Experimental and Analytical Evaluation of a Composite Honeycomb Deployable Energy Absorber

Karen E. Jackson, Sotiris Kellas, Lucas G. Horta, and Martin S. Annett
Langley Research Center, Hampton, Virginia

Michael A. Polanco and Justin D. Littell
ATK Space Systems, Inc., Hampton, Virginia

Edwin L. Fasanella
National Institute of Aerospace, Hampton, Virginia

NASA STI Program . . . in Profile

Since its founding, NASA has been dedicated to the advancement of aeronautics and space science. The NASA scientific and technical information (STI) program plays a key part in helping NASA maintain this important role.

The NASA STI program operates under the auspices of the Agency Chief Information Officer. It collects, organizes, provides for archiving, and disseminates NASA's STI. The NASA STI program provides access to the NASA Aeronautics and Space Database and its public interface, the NASA Technical Report Server, thus providing one of the largest collections of aeronautical and space science STI in the world. Results are published in both non-NASA channels and by NASA in the NASA STI Report Series, which includes the following report types:

- TECHNICAL PUBLICATION. Reports of completed research or a major significant phase of research that present the results of NASA programs and include extensive data or theoretical analysis. Includes compilations of significant scientific and technical data and information deemed to be of continuing reference value. NASA counterpart of peer-reviewed formal professional papers, but having less stringent limitations on manuscript length and extent of graphic presentations.

- TECHNICAL MEMORANDUM. Scientific and technical findings that are preliminary or of specialized interest, e.g., quick release reports, working papers, and bibliographies that contain minimal annotation. Does not contain extensive analysis.

- CONTRACTOR REPORT. Scientific and technical findings by NASA-sponsored contractors and grantees.

- CONFERENCE PUBLICATION. Collected papers from scientific and technical conferences, symposia, seminars, or other meetings sponsored or co-sponsored by NASA.

- SPECIAL PUBLICATION. Scientific, technical, or historical information from NASA programs, projects, and missions, often concerned with subjects having substantial public interest.

- TECHNICAL TRANSLATION. English-language translations of foreign scientific and technical material pertinent to NASA's mission.

Specialized services also include creating custom thesauri, building customized databases, and organizing and publishing research results.

For more information about the NASA STI program, see the following:

- Access the NASA STI program home page at *http://www.sti.nasa.gov*

- E-mail your question via the Internet to help@sti.nasa.gov

- Fax your question to the NASA STI Help Desk at 443-757-5803

- Phone the NASA STI Help Desk at 443-757-5802

- Write to:
  NASA STI Help Desk
  NASA Center for AeroSpace Information
  7115 Standard Drive
  Hanover, MD 21076-1320

Experimental and Analytical Evaluation of a Composite Honeycomb Deployable Energy Absorber

Karen E. Jackson, Sotiris Kellas, Lucas G. Horta, and Martin S. Annett
Langley Research Center, Hampton, Virginia

Michael A. Polanco and Justin D. Littell
ATK Space Systems, Inc., Hampton, Virginia

Edwin L. Fasanella
National Institute of Aerospace, Hampton, Virginia

Table of Contents

List of Figures

Page

List of Tables

**Experimental and Analytical Evaluation of a Composite Honeycomb
Deployable Energy Absorber**

Karen E. Jackson, Sotiris Kellas, Lucas G. Horta, and Martin S. Annett
NASA Langley Research Center
Hampton, VA

Michael A. Polanco and Justin D. Littell
ATK Space Systems, Inc.
Hampton, VA

Edwin L. Fasanella
National Institute for Aerospace (NIA)
Hampton, VA

1.0 ABSTRACT

In 2006, the NASA Subsonic Rotary Wing Aeronautics Program sponsored the experimental and analytical evaluation of an externally deployable composite honeycomb structure that is designed to attenuate impact energy during helicopter crashes. The concept, which is designated the Deployable Energy Absorber (DEA), utilizes an expandable Kevlar® honeycomb structure to dissipate kinetic energy through crushing. The DEA incorporates a unique flexible hinge design that allows the honeycomb to be packaged and stowed until needed for deployment. A variety of deployment options such as linear, radial, and/or hybrid methods can be used. Experimental evaluation of the DEA utilized a building block approach that included material characterization testing of its constituent, Kevlar®-129 fabric/epoxy, and flexural testing of single hexagonal cells. In addition, the energy attenuation capabilities of the DEA were demonstrated through dynamic crush tests of multi-cell components, and vertical drop tests of a composite fuselage section, retrofitted with DEA blocks, onto concrete, water, and soft soil. During each stage of DEA evaluation, finite element models of the test articles were developed and simulations were performed using the explicit, nonlinear transient dynamic finite element code, LS-DYNA. This report documents the results of the experimental evaluation that was conducted to assess the energy absorption capabilities of the DEA. In addition, details of the analytical simulations and test-analysis comparisons are presented.

2.0 INTRODUCTION

In 2005, the NASA Aeronautics Research Program was overhauled to focus on foundational physics and fundamental research in four flight regimes: hypersonics, supersonics, subsonic fixed wing, and subsonic rotary wing. Three guiding principles were established:
  • NASA is dedicated to the mastery and intellectual stewardship of the core competencies of Aeronautics for the Nation in all flight regimes,
  • The research will be focused in areas that are appropriate to NASA's unique capabilities, and
  • Research will be conducted to address the fundamental needs of the Next Generation Air Transportation System [1].
A four-step process was implemented in 2005-2006 to assess long-term research goals in each flight regime, solicit industry input regarding opportunities for cooperative partnerships, review

submitted proposals, and request additional proposals from universities for research in foundational physics. As part of this process, several in-house research proposals on rotorcraft crashworthiness were submitted, reviewed, and supported by the Subsonic Rotary Wing (SRW) Aeronautics Program [2].

Since its inception in 2006, the NASA SRW Aeronautics Program in Rotorcraft Crashworthiness has focused attention on two areas of research: the evaluation of an externally deployable energy absorbing (DEA) concept and improved prediction of rotorcraft crashworthiness. The DEA concept is a composite honeycomb structure that can be deployed, much like an external airbag system, to provide energy attenuation [3-5]. The concept was originally proposed and studied as a passive energy attenuation system for the Orion crew module, and was designed to significantly reduce impact loads transmitted to the crew during land or water impact following capsule re-entry. Eventually, the Orion Program Office focused on other energy attenuating concepts that had higher technical maturity [6]. However, during this early evaluation, the DEA concept demonstrated excellent energy absorption capabilities. As a result, the SRW Program selected the concept for further evaluation. Pre- and post-test photographs of a sample DEA component are shown in Figure 1.

The second SRW Rotorcraft Crashworthiness focus area relates to modeling and simulation. Several research topics have been identified to achieve improved prediction of rotorcraft crashworthiness, including: occupant modeling and injury prediction, multi-terrain impact simulation, model validation studies that focus on probabilistic analysis, and development of system-integrated simulation models [2]. An important aspect of the DEA evaluation was to develop finite element models that could accurately simulate the DEA crushing response under dynamic loading.
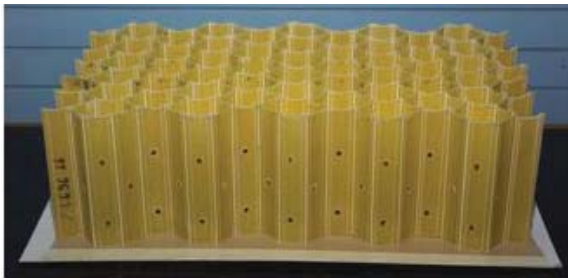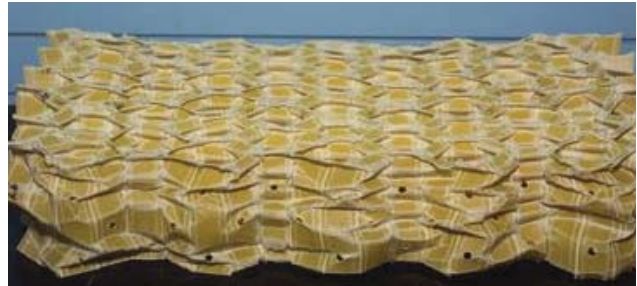
| (a) Pre-test photograph. | (b) Post-test photograph. |

Figure 1. Pre- and post-test photographs of a sample DEA component.

2.1 Motivation for DEA Development

Landing and crash energy management systems, which dissipate energy by stroking, can be grouped into two general categories. The first category consists of deployable devices such as hydraulic or pneumatic landing gears, vented airbags [7-10], non-vented airbags [11, 12], and hybrid airbag systems [13]. Non-deployable, or passive, energy absorbers belong to the second category which includes crushable honeycombs and cellular solids [14-17]. Generally, the type of crash energy management system chosen is governed by factors such as available volume, expected vehicle attitude, velocity at impact, mass allotment, and system reliability. Deployable

systems offer several advantages including efficient packaging and relatively large available stroke; however, due to their complexity, they are generally less reliable than passive systems.

External airbag systems have been utilized in many different aerospace applications. The most notable examples include plug-vented air bags on the F-111 crew-escape module [7], and non-vented air bags on the Mars Pathfinder [11]. Typically, non-vented airbag systems have an inherent degree of springiness due to residual gas pressure, which causes the vehicle to bounce several times before it comes to a complete rest. To offer adequate protection, the airbag is required to cover the entire vehicle, which generally leads to a heavier and more complex system. Because of sequential energy absorption (bouncing), non-vented airbag systems are not suitable for manned applications. Vented bags are generally more efficient energy dissipators, when compared to non-vented systems. These can be grouped into two general categories: automobile type airbags [8], which rely on time sensitive deployment in order to operate correctly, and bags with blow-out plugs [7, 13] which vent when a predetermined pressure is sensed. Unfortunately, when used on aircraft to improve crashworthiness, serious reliability issues can offset potential advantages in energy absorption.

In the case of automobile-type airbags, which have been considered for external use on rotorcraft to mitigate crash loads [8-10], precise determination of impending impact over varying terrain is required, which is a very challenging problem. Assuming that external airbags can be inflated fast enough and that all other sensors and systems function correctly, serious reliability issues can still arise for plug-vented systems when venting is partially or totally impaired due to the vehicle's unforeseen impact attitude. When gas is trapped, due to choked vents, these systems can cause vehicle tumbling, as occurred during impact testing of the airbag system mounted to the F-111 crew-escape module, see Figure 2. Finally, all gas-filled airbag systems suffer from low shear stability, loading-rate sensitivity, impact/venting synchronization (especially when multiple airbags are used), and sensitivity to extreme landing surface features such as rocks and steep slopes. Consequently, extensive testing and/or analyses are often required for system development and qualification, as was demonstrated by the F-111 program [18, 19].
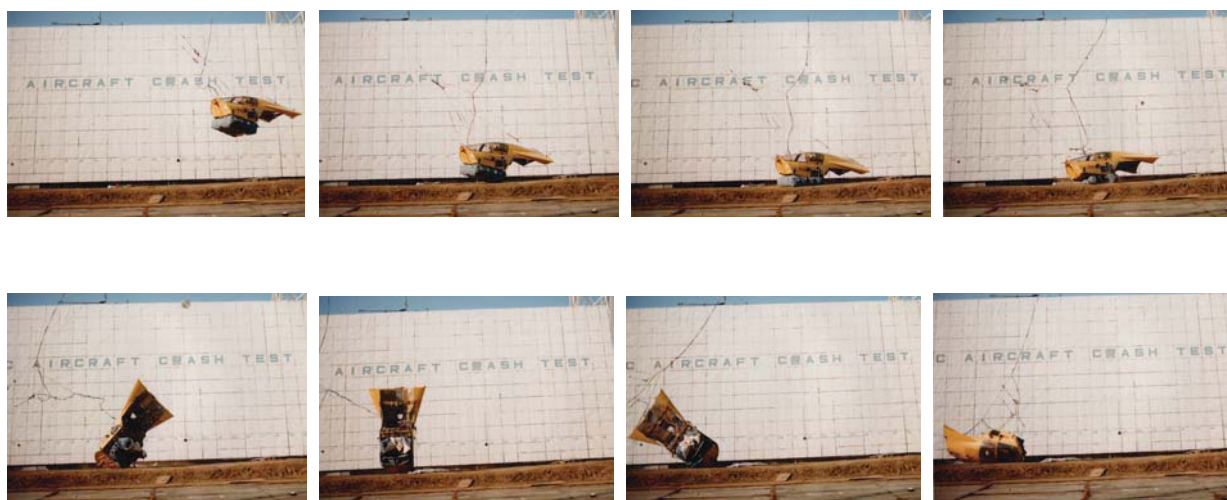
Figure 2. Series of photographs of an F-111 crew module impact test.

In order to avoid bottoming out, which is an inevitable negative aspect of vented airbags; a hybrid airbag approach was proposed for the Orion crew module [13]. The system consists of an internal non-vented bag (anti-bottoming) within a larger external vented bag (energy absorber). While this approach addresses the bottoming out issue, it does lead to a heavier and more complex system. Moreover, the non-vented bag is essentially a spring, which under certain attitude conditions could contribute to vehicle tumbling. To address the airbag shear issue, Mehaffie [17] studied a foam-filled airbag system for the recovery of small pilotless aircraft. While this concept appears to provide a viable solution to shear, time sensitive foam hardening and excess weight make it inappropriate for crashworthiness applications.

2.2 Description of the DEA Concept

The composite honeycomb Deployable Energy Absorber (DEA) possesses many of the desirable features of a deployable airbag system while overcoming most of their limitations. As with the Bixby [15] and Schafer [16] concepts, the new energy absorber utilizes an expandable honeycomb structure to absorb impact energy by crushing. However, unlike other cellular energy absorbers in use today, the new concept utilizes a unique and patented flexible hinge at each junction of its cell walls [3]. This feature enables almost any size and strength energy absorber to be fabricated and readily deployed either radially (omnidirectional energy absorption) or linearly (unidirectional energy absorption). Like conventional honeycomb, once expanded the new energy absorber is transformed into an efficient orthotropic cellular structure, with greater stiffness and strength along the cell axis as compared to the transverse directions.

An example of an isolated cell-wall junction is shown in the schematic of Figure 3, and a photograph of a stitched junction is depicted in Figure 4. In this example, a zigzag stitch pattern was used to eliminate delamination between the plies. Typically, the hinge is made of Kevlar®-129 fabric/epoxy with the fibers oriented at ±45° with respect to the hinge, or longitudinal, axis. The hinge consists of a fabric made of relatively strong, stiff, and tough fibers such as Spectra®, Vectran®, or Technora®. Other flexible materials can also be used for the construction of the hinges; however, advanced fiber reinforced fabrics are thought to offer some unique opportunities for structural tailoring. Examples of properties that can be optimized, individually or collectively, include minimal deployment force, shear rigidity, shear strength, hinge tearing resistance, and specific energy absorption. For the purposes of this paper, all DEA structures were fabricated of Kevlar®-129 fabric with Reinfusion 8601 epoxy resin. In addition, all DEA test articles were constructed of either single or multiple hexagonal cells.

The flexible hinge enables various methods of expanding the cellular structure with the most basic ones shown in Figures 5-7. The linear expansion mode, which is depicted in the schematic of Figure 5, represents the simplest mode. When expanded in this fashion the energy absorber produces higher specific energy absorption due to a more efficient volumetric expansion (lower effective expanded density). However, radial deployment, illustrated in Figure 6, produces an energy absorber with better omnidirectional capability. Because most practical applications involve curved rather than flat surfaces, the two basic deployment methods can be combined into a hybrid approach, as shown in Figure 7. To minimize the expanded density of the energy absorber, the cells are tapered, as shown in Figure 7(c). An artist's conception of how the energy absorber could be used on a rotorcraft to improve its crashworthiness is shown in Figure 8. For

this application, the energy absorber would be stowed under a frangible (or removable) aerodynamic cowling until a command is given to deploy the energy absorbers. Additional details regarding mathematical development of the DEA, the fabrication process, and deployment methods can be found in Reference 4.
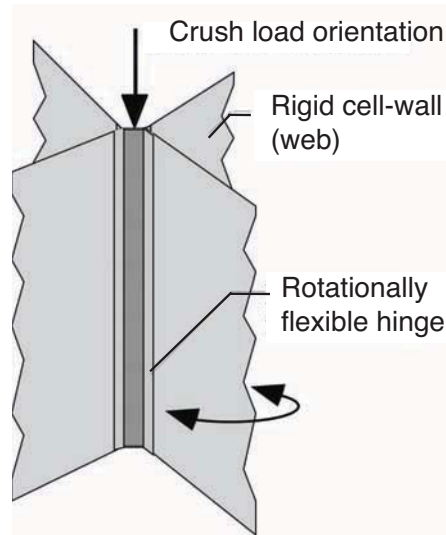
Figure 3. Schematic of the junction (hinge) of a square cell deployable structure.
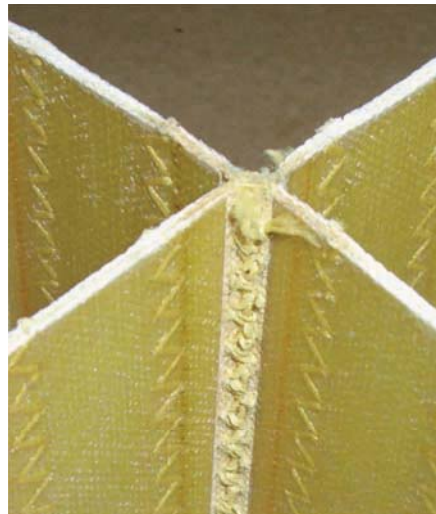
Figure 4. Photograph of square cell junction fabricated of Kevlar®-129 and E-glass fabrics.

2.3 Objectives

The objectives of this paper are to document the results of testing and analytical simulations that were performed during evaluation of the DEA concept. Experimental research included material property characterization testing of the DEA constituent, Kevlar®-129 fabric/epoxy; flexural testing of single hexagonal cells; dynamic crush testing of multi-cell DEA components; and vertical drop tests of a composite fuselage section, retrofitted with DEA blocks, onto three different terrains. An analytical effort was conducted to complement and augment the experimental program. Finite element models were developed to assist in DEA evaluation using

the explicit, nonlinear transient dynamic code, LS-DYNA [20, 21]. Details of the analytical simulations and test-analysis comparisons are also presented.
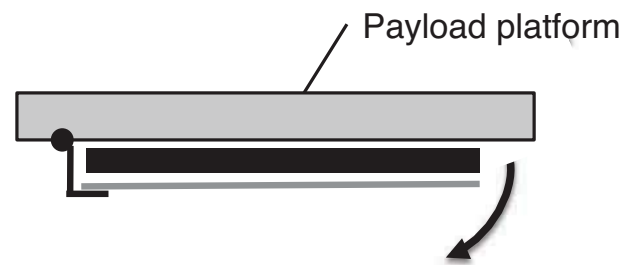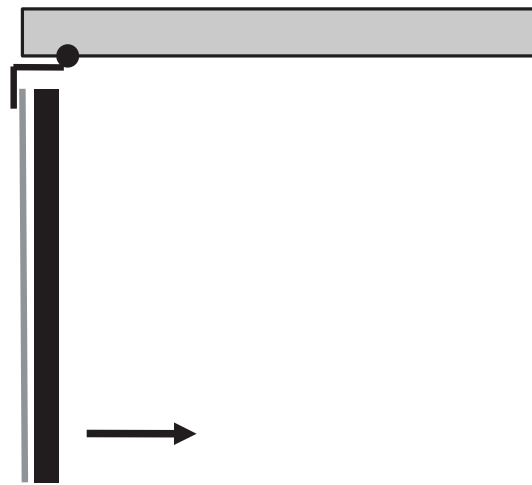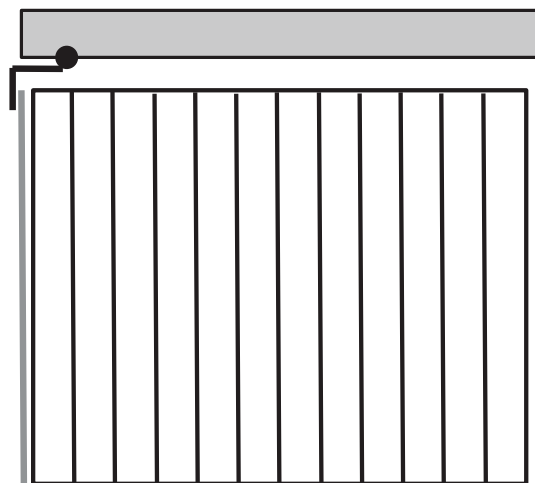
Figure 5. Basic steps required for linear deployment of a packed energy absorber. Deployment mechanisms could include springs or actuators of various kinds.

Payload platform
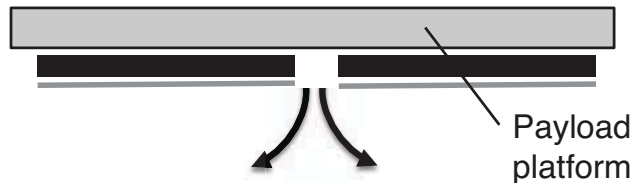
(a) Packed energy absorber
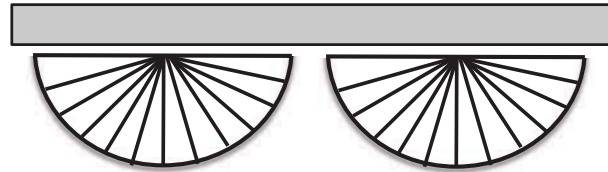
(b) Pair of DEA expanded radially

Figure 6. Radial deployment of two energy absorbers. Note that deployment greater than 180° is possible if more vehicle coverage is required.
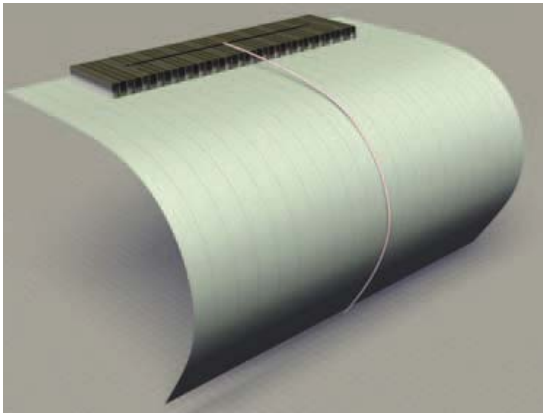
(a) Packed DEA.
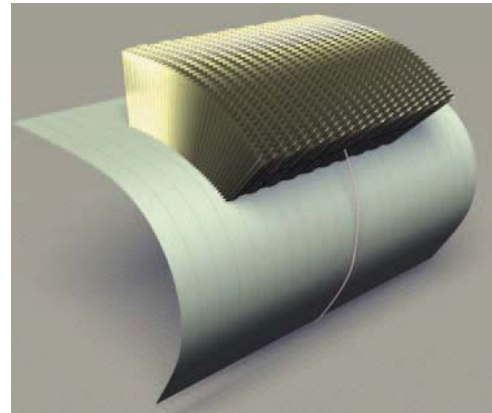
(b) Partially deployed DEA.
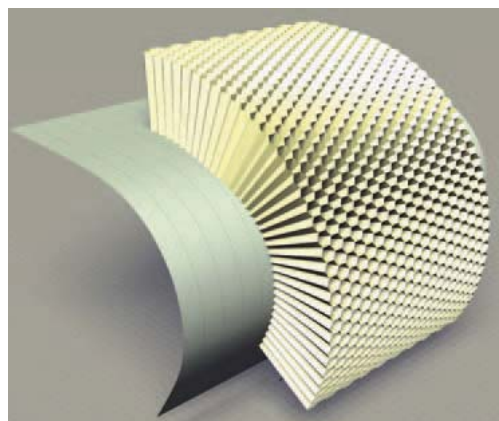
(c) Fully deployed DEA.

Figure 7. Hybrid deployment example with the energy absorber deployed over a curved surface.

Figure 8. Artist's rendition of a rotorcraft with a set of energy absorbers deployed. The front energy absorbers are shaped to allow for egress.

3.0 EXPERIMENTAL PROGRAM

This section of the paper summarizes the results of the experimental program that was conducted during evaluation of the DEA concept. It includes materials testing of Kevlar[®]-129 fabric/epoxy, flexural (3-point bend) testing of single hexagonal cells, dynamic crush tests of multi-cell DEA components, and vertical drop tests of a retrofitted fuselage section onto three different terrains.

3.1 Materials Testing of Kevlar[®]-129 Fabric/Epoxy

As mentioned previously, all DEA structures that were tested as part of the concept evaluation process were fabricated of Kevlar[®]-129 plain-weave woven fabric with Reinfusion 8601 epoxy resin, with a nominal ply thickness of 0.01-in. Kevlar[®] is a tough, high-modulus composite material that is commonly used in bullet/fragment resistant apparel, fiber-optic cables, and automotive belts and tires. In addition, Kevlar[®] has demonstrated excellent energy absorption capabilities under compressive loading [22]. During construction of the DEA, the Kevlar[®]-129 fabric/epoxy material was oriented at ±45° with respect to the longitudinal axis of the cells. Limited material testing was performed to provide data for concept design, and for input into the LS-DYNA finite element models. Additional information regarding material testing may be found in Reference 4.

3.1.1 Tensile Tests of 0°/90° Coupons

Tensile tests were performed on single ply coupons of Kevlar[®]-129 fabric/epoxy with fibers oriented at 0°/90° with respect to the loading direction. Coupon dimensions were: length of 6-in. (4.15-in. gage length), a width of 1.0-in. and a nominal thickness of 0.01-in. Five coupons were tested quasi-statically at a displacement rate of 1.0-inch per minute (ipm) using a standard load test machine. The individual and average stress-strain results are shown in Figures 9(a) and (b), respectively. Based on the average test results, the material exhibits a nearly linear-elastic response to ultimate failure, which occurs at a strain of 0.05-in/in and a stress of 76-ksi. A tensile modulus of 1.5e06-psi was estimated based on a linear curve fit of the material response at low strain values. Note that the noise seen in the raw test data is an artifact of the data acquisition system.

8

(a) 0°/90° response data.
(b) 0°/90° average response.
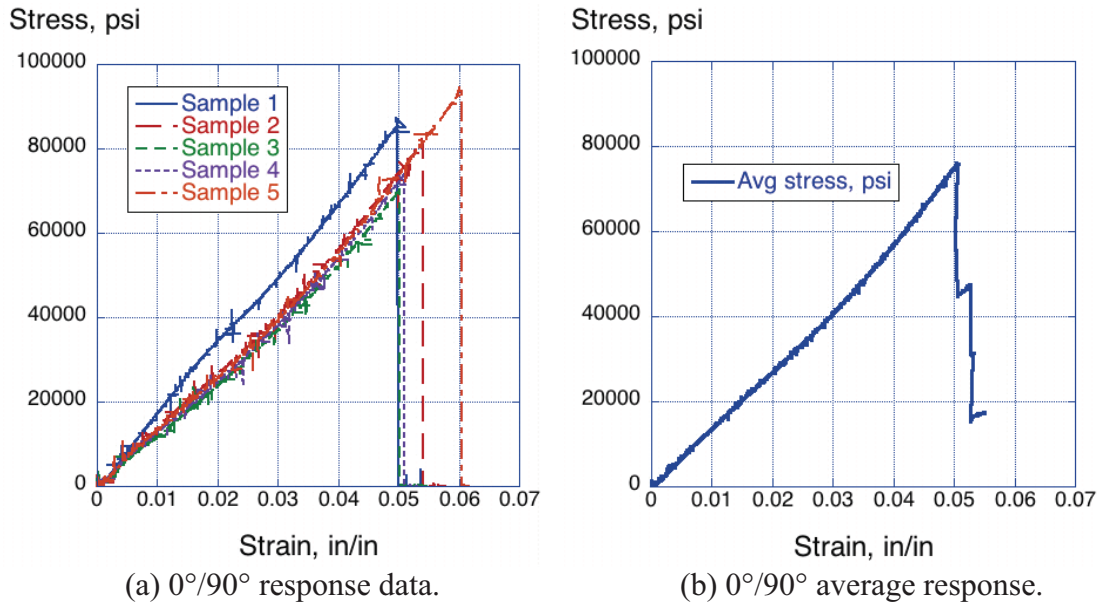
Figure 9. Tensile stress-strain response of 0°/90° Kevlar®-129 fabric/epoxy coupons.

3.1.2 Tensile Tests of ±45° Coupons

Two sets of tensile tests were performed using the same size of coupons as described previously; however, for these coupons the fibers were oriented at ±45° with respect to the loading direction. For each set, five coupons were tested at two different displacement rates: 1.0-ipm and 20-ipm. The individual stress-strain responses for the two different displacement rates are shown in Figure 10 and the average stress-strain results are shown in Figure 11. As noted previously, the noise or chatter seen in the raw test data is an artifact of the data acquisition system.

(a) ±45° response data at 1-ipm.
(b) ±45° response data at 20-ipm.
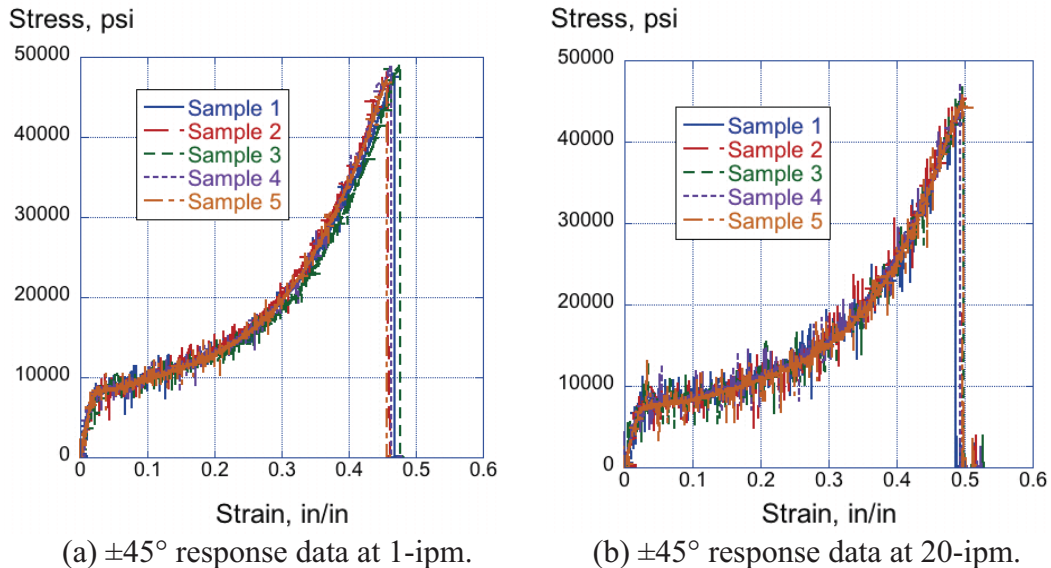
Figure 10. Tensile stress-strain responses of ±45° Kevlar®-129 fabric/epoxy coupons tested at two different displacement rates.

9
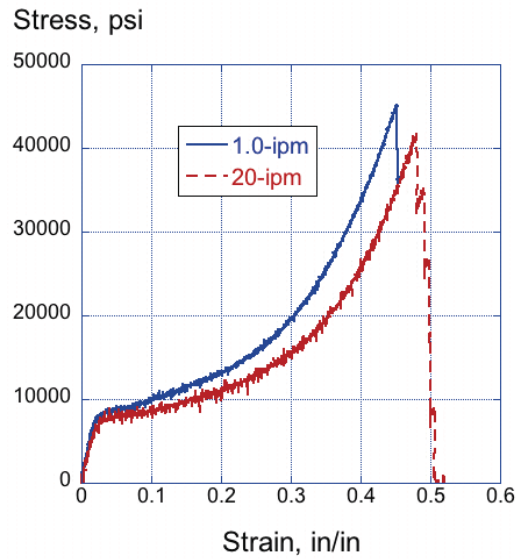
Figure 11. Average stress-strain responses of ±45° Kevlar® fabric/epoxy tensile coupons tested at two different displacement rates.

It is important to note that the data obtained from tensile tests of ±45° coupons can be used to derive material properties for shear including shear stiffness, shear strength, and ultimate shear strain-to-failure, as documented in Reference 23. Based on the average test results, the material exhibits a linear response to approximately 8,000-psi, and then yields, followed by a nonlinear strain hardening response. This portion of the stress-strain response is attributed to progressive matrix failure, which allows the fibers to reorient in the direction of loading (fiber scissoring), which, in turn, produces the stiffening effect seen in the response. It is also interesting to note that material testing performed at higher strain rates either produces the same response for materials that are not rate sensitive or provides higher stress-strain responses for strain-rate dependent materials. For the results shown in Figure 11, the Kevlar®-129 fabric/epoxy material indicates a higher stress-strain response for the lower strain rate, which is opposite to the typical response. Without testing at a third strain rate, it is impossible to know if this behavior is a trend for this material.

3.2 Three-Point Bend Testing of Single Hexagonal Cells

The effect of cell geometry on the shear stability of the DEA was studied through a series of simple, quasi-static tests. Three-point-bend tests were conducted on single-hexagonal-cell samples. Specimens were fabricated using the same materials and methods as the actual deployable structures, including hinge lines. A typical test sample, under load, is shown in the photograph of Figure 12(a). Each cell sample contained three 0.25-in.-thick hexagonal Bakelite stanchions located at each of the loading points. The role of the stanchions, which were bonded to the cell walls, was to preserve the hexagonal shape of the cell while distributing the load uniformly over the entire perimeter of the cell. To eliminate possible trapped air effects during loading, each stanchion was perforated. The test fixture, shown in Figure 12(a), was designed to accommodate samples of varying length, L, and load-displacement data were recorded until a peak load was reached. The three-point-bend study involved testing of four sets of scaled

specimens, five specimens per set, in which the ratio, L/W, was kept constant at 1.75 and the flat facet width, W, was varied (W=0.75-in., 1.0-in., 1.25-in. and 1.5-in.). For the scaled specimens, displacement rates were prescribed by the width of the specimen. For example, the specimen with a width of W=1.25-in. was tested at a displacement rate of 1.25-ipm. The cross-sectional geometry of the W=1.0-in. specimen is shown in Figure 12(b). All specimens were fabricated of single ply Kevlar®-129 fabric/epoxy with a nominal thickness of 0.01-in. The fabric was oriented at ±45° with respect to the longitudinal axis of the cell. One specimen of each size is depicted in the photograph of Figure 13. Since specimens were scaled, only one was chosen for presentation, in this case the specimens with a width of W=1.0-in. Individual sample and average load versus displacement responses for the W=1.0-in. single cells are shown in Figures 14(a) and (b), respectively.

Characteristic instability modes in this type of sample were shear buckling in the lower oblique cell walls and compressive buckling on the top horizontal cell wall, as indicated in Figure 12(a). Due to considerable scatter in the results, as shown in Figure 14(a), at least five samples were tested for each geometry case. In Reference 4, the maximum stress for each of the four single hexagonal cell specimens was calculated by dividing the peak load by the cross sectional area of the hexagonal cell, and the maximum stress was plotted versus t/W. Based on these results and assuming that the three-point bend test is truly representative, the shear stability increases linearly with t/W.

| (a) Photograph of 3-point bend test. | (b) Geometry of W=1.0-in. specimen. |
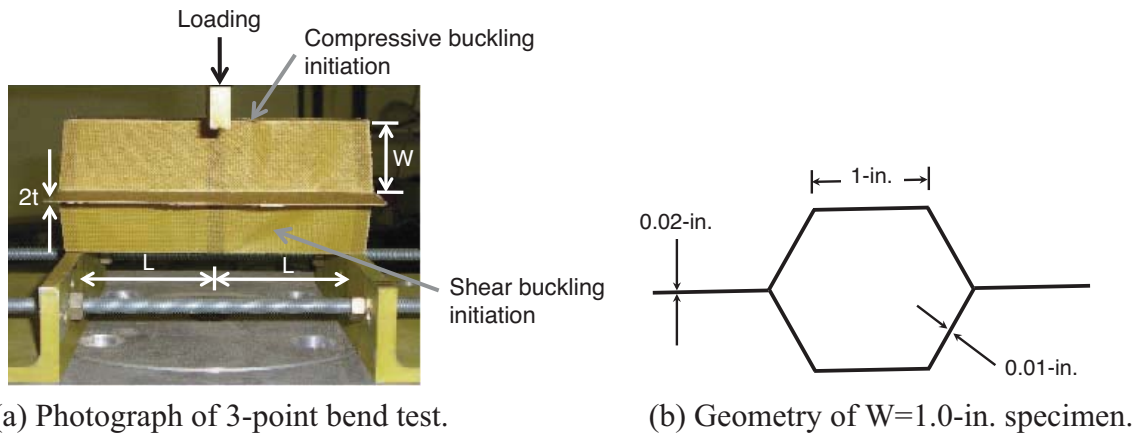
Figure 12. Three-point-bend set-up for single cell tests.
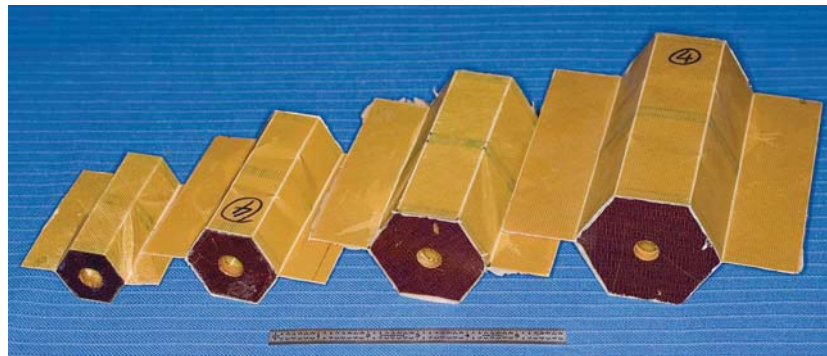
Figure 13. Photographs of four scaled single hexagonal cell specimens.

(a) Responses of five samples.   (b) Average of five responses.
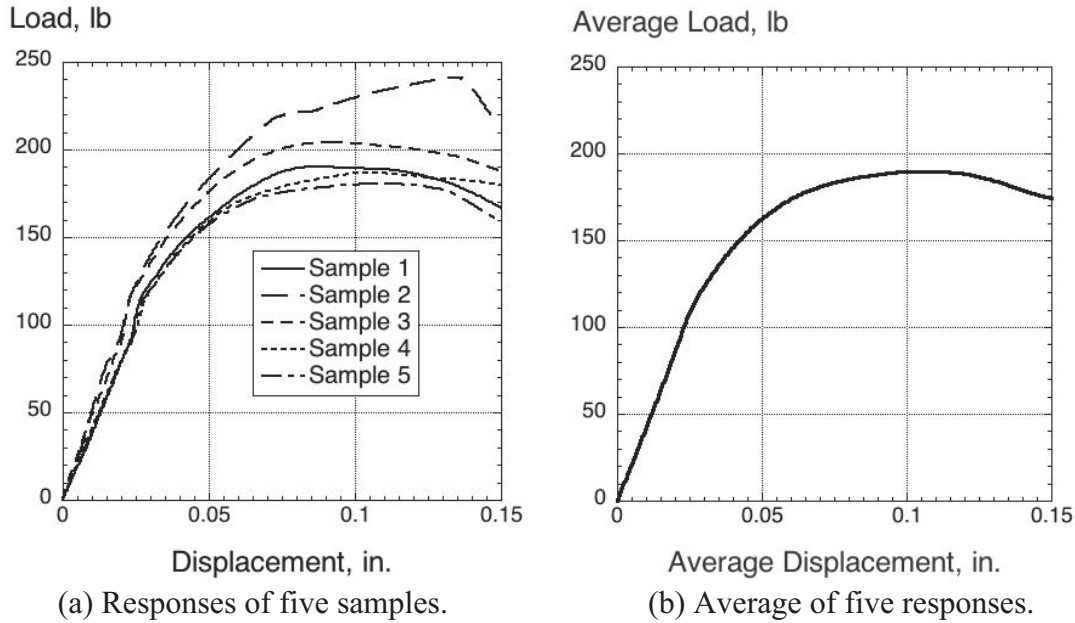
Figure 14. Load versus displacement response from 3-point-bend tests on samples with
t=0.01-in. and W= 1.0-in.

3.3 Multi-Cell DEA Component Crush Testing

Three multi-cell components were fabricated to evaluate the energy absorption capabilities of the
DEA under both normal and off-axis loading conditions. Each of the components was fabricated
of hexagonal cells having a 1-in. flat facet width. Two of the DEA components, consisting of
59- and 104-cells, were manufactured such that the longitudinal axes of the cells were oriented in
the same direction as loading (normal). A third DEA component, consisting of 68-cells, was
fabricated such that the longitudinal axis of the cells was canted by 27° with respect to the
direction of loading (off-axis). The top surface of each DEA component was curved slightly to
reduce the high peak loads that can occur during initial impact. Also, transverse holes were
drilled into the DEA components to allow entrapped air to escape.

Each component was impacted in a fully deployed state by a rigid impact mass, or block, that
translated on vertical support rods through low-friction bearings.   The drop mass was
instrumented with an accelerometer to record the vertical acceleration response.   Details
regarding the dimensions of each DEA component and the impact test conditions are listed in
Table 1. Additional information on the DEA fabrication method and multi-cell component crush
testing may be found in Reference 4.

Table 1. Details of DEA Component Crush Testing

Number of cells	Cell orientation*	Length, in.	Width, in.	Height, in.	Area, in^2	Impact block weight, lb.	Velocity at impact, in/s
59	0°	16	12.4	6.0	198	412.5	195.6
104	0°	21	15.8	10.0	331	477.2	266.4
68	27°	16	14.0	6.7	224	477.2	183.6

*with respect to the vertical, or loading, direction

12

3.3.1 59-Cell DEA Crush Test

The measured acceleration time history obtained from the 59-cell DEA component crush test is plotted in Figure 15(a), and the integrated velocity and displacement time histories are plotted in Figures 15(b) and (c), respectively. An average acceleration of 7.1-g was determined for the time interval of 0- to 0.03-s, prior to the large increase in acceleration that initiates at 0.034-s. The increase in acceleration is attributed to compaction or "bottoming out" of the DEA. Also, the maximum vertical displacement of the DEA was 5.6-inches. Given that the original height of the DEA was 6-in., a total crush stroke of 93% was obtained. Note that the 59-cell DEA specimen exhibited stable crushing for 5-in. of vertical displacement, or 83% maximum stroke prior to initiation of compaction. A close-up photograph of the post-test specimen is shown in Figure 16, which highlights the primary deformation and failure modes of the DEA. The DEA dissipates kinetic energy through local buckling of the cell walls and plastic hinge formation. In addition, some minor delamination and tearing at the cell wall interfaces are observed.

(a) Acceleration time history. (b) Velocity time history. (c) Displacement time history.
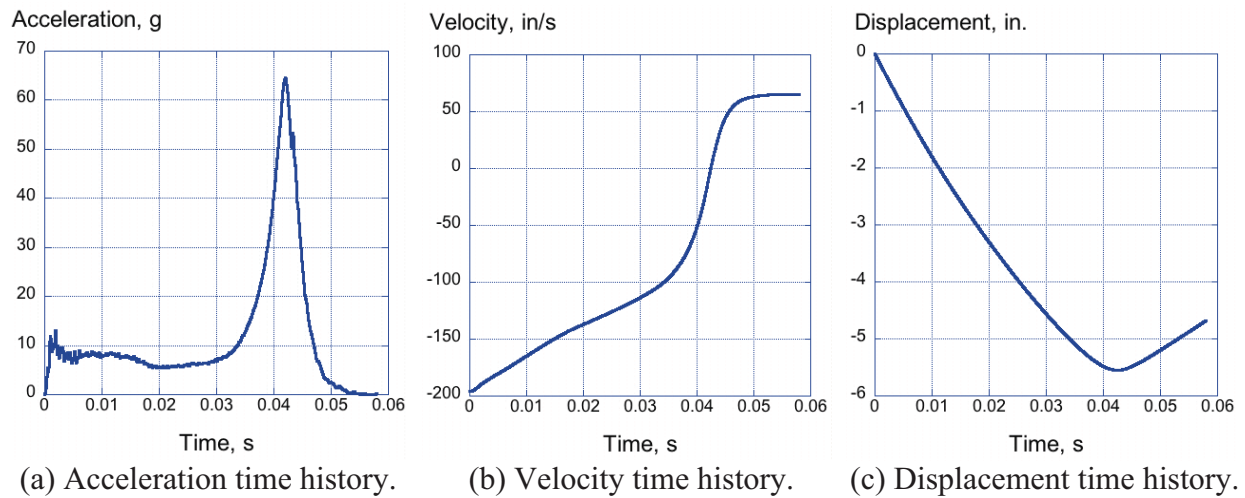
Figure 15. Test data from the dynamic compression test of the 59-cell DEA.

Figure 16. Close-up photograph illustrating the energy absorption modes exhibited by the DEA.

13

3.3.2 104-Cell DEA Crush Test

A second DEA component was fabricated that consisted of 104-hexagonal cells with specimen dimensions and impact loading conditions listed in Table 1. The measured acceleration time history is plotted in Figure 17(a), and the integrated velocity and displacement time histories are plotted in Figures 17(b) and (c), respectively. An average acceleration of 14.3-g was determined for the time interval of 0- to 0.03-s. It is interesting to note the differences in acceleration responses between the 59- and the 104-cell DEA components, shown in Figures 15(a) and 17(a), respectively. The acceleration response of the 59-cell DEA indicates that the component was compacted during crushing, which produces a large increase in acceleration near the end of the pulse. However, the acceleration response of the 104-cell DEA indicates that the specimen did not achieve compaction, even though a higher impact mass and velocity were used during the impact test. Obviously, the incident kinetic energy was insufficient to produce compaction due to the greater cross-sectional area and height of the 104-cell DEA. Based on a maximum displacement of 6.6-in., a crush stroke of 65.6% was obtained for the 104-cell DEA. A post-test photograph of the 104-cell DEA component is shown in Figure 18. Similar deformation modes of local cell wall buckling, plastic hinge formation, minor delamination and tearing at the cell wall junctions are observed; however, considerably less damage is seen overall when compared with the 59-cell DEA component.

(a) Acceleration response.   (b) Velocity response.   (c) Displacement response.
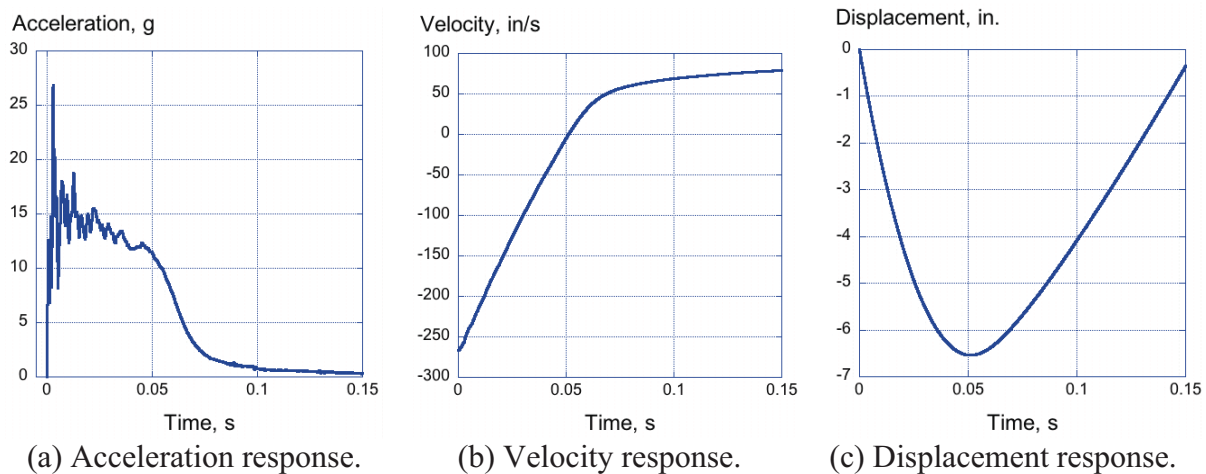
Figure 17. Results of the dynamic crush test of the 104-cell DEA component.

Figure 18. Post-test photograph of the 104-cell DEA component.

3.3.3 68-Cell DEA Crush Test

A final DEA component was fabricated of 68 hexagonal cells in which the longitudinal axis of the cells was canted by 27° with respect to the vertical direction. Component dimensions and impact loading conditions are listed in Table 1. The 68-cell DEA component was fabricated and tested specifically to determine how the DEA would respond under combined normal and shear loading. Unlike the two previous component tests, the bottom surface of the DEA was attached to a flat aluminum plate using potting material prior to the impact test.

Acceleration, velocity, and displacement time histories are shown in Figure 19 for the 68-cell canted DEA component. The acceleration curve, shown in Figure 19(a), achieves an initial acceleration of 10-g at 0.004-s, which subsequently drops to 5-g and then begins to increase to a second peak of 27.7-g at 0.0475-s. The initial reduction in acceleration following the 10-g peak is attributed to global buckling and collapse of a row of perimeter cells. Following this collapse, the interior cells begin to react the load and the acceleration increases as compaction begins to occur. The second peak is attributed to compaction of the DEA component. Based on the maximum displacement of 5.6-in., a crush stoke of 83.6% was determined. An average acceleration of 6.5-g was calculated for the time interval of 0- and 0.03-s. This value is only 8% lower than the value obtained for the 59-cell DEA component, which had all of its cells oriented in the same direction as the loading axis.

(a) Acceleration response.   (b) Velocity response.   (c) Displacement response.
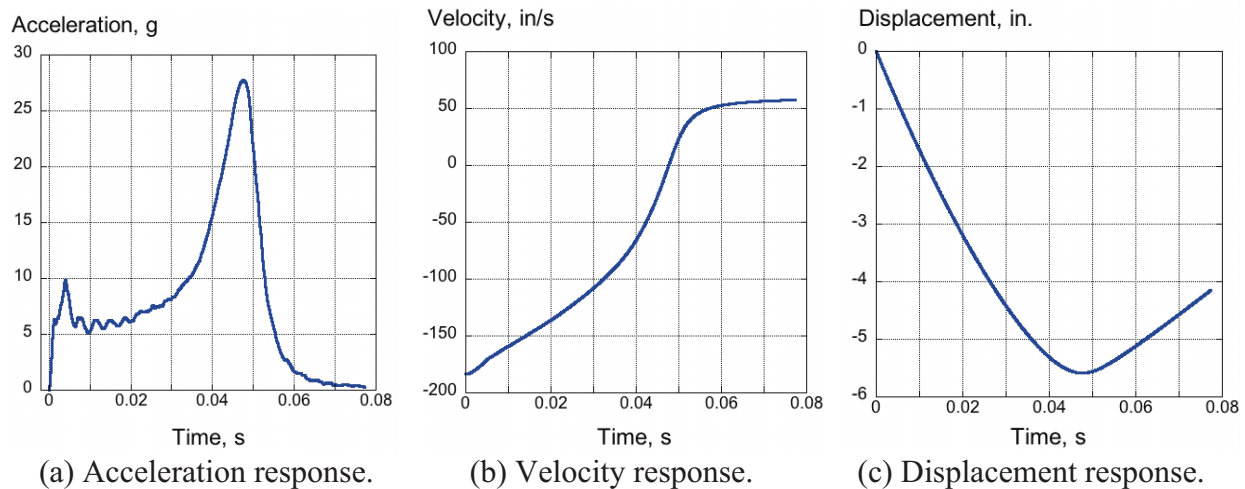
Figure 19. Results of the dynamic crush test of the 68-cell DEA component.

The crush response of the 68-cell DEA was recorded using high-speed video and several photographs taken from the video are shown in Figure 20. These photos indicate that the crushing response of the DEA is fairly uniform, despite the higher shear loading present in the off-axis test. The off-axis orientation contributed to global buckling of a row of perimeter cells, which is evident on the left side of Figure 20(b).

15

(a) EA prior to impact.
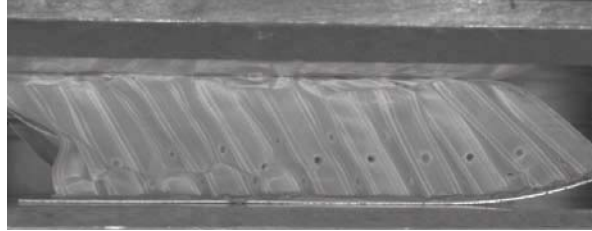
(b) EA after approximately 35% of crush.
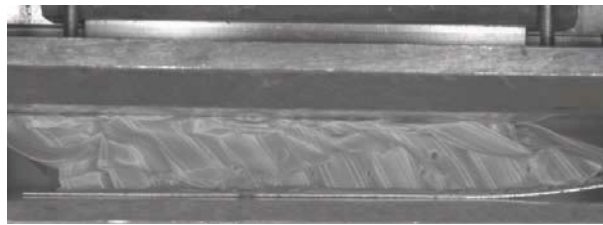
(c) EA after approximately 60% of crush.

Figure 20. High-speed video frames from 27° off axis test.

3.3.4 Comparative Analysis of the DEA Component Results

Test results for three DEA components have been presented, each of which was fabricated of Kevlar®-129 fabric/epoxy oriented at ±45° with respect to the longitudinal cell axis. Also, each DEA component had a cell wall edge length of 1.0-in. and a nominal cell wall thickness of 0.01-in. This particular configuration of the DEA was designed to yield an average crush stress of approximately 20-psi [4]. The stress-strain responses of the 59-, 104-, and 68-cell DEA components were determined, based on the measured acceleration data. The stress was calculated by adding 1 to the acceleration data in g's, to account for the acceleration of gravity, and then multiplying the sum by the weight of the impact block, and then dividing by the cross-sectional area of the DEA. The strain was determined by double integration of the acceleration response to obtain displacement, which was divided by the initial vertical height of the DEA component. Stress-strain responses for each DEA component are plotted in Figure 21. The average stress for each DEA was determined by calculating the area under the stress curve for the strain interval of 0- to 0.6-in/in. Then, the total area is divided by the strain interval. The average stress values are 15.6-psi for the 68-cell DEA, 17.6-psi for the 59-cell DEA, and 22.0-psi for the 104-cell DEA. If the crush stresses of the two normal DEA components (59- and 104-cell) are averaged, a value of 19.8-psi is obtained, which is just slightly below the design goal. Please note that values of average crush stress are reported in later sections of the report based on average acceleration over a time interval of 0.0-0.03-s. These numbers may differ slightly from the ones shown in Figure 21, based on the different intervals used in the calculation.

16

One potential explanation for the reduction in average stress for the 59-cell DEA is the fact that this component has a larger percentage of circumferential cells, which tend to buckle globally instead of crushing uniformly, thus lowering the effective crush stress. Unlike the interior cells, the circumferential cells are only partially supported by neighboring cells. As mentioned previously, the 68-cell DEA exhibited crushing, as well as bucking of some cells on the perimeter of the component. The large reduction in acceleration following the initial peak, shown in Figure 19(a), is attributed to global buckling of these cells. However, the stiffness of the component is restored as the interior cells crush uniformly and eventually compact. The performance of the DEA concept under off-axis loading is considered excellent, with a relatively small reduction in average acceleration when compared with the 59-cell DEA. Typically, energy-absorbing components, such as tubes and truncated cones, show significant reductions in crush performance under off-axis loading [24, 25].
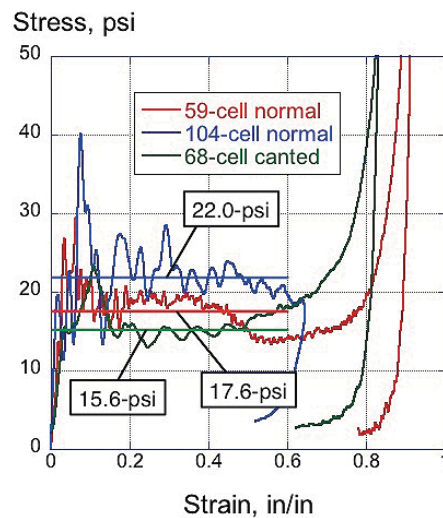
Figure 21. Crush stress versus strain of three DEA components.

3.4 Multi-Terrain Impact Testing of a Composite Fuselage Section Retrofitted with DEA

A major challenge that designers face when considering crashworthiness of helicopters arises from the unknown morphology of the crash site, including surfaces such as concrete, water, and soft soil. In fact, helicopter accident data indicate that more than 80% of crashes occur onto multi-terrain surfaces such as water, soft soil, plowed or grassy fields, and shallow swamps, as opposed to smooth prepared surfaces [26]. In addition, research studies have shown that helicopters, designed for crash resistance onto hard surfaces, do not perform well during multi-terrain impacts [27-32]. For hard and non-yielding impact surfaces, the vehicle's kinetic energy has to be managed by the airframe and internal and/or external energy absorbing devices to ensure load attenuation and adequate post-crash cabin volume. Often, legacy airframes have little or no internal structure designed for crash energy management. Consequently, external energy absorbers with large stroke capability are often necessary.

For hard surface impact, the cross-sectional shape of the external energy absorber is not important as long as stroking is not hindered. Conversely, for water impact the energy absorber stroke is less relevant since peak dynamic loads are brief and typically last only as long as it

17

takes for the vehicle to break through the water surface. However, the shape of the penetrating surface is much more critical and typically determines the magnitude of the peak load. Devices such as landing gear and/or skids, which can be very effective in absorbing energy on relatively hard surfaces, are rendered useless during water impacts. Moreover, protruding devices used for energy absorption can become a liability during water or soft soil impacts that involve large forward velocities, causing the aircraft to be more sensitive to tumbling. In addition to conventional retractable landing gear, other externally deployable devices, which have been proposed for helicopter active crash protection include vented airbags [9, 10], porous airbags, [8] and the composite honeycomb DEA concept [4, 5].

Since landing and/or skid gears are ineffective during water impact, Michielsen *et al* [33] have proposed the tensor skin panel concept where crash energy is dissipated by the deflection of an energy absorbing composite sandwich belly panel. In essence, this approach is similar to the one previously proposed in Reference 34 where most of the crash energy is dissipated by crushable structure placed between a rigid floor and a flexible aerodynamic cowling. Therefore, for both concepts, stroking is limited by the available subfloor space. The multi-terrain capability of the concept proposed in Reference 34 was investigated by Sareen *et al* [27] for hard and soft surface impacts, and by Fasanella *et al* [28] for water impact. While concepts with integrated subfloor energy absorption capability can help mitigate impact loads, their performance is limited by the crush stroke capacity – an area in which externally deployable energy absorbers have a clear advantage.

A necessary requirement for the successful utilization of the deployable honeycomb in multi-terrain impact applications is the capability to transfer load from the impact surface into the cell walls to initiate progressive crushing. Essentially, for soft surface impacts, the honeycomb must be prevented from acting as a "cookie cutter". Therefore, the honeycomb's surface, which contacts the impact surface, must be covered. While the primary role of a cover is to introduce the load into the honeycomb cells, the cover also has to be geometrically compatible with the energy absorber, both in its stowed and deployed stages. Several energy absorber cover concepts were considered and the ones that met all design requirements for vertical impacts were fabricated and tested prior to full-scale impact testing, as described in Reference 5. Friction, which is an important parameter in forward impact velocities, was not considered in this preliminary cover design study. A typical geometry of a covered energy absorber is shown schematically in Figure 22.
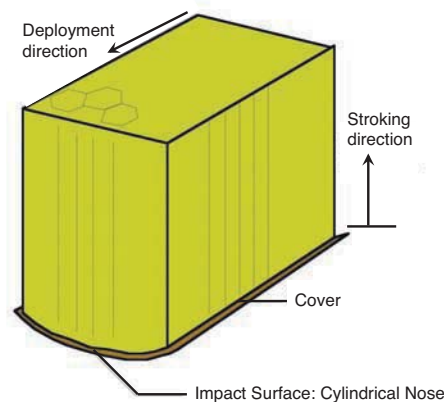
Figure 22. Schematic of a covered deployed energy absorber with a cylindrical impact nose.

18

In 2006 and 2007, vertical drop tests were conducted using a 5-ft-diameter, 5-ft-long composite fuselage section to evaluate the energy absorption capabilities of the DEA during multi-terrain impact. In particular, tests were performed onto a rigid concrete surface, water, and soft soil (sand). The composite fuselage section was developed during a prior research program [35] at NASA Langley Research Center and was used as a test bed to evaluate the responses of seats and dummies [36], to study quantitative correlation methods including experimental uncertainty [37], and to examine the influence of multi-terrain [38]. The fuselage section is fabricated using composite sandwich construction. The upper fuselage cabin is fabricated of 3-lb/ft^3 polyurethane closed-cell foam with E-glass/epoxy fabric face sheets, while the floor is fabricated of 8-lb/ft^3 polyurethane closed-cell foam with hybrid E-glass/epoxy and graphite/epoxy fabric face sheets. The layers of graphite/epoxy fabric and the higher density foam provided increased stiffness and improved structural rigidity of the floor, which is designed to serve as primary, load-bearing structure. As such, the floor must react the loads generated by crushing of subfloor energy absorbers or external energy attenuating systems.

For the multi-terrain impact tests that were conducted as part of the DEA evaluation program, the fuselage section was outfitted with ten 100-lb lead blocks that were mounted, five per side, to the floor of the fuselage section using standard seat rail fasteners. Accelerometers (250-g maximum range) were mounted on the lead blocks to record the dynamic structural response of the floor. Four DEA blocks were fabricated and attached to the bottom surface of the fuselage section. The DEA blocks were made of a single woven-ply of Kevlar®-129 fabric/epoxy, oriented at ±45° with respect to the longitudinal direction, had a nominal cell edge length of 1.0-in., and weighed 5.6-lb each. The deployed size of the honeycomb blocks was 20-in. tall, 16.5-in. wide and 20.5-in. deep and incorporated a curved surface (18-in. radius) on the bottom. The 18-in. cylindrical curvature was necessary to attenuate the initial peak loads for rigid surface impacts. The DEA blocks were sized based on the rigid-surface impact test with the assumption that the crash energy of a 40-ft/s impact would be managed through crushing of the DEAs while restricting the dynamic loads to less than 20-g. Therefore, 20-g was the target level for the sustained crushing load, also referred to as the energy absorber design crush load. The results of the multi-terrain impact tests will be described in the following subsections of the paper.

3.4.1 Rigid Surface Impact Test

The rigid surface impact test was performed using the 70-ft. Vertical Drop Tower located at NASA Langley Research Center. The test article was released from a height of 22.9-ft to achieve a vertical impact velocity of 38.4-ft/s (460.8-in/s). A pre-test photograph of the suspended fuselage section is shown in Figure 23(a). The total weight of the test article (fuselage section, lead blocks, and DEA) was 1,212 lb. To prevent excessive flexing during the rigid surface test, the upper fuselage cabin was stiffened by a pair of ±45° woven glass straps. Four fully deployed energy absorbers were attached to the flat bottom surface of the fuselage section using tie-down straps, as shown in Figure 23(b).

Vertical accelerations were measured at six locations on the fuselage floor with accelerometers mounted in the center of selected lead blocks (one accelerometer each on the two front, center, and rear blocks). Accelerometer locations are shown in the photograph of Figure 24(a) and are

depicted in the floor schematic shown in Figure 24(b). Data were collected at 10,000 samples per second. Unfiltered acceleration time histories were used to evaluate the floor-level velocity response and to calculate crush displacements through double integration.

(a) Pre-release photo.   (b) Pre-test photo of test article.

Figure 23. Pre-test photographs of the rigid surface impact test.
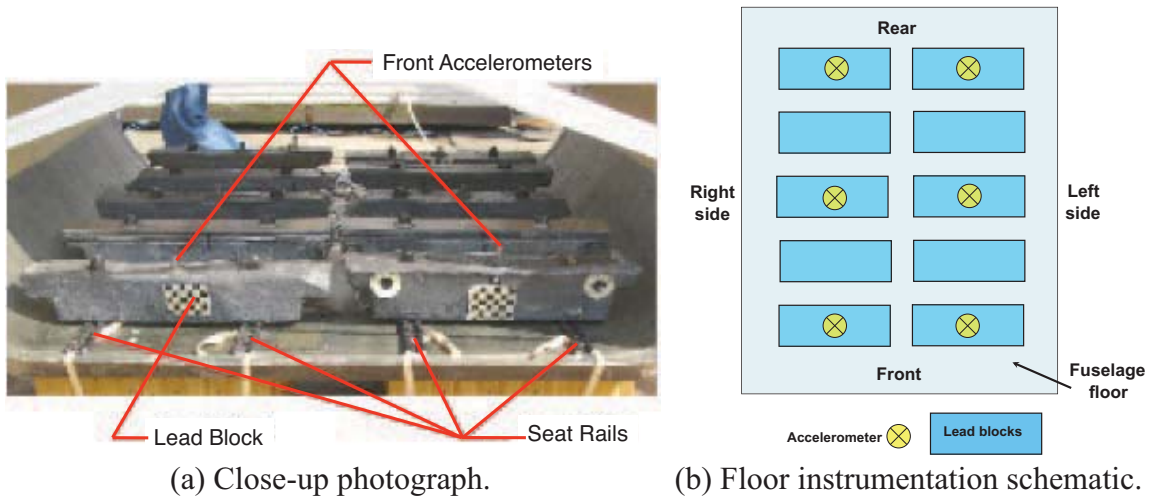
(a) Close-up photograph.   (b) Floor instrumentation schematic.

Figure 24. Instrumentation locations for the rigid surface drop test.

Acceleration-, velocity-, and displacement-time histories are plotted in Figure 25 for four accelerometer locations. As expected of a flat impact, all of the acceleration time histories were similar in magnitude and duration.   Even though initial peak accelerations of 30- to 35-g were recorded, as shown in Figure 25(a), an average acceleration of 18.5-g is obtained over the pulse duration of 0.0-0.06 second. Thus, the energy absorber design crush load was achieved. A small rebound velocity of approximately 100-in/s was measured, as shown in Figure 25(b), indicating that some stored energy was available, likely due to entrapped air, following crushing of the DEA. Maximum displacements ranged from 14.2- to 14.9-in. and were determined through double integration of the acceleration data, as shown in Figure 25(c). These displacement values provide a range of maximum crush strokes between 71-75%, given the pre-test height of 20-in.

(a) Acceleration response.   (b) Velocity response.   (c) Displacement response.
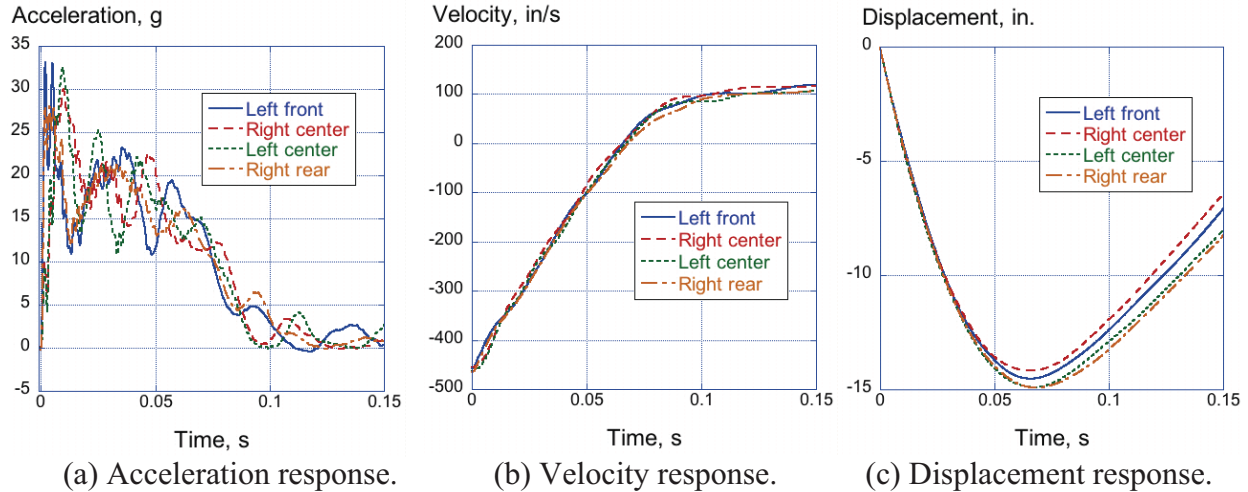
Figure 25. Test results for the rigid surface impact test at four different floor locations.

The energy absorbers for the rigid surface impact test were sized for a 20-g acceleration level. As with most high-speed impacts, the plot of acceleration versus stroke, shown in Figure 26, indicates that the 20-g level was exceeded during the initial part of the crush. Additional pulse attenuation may have been possible through more aggressive shaping of the energy absorbers. For this test, the DEA blocks were shaped with a single radius of curvature of 18-in. The high-speed video coverage of the test indicated that the majority of the fuselage's kinetic energy was dissipated through crushing of the energy absorbers, which crushed progressively to 71-75% of full stroke. A post-impact photograph illustrating the DEA crush response is shown in Figure 27. The accordion-like deformation pattern produced by local buckling of the cell walls of the DEA is evident in the photograph.
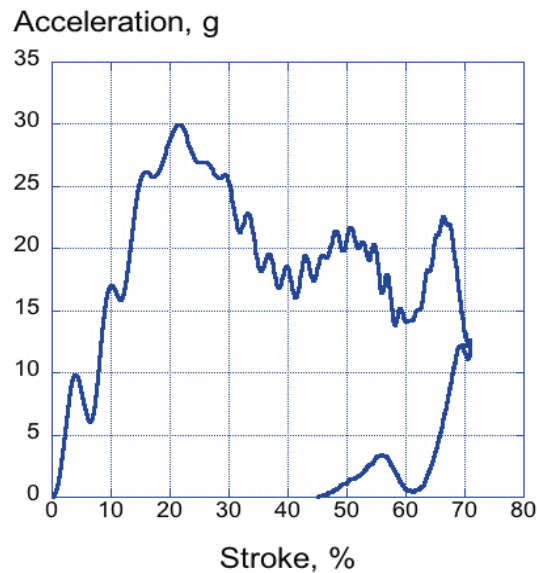
Figure 26. Typical acceleration versus stroke response from the rigid surface impact test.

Figure 27. Post-test photograph illustrating DEA crush response.

3.4.2 Water Impact Test

Two water impact tests were conducted. The first test was performed of the fuselage section with the DEA and the second with no DEA attached. Pre-test photographs of the two test articles are shown in Figure 28. The vertical drop tests were performed by releasing the test articles to impact a 15-ft-diameter pool of water (approximately 42-in. deep) that was placed at the base of the 70-ft drop tower at NASA Langley. The fuselage section without energy absorbers, shown in Figure 28(a), was tested first to provide a datum for comparison with the second test, which included four deployable honeycomb energy absorbers, as shown in Figure 28(b). Each energy absorber was fitted with a cover, fabricated of a single ply of Kevlar®-129 fabric/epoxy that was incorporated into the design of the structure. A close-up photograph highlighting the cover is shown in Figure 29. The energy absorbers were located as close to the edge of the flat portion of the floor as possible and were mounted symmetrically about the mid-surface and centerline of the section.

Each fuselage section was fitted with ten 100-lb lead blocks that were mounted, five per side, to the floor of the fuselage section using standard seat rail fasteners. Accelerometers (250-g maximum range) were mounted on the lead blocks to record the dynamic structural response of the floor, as indicated in the floor plan schematics of Figure 30. For the drop test of the fuselage section without energy absorbers, only two accelerometers were used, one each on the right and left center lead blocks, as shown in Figure 30(a). For the test of the fuselage section with energy absorbers, eight accelerometers were used, as indicated in Figure 30(b). Data were collected at 10,000 samples per second for both impact tests. The experimental data were filtered using an SAE J211 filter with a Channel Filter Class (CFC) 180 [39]. The total weights of the fuselage sections, with and without energy absorbers, were 1,225-lb and 1,200-lb, respectively. The measured velocities at impact were 24.7-ft/s (296.4-in/s) and 25.0-ft/s (300-in/s) for the test with and without energy absorbers, respectively.

(a) Fuselage section without DEA. (b) Fuselage section with DEA.

Figure 28. Pre-test photographs of the test articles.

Figure 29. Close-up photograph showing the cover over the DEA block.
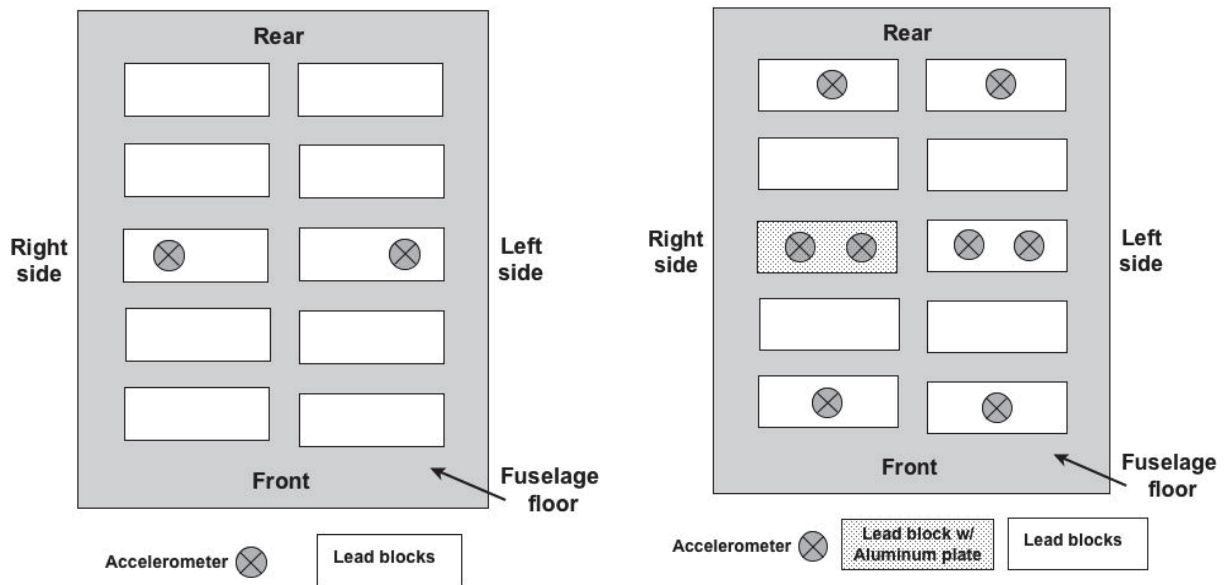
(a) Fuselage section without DEA. (b) Fuselage section with DEA.

Figure 30. Instrumentation plans for two fuselage section drop tests.

23

Acceleration-, velocity-, and displacement-time histories of the right- and left-center lead blocks are plotted in Figure 31 for the water impact test of the fuselage section without DEAs. During this drop test, the measured peak accelerations ranged from 150- to 220-g's with a slight time shift between peaks. Based on the time delay between pulses, it was determined that the fuselage section impacted the water with a 1°-rolled attitude, such that the right side of the fuselage impacted the water first. Post-test damage to the fuselage section consisted of a minor delamination of a single E-glass/epoxy face sheet, which was repaired prior to the second drop test with energy absorbers.

(a) Acceleration response.　　(b) Velocity response.　　(c) Displacement response.
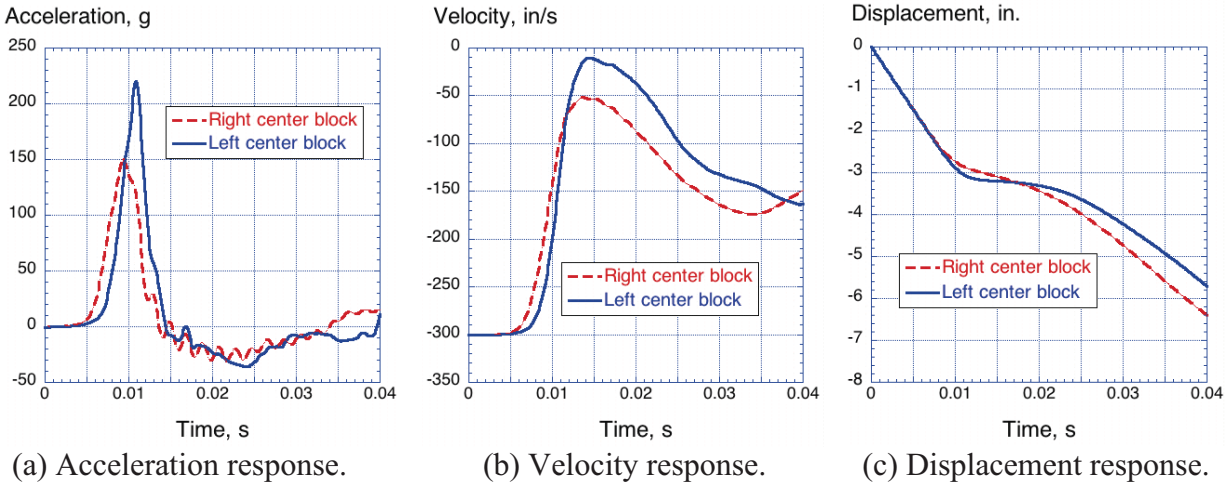
Figure 31. Floor-level responses from the water impact test of the fuselage section without DEA.

Acceleration-time histories are plotted for all eight accelerometer locations in Figure 32 for the water impact test of the fuselage section with DEA. Data from symmetric locations are similar. For example, the left and right center inboard (IB) accelerometer responses, shown in Figure 32(a), are nearly identical, with an initial peak acceleration of 17-g and an initial pulse duration of 0.0225-seconds. The initial peak acceleration is attributed to contact of the DEA blocks with water, while the second large spike in acceleration, that is seen in the responses of the four center accelerometers and occurs just prior to 0.06-seconds, is attributed to impact of the bottom surface of the floor with water. An average floor-level acceleration of 9.3-g was determined by averaging the data from all eight accelerometers for a pulse duration of 0.02-s. Unlike the previous rigid surface test in which all of the acceleration traces were similar, significant differences are observed during the water impact test based on accelerometer location. The front and rear acceleration responses, shown in Figures 32(c) and (d), respectively, exhibit a large initial peak ranging in magnitude between 34- and 42-g. Following the initial peak, the acceleration responses decrease to approximately 7-g and exhibit an oscillatory response. This behavior is quite different than the responses exhibited by the center lead blocks.

(a) Center inboard (IB) accelerometers.

(b) Center outboard (OB) accelerometers.

(c) Front accelerometers.

(d) Rear accelerometers.
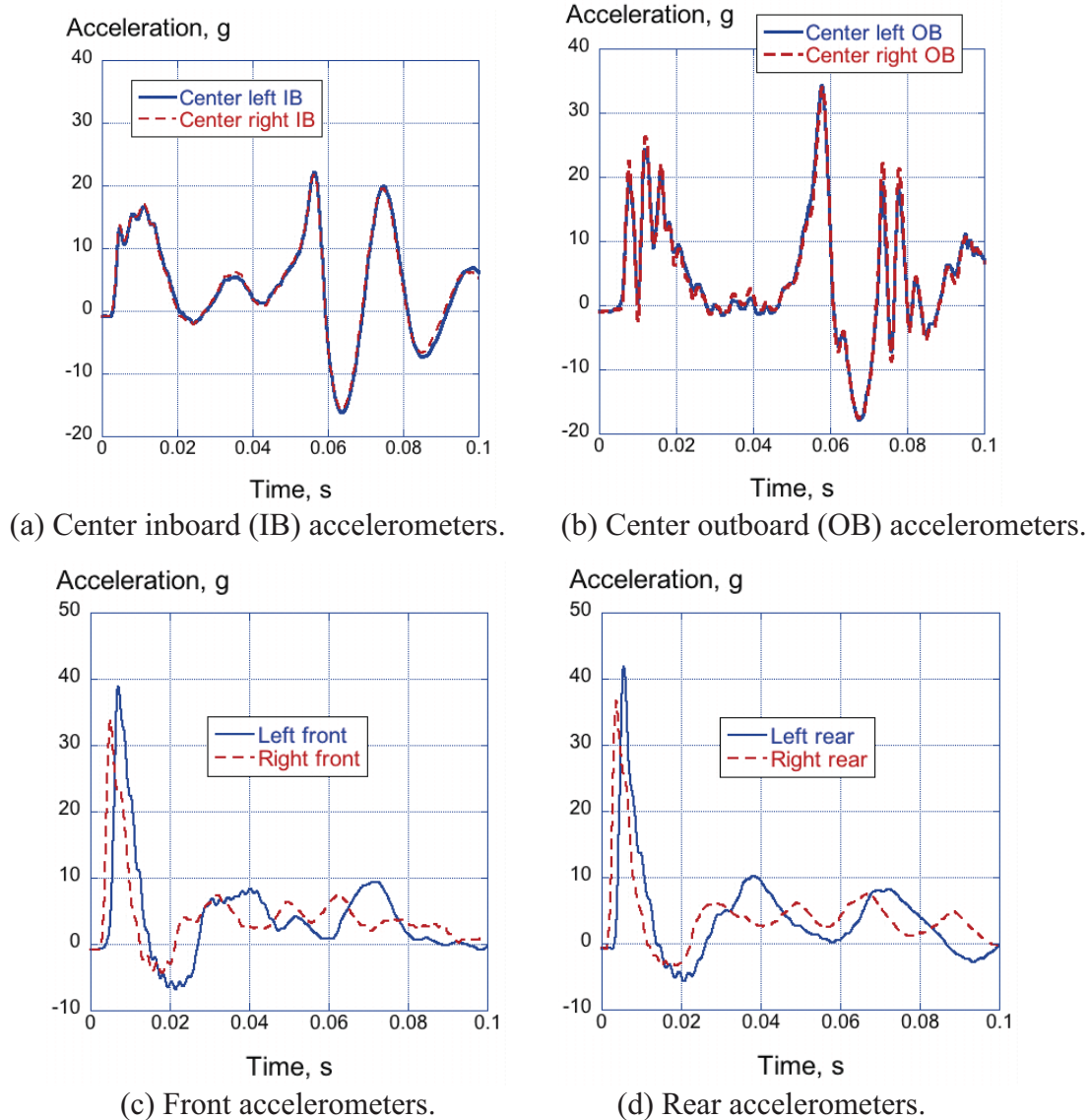
Figure 32. Acceleration time histories from the water impact test.

The acceleration-, velocity- and displacement-time histories of the center left and right IB accelerometers are plotted in Figure 33, highlighting the initial portion of the pulse. By 0.04-seconds, the initial velocity has been reduced by less than 100-in/s. For water impact, the initial pulse, as the structure breaks the surface of the water, is of short duration, or approximately 0.02-second, for this test. However, the total pulse duration, approximately 0.4-seconds, is fairly long and represents the time required for the structure to impact the bottom of the pool. Less than 1-in. of crush of the energy absorbers was observed post-test, which indicates that energy absorption was achieved primarily by momentum transfer to the water, rather than from honeycomb crushing. The peak floor-level acceleration for the center lead blocks was reduced significantly in comparison to the test without DEA (17-g versus 150- to 220-g). This reduction is attributed to the reduced cross-sectional area and the curved bottom surfaces of the DEA in comparison with the flat bottom of the fuselage floor.

| (a) Acceleration responses. | (b) Velocity responses. | (c) Displacement responses. |
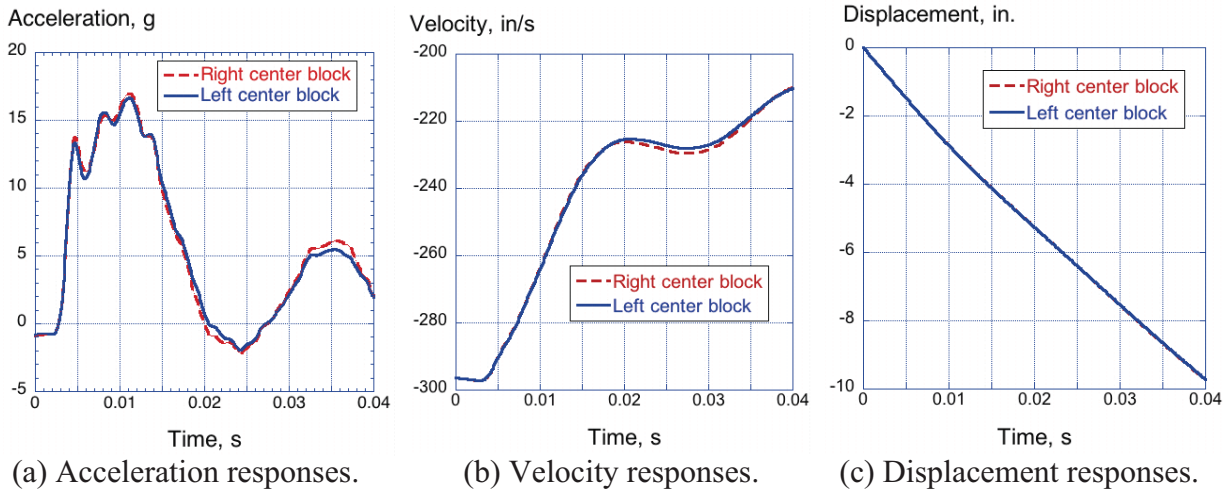
Figure 33. Floor-level responses from the water impact test of the fuselage section with DEA.

3.4.3 Soft Soil (Sand) Impact Test

Prior to the soft soil impact test, a 12-ft x 12-ft wooden box, filled to a height of 2½-ft with high-grade "washed" sand, was installed beneath the drop tower at NASA Langley. Pre- and post-test photographs of the test article are shown in Figures 34(a) and (b), respectively. As with the previous tests, four blocks of DEAs were mounted beneath the floor of the composite fuselage section, as shown in Figure 34(a). A single layer of Kevlar® fabric was used to cover the bottom surfaces of the DEA blocks to ensure proper load transfer into the cell walls. The fuselage section was instrumented with six accelerometers, one accelerometer attached to the two front, center, and rear lead blocks, to record the structural response of the floor. This instrumentation layout was the same as used for the rigid surface impact, as illustrated in Figure 24(b). Data were collected at 10,000 samples per second. A 37.4-ft/s (448.8-in/s) vertical drop test was conducted using the 70-ft. Vertical Test Tower located at the Landing and Impact Research (LandIR) facility.

Following the impact test, the deployable energy absorbers were removed from the sand and post-test measurements of the depth of the impressions left in the sand were made. A photograph illustrating the measurement technique is shown in Figure 35(a). It was determined that the maximum crater depths ranged from 7- to 9-in. Penetrometer impact tests were conducted from a drop height of approximately 48-in. soon after the fuselage drop test to ensure unaltered soil conditions (moisture content). The intention of the penetrometer tests was twofold: to provide an indication of soil uniformity across the impact surface, and to provide soil characterization in the form of acceleration-time responses to facilitate analytical simulations of the impact surface. The 20-lb. penetrometer had a hemispherical surface with a diameter of 8-in. and was instrumented with a triaxial accelerometer pack. Five locations around the impact area were surveyed using the penetrometer, as shown in Figure 35(b). Maximum penetration depth and acceleration-time histories from the five impacts indicated some variability within the impact area thought to be associated with the fact that the soil was not packed. Measured penetrations were in the range of 3.5- to 5.0-in. deep and the average was 4.45-in.

26

(a) Pre-test photo.   (b) Post-test photo.

Figure 34. Pre- and post-test photographs from the drop test onto sand.

(a) Crater depth measurement.   (b) Penetrometer test locations.
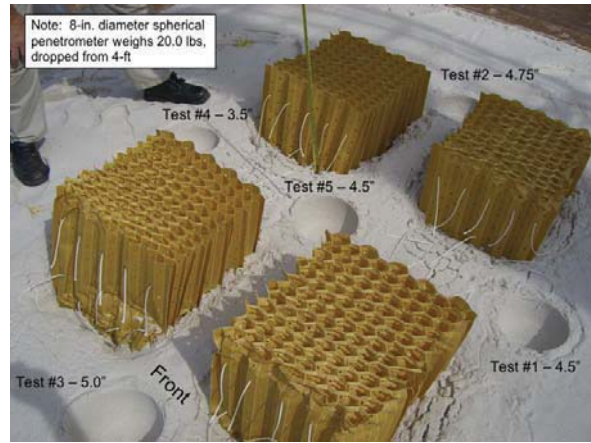
Figure 35. Photographs illustrating post-test measurements.

Unfiltered acceleration-, velocity- and displacement-time histories are shown in Figure 36 for the right and left center lead blocks obtained during the sand impact test. The left side accelerometer exhibits more high frequency oscillations initially than that seen by the corresponding right side accelerometer; however, both responses are similar. The velocity responses of the right and left center blocks are nearly identical and indicate a minimal rebound of approximately 30-in/s, as shown in Figure 36(b). The displacement responses, shown in Figure 36(c), indicate a maximum displacement of approximately 15-in. Based on this value of total vertical displacement, the maximum crush displacement of the DEA blocks can be estimated between 6- and 8-inches, given that the crater depths measured between 7- to 9-in. For comparison, the unfiltered acceleration responses of the front and rear lead blocks are plotted in Figure 37. These responses are similar in shape, magnitude, and duration to the center block responses, shown in Figure 36(a). An average acceleration of 17.5-g was determined for a pulse duration of 0.0- to 0.05-seconds, based on data from all six accelerometers.

Interestingly, the sand acceleration responses are quite similar to the responses obtained for the rigid surface impact, which are plotted in Figure 25(a). Despite the different impact surfaces and complex modes of energy dissipation, the two responses appear to be similar in shape, with the magnitude of the peak acceleration being approximately 2- to 3-g lower for the soft soil impact.

(a) Acceleration response.   (b) Velocity response.   (c) Displacement response.
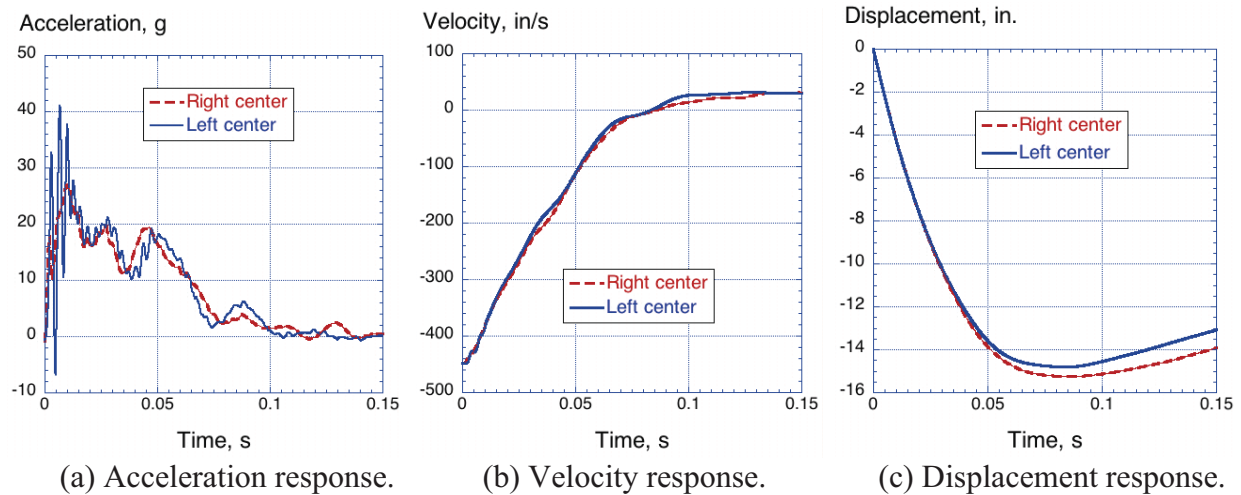
Figure 36. Floor-level responses from the sand impact test of the fuselage section with DEA.

(a) Front accelerometers.   (b) Rear accelerometers.
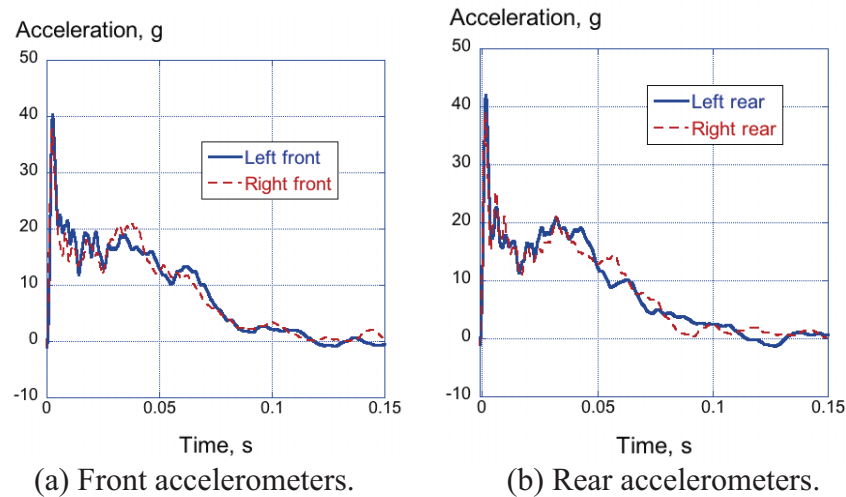
Figure 37. Floor-level responses from the sand impact test of the fuselage section with DEA.

3.4.4 Comparative Results of Multi-Terrain Impact Testing

Acceleration results from vertical drop tests of the composite fuselage section retrofitted with DEA blocks impacting onto a rigid (hard) surface, water, and soft soil (sand) are plotted in Figure 38. Load attenuation through crushing occurred in both hard surface and soft soil impacts. In these cases, the impact surface provided adequate reaction load to initiate and maintain stable crushing. Given that the impact velocity conditions were nearly identical, 38.4- versus 37.4-ft/s, similar acceleration responses were obtained for these two tests, as indicated in Figure 38. However, for water impact, kinetic energy was dissipated primarily by accelerating the displaced water volume. Though effective in attenuating the initial peak, the energy

absorbers were not able to absorb kinetic energy through crushing. This finding is by no means a drawback of the energy absorber but simply a reality associated with water impact. The initial peak-load, which occurs during penetration of the water surface, is too brief to promote sustained crushing. Once the energy absorbers break through the water surface there is simply not enough resistance to maintain crushing [5]. The large difference in peak acceleration measured during the fuselage section drop tests into water with and without the DEA (17-g versus 150- to 220-g) highlights the importance of surface shape and geometry during water impact. Obviously, flat surfaces should be avoided.
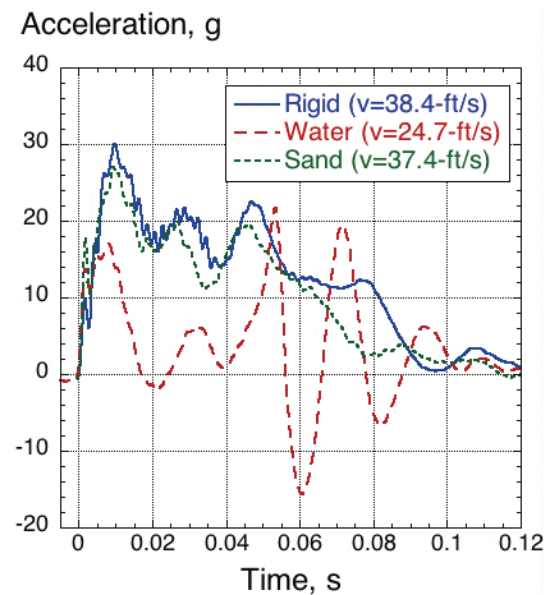
Figure 38. Acceleration responses for rigid surface, water, and soft-soil impact.

A similar fuselage section with an integrated crushable foam subfloor concept and similar payload was used in previous studies to evaluate multi-terrain impact [27, 28, 38]. A photograph of the fuselage section with integrated foam subfloor taken just prior to a 25-ft/s impact onto a hard surface is shown in Figure 39(a), along with a comparable plot of floor-level acceleration responses obtained during multi-terrain impact testing, shown in Figure 39(b). Sareen *et al* [27] studied the response of the fuselage section during 25-fps vertical drop tests onto a hard surface and soft soil (sand) and Fasanella *et al* [28] reported on the response of the same fuselage section during a 25-fps vertical drop on water. Therefore, a loose comparison of the two concepts can be made for corresponding impact surfaces.

For impact on a hard surface (concrete), the deployable honeycomb has a clear advantage over the integrated crushable foam concept. Despite the fact that the kinetic energy at impact for the fuselage with the deployable honeycomb was 2.36 times greater than that of the fuselage with integrated crushable foam, the dynamic loads were attenuated to an average of less than 20-g for the deployable honeycomb as compared to 25-g for the more conventional concept. This advantage is attributed directly to the fact that the externally deployable honeycomb had a greater crush stoke available than the integrated crushable foam.
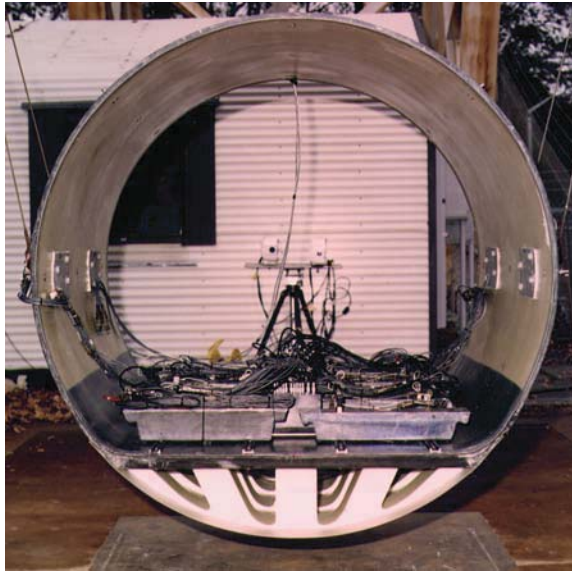
(a) Photo prior to drop test.   (b) Multi-terrain acceleration responses.
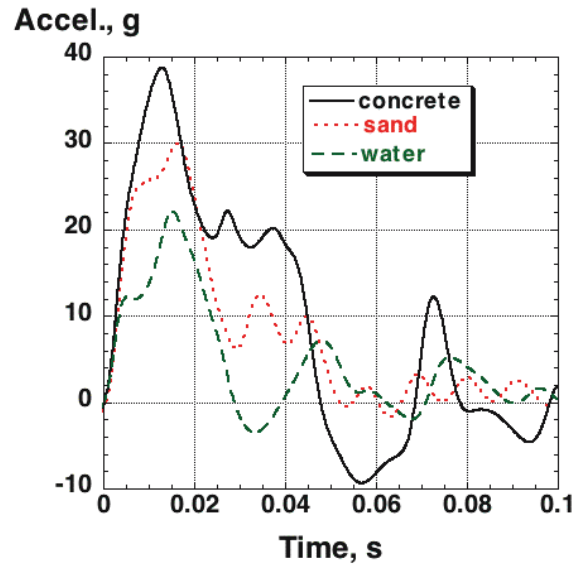
Figure 39. Photograph of fuselage section with integrated foam subfloor and floor-level acceleration responses from multi-terrain impact testing [reprinted from Reference 38].

In the case of the soft soil impact, the deployable honeycomb also exhibited a superior performance over the integrated crushable foam concept. Despite the fact that the kinetic energy at impact for the fuselage with the deployable honeycomb was 2.24 times greater than that of the fuselage with integrated crushable foam, the peak dynamic loads were attenuated to less than 27-g as compared to 31-g. In this case, the honeycomb dissipated energy by both penetration and crushing and maintained a relatively flat response. To the contrary, the kinetic energy of the fuselage with the integrated foam concept was dissipated primarily by soil penetration.

For water impact, stroke availability is less important and the most critical factor is the shape of the impacting object. Consequently, no significant amount of energy was dissipated by honeycomb crushing. Instead most of the kinetic energy was absorbed through the acceleration of the displaced water. With the exception of the initial peak, which was lower for the deployable honeycomb, the two concepts had comparable responses.

These results demonstrate that even for the simple case of vertical impact, designing for multi-terrain impact capability can be extremely complex due to the different, and often opposing, requirements for each impact surface. For example, the cylindrical-shaped nose of the deployable honeycomb was necessary for hard surface impacts in order to attenuate the initial peak [5]. However, for water impact the cylindrical nose promoted faster water-surface penetration (less water resistance) and hence less energy dissipation. Moreover, the large energy absorber depth needed for stroking during hard surface impacts can become a liability in the case of water, or even soft-soil, impacts involving combined vertical and forward velocity conditions. Therefore, designing for multi-terrain impact applications could result in either a significant penalty in energy absorber mass, or reduced energy absorbing capability across multi-terrain surfaces.

4.0 LS-DYNA MODEL DEVELOPMENT AND TEST-ANALYSIS COMPARISONS

The explicit nonlinear transient dynamic commercial code, LS-DYNA [20, 21], was used to perform finite element analyses for each of the tests described in Section 3.0. The initial approach was to develop a robust and accurate material model to represent the behavior of Kevlar®-129 fabric/epoxy based on material property data, then perform test-analysis comparison studies using the single cell three-point-bend tests as a means of calibrating and refining the material model. Once an accurate material model was available, then shell-based finite element models of the DEA components would be developed and validated through comparison with experimental data. The final step would be development of finite element models to represent the multi-terrain impact tests of the composite fuselage section retrofitted with DEA. This building block approach was followed; however, several challenging problems were encountered that required modifications to the approach and expansion of the scope of the research. For example, a probabilistic methodology was implemented to generate input parameters for the LS-DYNA composite material model, for which reliable test data were not available [40]. In addition to the shell-element-based models, solid element models were also investigated, as a potential means of lowering the run times of the simulations and as an alternate modeling approach [41]. The objectives of the simulations were to utilize state-of-the-art nonlinear explicit transient dynamic analysis techniques to develop accurate finite element based models of the DEA; to simulate both normal and off-axis DEA component responses, as well as multi-terrain impacts; and, to demonstrate an analytical methodology that can be used with confidence as a design tool for the DEA.

As computational capabilities continue to improve and the cost associated with test programs continues to increase, certification of future aircraft will rely heavily on computational methods. Reliance on computational tools, however, will only come after rigorous demonstration of their predictive capabilities. NASA under the SRW Rotorcraft Crashworthiness Program is sponsoring the development and validation of such tools [2]. Jackson *et al* in Reference 42 discussed detailed requirements and challenges associated with certification by analysis. Fundamental to the certification effort is the demonstration of verification, validation, and calibration metrics and algorithms for this class of problems. Roach [43], Oberkampf [44], Thaker [45], and Atamturktur [46] have provided accepted definitions of these terms. The process of model calibration, which follows the verification and validation phases, involves reconciling differences between test and analysis. Most calibration efforts combine both heuristics and quantitative methods to assess model deficiencies, to consider uncertainty, to evaluate parameter importance, and to compute required model changes. A particular challenge in model calibration for explicit nonlinear transient dynamic simulations comes because of the computational burden associated with even simple simulations. Long execution times limit the number of solutions obtainable in a timely manner. Oftentimes, calibration efforts are focused on predicting responses at critical locations as opposed to assessing the overall adequacy of the model [47].

Another complication with calibration of nonlinear models is the lack of universally accepted metrics to judge model adequacy. Work by Oberkampf *et al* [48] and later Schwer *et al* [49] are two noteworthy efforts that provide users with metrics to evaluate nonlinear time histories. Unfortunately, seldom does one see them used to assess model adequacy. In addition, the

metrics, as stated in References 48 and 49, do not consider the multi-dimensional aspect of the problem explicitly. The concept of using impact shapes as a metric for multi-dimensional calibration has been proposed by Anderson *et al* [50] and demonstrated by Horta *et al* [47, 51]. Because most applications in this area use commercially available codes, it is assumed that code verification and validation have been addressed elsewhere.

This section of the report is divided into two main sections representing the shell- and solid-element modeling approaches. The shell-element section is subdivided to present: material model development and test-analysis comparisons of the three-point bend testing of single hexagonal cells, dynamic compression testing of multi-cell DEA components, and multi-terrain impact testing of a composite fuselage section retrofitted with DEA blocks. Likewise, the solid-element section is subdivided to present: material model development and test-analysis comparisons for dynamic compression tests of multi-cell DEA components and multi-terrain impact testing. Additional information regarding the analytical simulations may be found in References 40-41, 47, 52-57.

4.1 Shell-Element Modeling of the DEA

4.1.1 Material Model Development

A major challenge in developing a reliable and robust shell-based model of the DEA is to generate an accurate material model to represent Kevlar®-129 fabric/epoxy. The use of shell elements in modeling the thin composite honeycomb provides for a more realistic and accurate representation of the DEA geometry than can be generated using solid elements. In addition, property diminishment of individual plies can be implemented based on damage mechanics models [58]. Success in simulating the crush response of the DEA is highly dependent on accurately modeling the cell wall material and geometry. Modeling of composites has long been complicated by the variety of failure modes they exhibit under compression, such as local buckling, delamination, and tearing. These interacting failure modes often complicate the ability to model the material crush response of the DEA under load. To accurately characterize Kevlar®-129 fabric/epoxy, an LS-DYNA material model was needed with the capability to predict the observed failure mechanisms in the DEA and to demonstrate good functionality when used in conjunction with a shell-element-based model, which best captures the geometry of the DEA. Two materials were investigated: *MAT_LAMINATED_COMPOSITE_FABRIC or Mat 58 and *MAT_PIECEWISE_LINEAR_PLASTICITY of Mat 24 [21].

4.1.1.1 Laminated Composite Fabric Model

The Mat 58 material model was initially chosen based on past success in predicting the impact damage of the Reinforced Carbon-Carbon leading edge panels of the Space Shuttle Columbia [59, 60]. Mat 58 is a continuum damage mechanics material model based on the Matzenmiller-Lubliner-Taylor theory [61] and is intended for use with shell elements to simulate composite tape laminates and woven fabrics. The model requires input of material properties in tension, compression, and shear to define stress-strain behavior within the lamina or laminate. The user specifies the in-plane elastic modulus and Poisson's ratio in two primary directions, designated A and B in LS-DYNA. The maximum strength in tension, compression, and shear is also specified at corresponding strain values. A representation of the stress-strain curve for in-plane

tension is illustrated in Figure 40. The tensile response is initially linear elastic with the modulus specified by EA. Stress increases nonlinearly until XT, the maximum strength, is reached. The nonlinear portion of the response is defined internally by LS-DYNA based on a continuum damage approach. Once XT is reached, the stress is reduced based on the "stress limiting" factor SLIMT1, and is then held constant at the reduced value until elements reach a strain specified by the ERODS parameter in the material model, at which point the elements are deleted and removed from the solution. Similar stress-strain responses are defined for in-plane compression and shear. Additional information on this material model can be found in Reference 21.
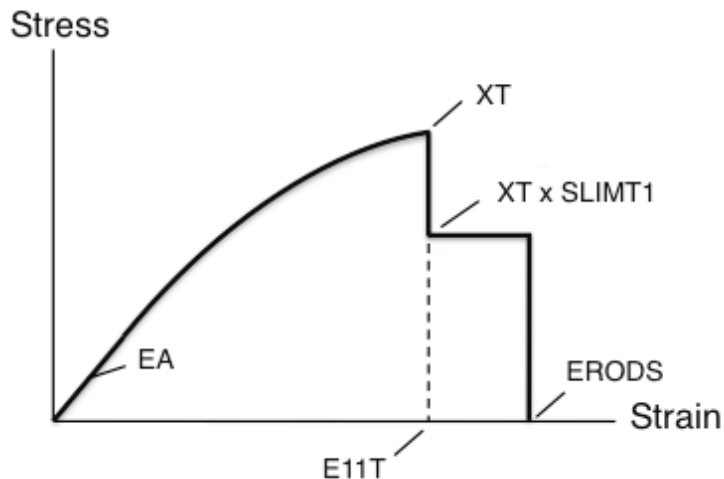
Figure 40. Typical in-plane tension stress-strain curve used for material within Mat 58.

Initial input parameters for Mat 58 were determined based on data obtained from tensile tests conducted on single-ply Kevlar®-129 fabric/epoxy coupons oriented at 0°/90° and ±45º with respect to the loading axis, as plotted in Figures 9 and 10, respectively. All coupons had a nominal thickness value of 0.01 inches. Tensile properties for the model were obtained from 0°/90° tensile data while shear properties were obtained from ±45º tensile coupon tests. The ±45° coupons were pulled in tension at 1-ipm and 20-ipm to assess the effect of strain rate on the stress-strain response, as shown in Figure 11. LS-DYNA material model Mat 158 is capable of representing strain rate effects.   However, the simpler Mat 58 material model was used instead. Input shear property values were based on the 20-ipm test data as being most representative of the response.

Mat 58 properties used in the modeling effort are listed in Table 2. Note that since the Kevlar® material is a plain weave fabric, the modulus in the longitudinal or fiber direction (EA) is the same as the modulus for the transverse direction (EB). The Mat 58 material card requests input of the Poisson's ratio in the BA direction, as opposed to the more standard AB direction. The Poisson's ratio in the BA direction can be derived from the ratio of EB to EA multiplied by the Poisson's ratio in the AB direction. However, since EA=EB, the two values of Poisson's ratio are the same. Typically, compressive strengths of Kevlar® materials are considerably lower than their corresponding tensile strengths. Reference 62 states that "when a laminate using Kevlar® reinforcement is loaded in compression…the individual fibrils buckle and split away from the bundle when the stress exceeds about one-fifth of what it would take in tension." Since no compressive testing was performed, a range of compressive strength values from 7,500- to

16,000-psi was considered. The value of 16,000-psi was based on 1/5 the tensile strength of 80,000-psi for the 0°/90° data. A low value of compressive strength of 7,500-psi was based on the approximate yield stress of the ±45° coupons. With Mat 58, a compressive strength value of 10,000-psi provided the best fit to both the static single cell and the dynamic DEA component test data.

Table 2. Mat 58 material properties used to represent the Kevlar[®]-129 fabric.

Material Property Description	Symbol	Values
Density, lb-s^2/in^4	RO	1.29E-4
Young's modulus longitudinal & transverse direction, psi	EA, EB	1.3E+6
Poisson's ratio	PRBA	0.3
Stress limit of nonlinear portion of shear curve, psi	TAU1	Not used
Strain limit of nonlinear portion of shear curve, in/in	GAMMA1	Not used
Shear modulus AB, BC, and CA, psi	GAB	1.54E+5
Min stress factor for limit after max stress (fiber tension)	SLIMT1	0.8
Min stress factor for limit after max stress (fiber comp)	SLIMC1	1.0
Min stress facto for limit after max stress (matrix ten)	SLIMT2	0.8
Min stress factor for limit after max stress (matrix comp)	SLIMC2	1.0
Min stress factor for limit after max stress (shear)	SLIMS	1.0
Material axes option (model dependent)	AOPT	
Maximum effective strain for element layer failure	ERODS	10.0
Failure surface type	FS	1.0
Strain at longitudinal compressive strength, in/in	E11C	0.02
Strain at longitudinal tensile strength, in/in	E11T	0.05
Strain at transverse compressive strength, in/in	E22C	0.02
Strain at transverse tensile strength, in/in	E22T	0.05
Strain at shear strength, in/in	GMS	0.02
Longitudinal and transverse compressive strength, psi	XC, YC	10,000.
Longitudinal and transverse tensile strength, psi	XT, YT	80,000.
Shear strength, psi	SC	5,000.

4.1.1.2 Piecewise Linear Plasticity Material Model

Due to initial difficulty in characterizing the DEA material response, a less complex material model was sought to represent Kevlar[®]-129 fabric/epoxy. Thus, Mat 24, known as *MAT_PIECEWISE_LINEAR_PLASTICITY, was chosen [21]. In the model, the user can specify the elastic modulus, Poisson's ratio, yield stress, and tangent modulus of the material. The user can also input an effective stress versus effective plastic strain curve that defines the isotropic material response. Material property values used in Mat 24 to represent Kevlar[®]-129 fabric/epoxy are listed in Table 3 and the input stress-strain curve, which was based on the average tensile responses of ±45° coupons at 20-ipm, is shown in Figure 41. The higher strain rate curve was used since the material model application will involve high strain rates. Also, it should be noted that the tangent modulus listed in Table 3 was set to zero in this case, indicating that the plastic response of the material was defined by the input stress-strain curve. Finally, the compressive response was assumed to be equivalent to the tensile response for the initial portion of the curve. Also, since crushing of the Kevlar[®]-129 fabric/epoxy occurs for material oriented

at ±45°, the rational seemed logical for modeling cases where the high tensile strength does not come into play.

Table 3. Property values used in Mat 24.

Parameter No.	Symbol	Description	Value
1	E (psi)	Young's modulus	340,000
2	PRBA	Poisson's Ratio	0.3
3	SIGY (psi)	Yield stress	7,500
4	ETAN (psi)	Tangent modulus	0
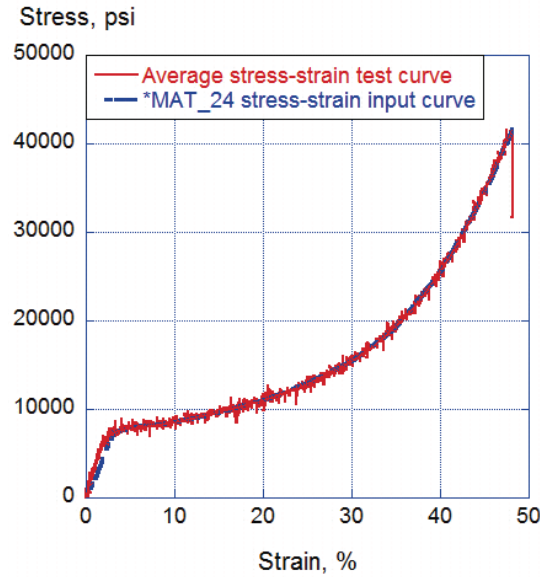
Figure 41. User-defined stress-strain input curve for Mat 24.

4.1.2 Simulation of the Three-Point Bending Tests

Even though the single cell specimen was loaded quasi-statically, a slowly-loaded dynamic finite element model was executed using LS-DYNA v971 for the sole purpose of verifying the input material properties for Mat 58, which will be used in future simulations of the energy absorber. A picture of the complete model is shown in Figure 42. The model consists of three major parts: three "Bakelite" stanchions, the deformable composite cell wall, and the flanges. These parts are shown separately in Figure 43. The cell dimensions were cell-wall width (W) = 1.0-in., cell-wall thickness (t) = 0.01-in. and overall length equal to 4.21-in. The model was constructed using a nominal element edge length of 0.05-in.

The walls of the single hexagonal cell were represented using Mat 58 with the property values shown in Table 2. The flanges consisted of two layers of fabric, with a specified nominal thickness of 0.02-in. However, measured thicknesses ranged between 0.03- to 0.04-in., which included areas of excessive adhesive. The ±45° ply orientations were defined using the *SECTION_SHELL and *INTEGRATION_SHELL cards in LS-DYNA. The Bakelite stanchions were represented using a linear elastic material with a density of 1.356E-4 lb-s^2/in^4,

an elastic modulus of 1.09E+6-psi, and a Poisson's ratio of 0.25. The complete model consisted of 27,098 nodes; 12,000 hexagonal solid elements; and 13,600 Belytschko-Tsay shell elements.
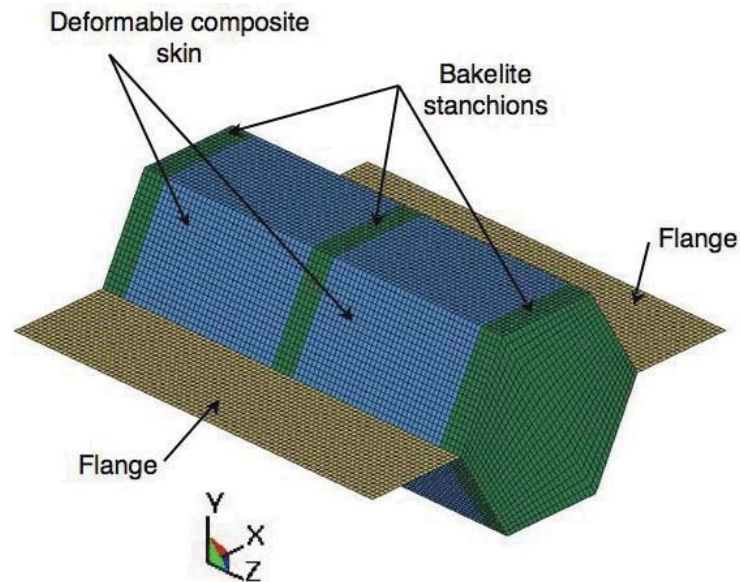
Figure 42. Single cell model for 3-point-bend test.

(a) Hexagonal stanchions (Bakelite).   (b) Deformable skin.

(c) Flanges.
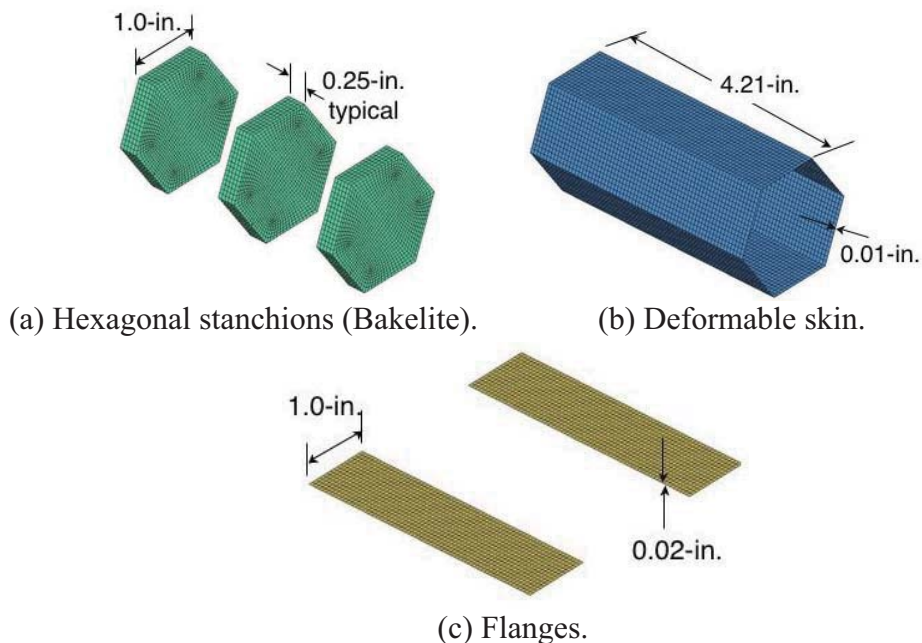
Figure 43. Three distinct parts of the LS-DYNA model with nominal dimensions.

The test specimen was loaded in three-point bending by applying a compressive load at the center of the hexagonal cell using a 0.25-in. wide bar, as shown in Figure 12(a). In the test, loading was performed in displacement control at a rate of 2.0-ipm. The reaction points (0.25-in. from the bottom edge) were simply supported. A *BOUNDARY_SPC_SET was defined in the model to represent the simply supported boundary conditions. For this set, nodes within the

0.25-in. by 0.75-in. area at the bottom of both ends of the specimen were constrained from linear motion in the x- and y-directions.   The constrained nodes were free to move only in the z-direction (no friction assumed), and free to rotate.   Note that the axis directions are shown in Figure 42.

To represent the three-point loading condition, all of the nodes within the 0.25-in. by 0.75-in. loading area at the top center of the cell were assigned a *LOAD_NODE_SET condition. This condition specified that at 0.0-seconds the load was 0.0-lb.   At the termination time, the maximum load per node was 2.1825-lb. Note that 2.1825-lb times 126, which is the number of nodes included in the set, equals 275-lb, which is slightly over the maximum load observed in the test.   The simulation was conducted with a termination time of 0.1-second.   In this simulation, time serves as a scale factor for load, with the maximum loading applied at the end time. Since the tests were performed under quasi-static loading, a fairly long end time was selected for the simulation to minimize impulsive loading effects.   The kinetic energy time history responses of the various parts within the model were monitored to ensure that a quasi-static loading was applied. The model was executed using double precision LS-DYNA v971 and required approximately 3 hours clock time to simulate 0.1 second of simulation time.

4.1.2.1 Results for the Laminated Composite Fabric Model
As described previously, the three-point-bend study involved four scaled (same L/W) cases (W= 0.75-in., 1.0-in., 1.25-in. and 1.5-in.). Since specimens were scaled, only one was chosen for simulation and comparison with experiment. Five individual tests were conducted on single-cell specimens with width equal to 1.0-in. and length equal to 4.21-in. as shown in Figure 14(a). The upper- and lower bound test responses from these three-point-bend experiments are plotted with the LS-DYNA predicted response in Figure 44.   The model follows the upper bound of the test data to 100 pounds. Then, as damage accumulates in the model and small buckles form, the predicted load falls below the lower bound test limit at a displacement of 0.05 inches.   Finally, after 0.08-in. of displacement, the model predictions are within the experimental range. The response of the "paper-thin" material with nominal thickness of 0.01-in. is difficult to predict as the actual thickness varied due to epoxy variations and glue over-run at the support blocks. Parametric studies showed that boundary conditions and thickness variations of only 0.001-in. made a significant difference in model results.

Initial buckling of the top surface on each side of the center support at a load of 160-lb and at a corresponding displacement of 0.045-in. is depicted in the fringe plot of Figure 45. These two buckles were created at slightly different times and correspond to the two drops in load of approximately 10 pounds seen in Figure 44. The buckling in the model corresponds to buckling observed in the test article in the same region. The diagonal bands on each side of the center support illustrate the high shear loading in the bottom half of the cell. In three-point bending, the top surface of the hexagonal cell is subjected to high compressive loads, while the bottom surface is subjected to high tensile loads. Consequently, the test specimens exhibit initial instability in the form of compressive and shear buckling, as shown in Figure 12(a).   The deformed specimen is shown in Figure 46 near the end of the simulation at a displacement of 0.1-in. The test specimens do not collapse after maximum loading is achieved and exhibit a complex unloading response. No attempt to model the unloading was made. Finally, Horta [40] conducted a study utilizing a Response Surface Methodology (RSM) to assess the influence of

parameter uncertainty in the Mat 58 material model on the three-point bend response of a single-cell. Unfortunately, the compressive stress range investigated by Horta was much higher than what was finally determined to be correct. Consequently, Horta's model predicted the three-point bend response quite well, but was unsuitable for the DEA component simulations, which required a lower compressive strength to capture the crushing behavior.
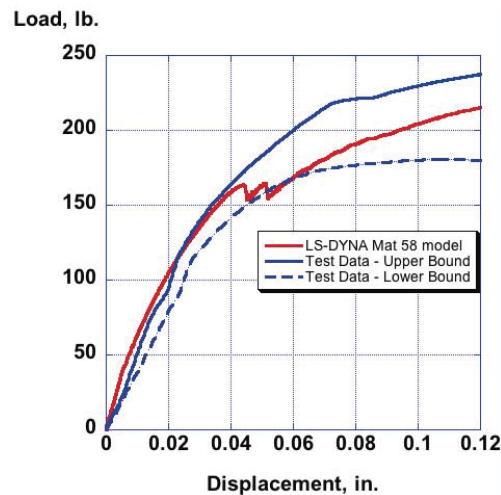
Figure 44. Test/analysis correlation for three-point-bend test.
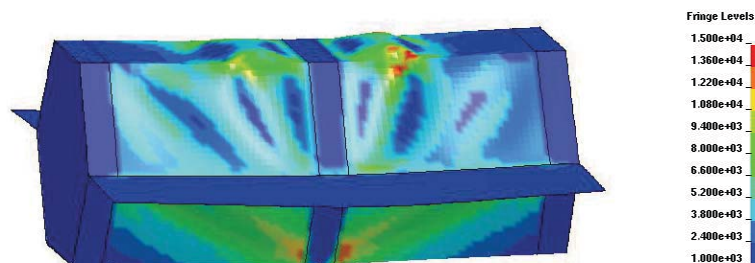
Figure 45. Fringe plot of Von Mises stress for a displacement of 0.045-in. Fringe levels are in psi.
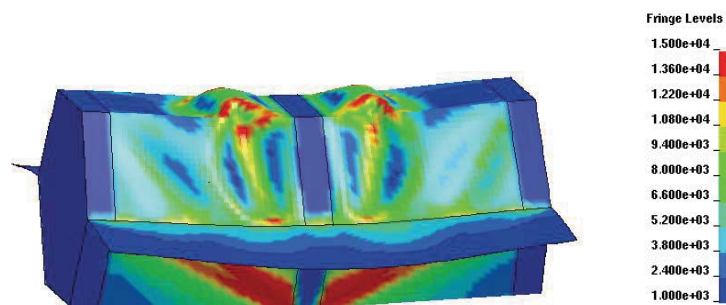
Figure 46. Fringe plot of Von Mises stress for a displacement of 0.1-in.

4.1.2.2 Results for the Piecewise Linear Plasticity Model

The Mat 58 material model was replaced in the existing single-cell model for W=1.0-in. with the Mat 24 piecewise linear plasticity model. As a reminder, the Mat 24 model is based on the tensile stress-strain response of the ±45° Kevlar®-129 fabric/epoxy coupons. The boundary

38

conditions described previously for the single-cell models remained the same. The angle layup within *SECTION_SHELL was removed since the model did not assume definition of a composite, but the *INTEGRATION_SHELL cards, setup for Mat 58, remained intact. Use of this isotropic material model led to softer behavior and lower strength of the three-point bend response due to a lower input Young's modulus and a yield stress value of only 7,500-psi for both compression and tension. The response of the single cell is dominated by the tensile behavior in the lower half of the cell. A comparison of the structural response using the two material models is shown in Figure 47. Although Mat 24 performed poorly in correlating with the experimental three-point bend test data, it was evaluated further in simulations of the dynamic crush response of the DEA components due to the compression-dominated nature of those tests.
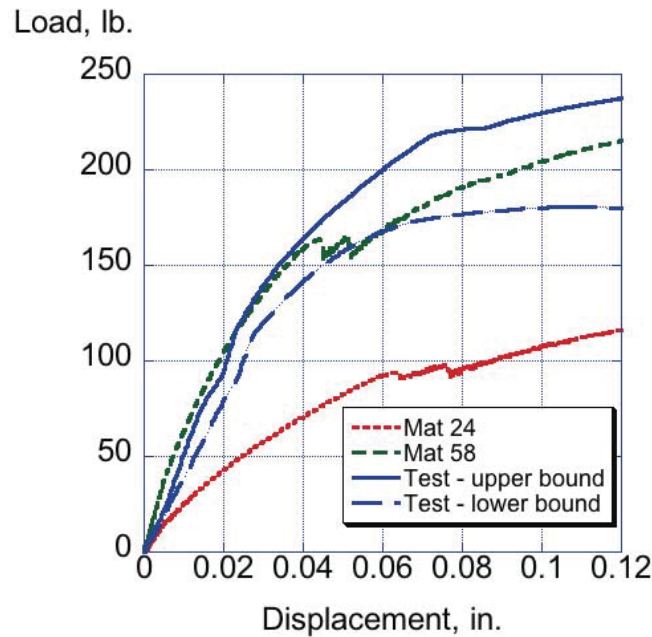
Figure 47. Test/analysis correlation of single cell using Mat 58 and Mat 24 models in LS-DYNA.

4.1.3 Simulation of the DEA Multi-Cell Component Tests

Dynamic crush tests of multi-cell honeycomb components were simulated using Mat 58 and Mat 24 in LS-DYNA to represent the Kevlar®-129 fabric/epoxy cell walls. Shell-element-based models were developed to represent the 59- and 104-cell DEA components whose cells were oriented along the loading direction (normal), and the 68-cell DEA component in which the cells were canted by 27° with respect to the loading direction (off-axis). The finite element models of these DEA components are shown in Figure 48. All models consisted of four parts, including an impact block used to crush the DEA, a reaction surface placed under the honeycomb, one part for plies within the DEA having a thickness of 0.01-in., highlighted in blue, and another part defined for double plies with a 0.02-in. thickness, highlighted in green. Like the single-cell models, the *SECTION_SHELL and *INTEGRATION_SHELL cards were used with Mat 58 to specify the ±45° ply orientations of the composite cell walls.

39

For each simulation, the impact blocks were assigned a vertical impact velocity to match the test conditions, which are listed in Table 1. Gravitational loading was included in all models. A contact definition of *CONTACT_AUTOMATIC_SINGLE_SURFACE was used to represent contact between the impact block and the DEA, between the DEA and the reaction surface, and for internal contact between elements within the DEA. A coefficient of friction of 0.35 was used and the SOFT parameter in the contact definition was set to 1, for soft-to-hard material contact. All nodes on the impact surface were fully constrained using the *BOUNDARY_SPC_SET. The impact surface and impact block were both modeled as *MAT_RIGID in LS-DYNA. The nominal edge length of the shell elements used to create the DEA models was 0.25 inches. Information on all three DEA component models is listed in Table 4.

(a) 59-cell DEA component.

(b) 68-cell DEA component, 27° off-axis.

(c) 104-cell DEA component.   (d) 104-cell DEA component (isometric view).
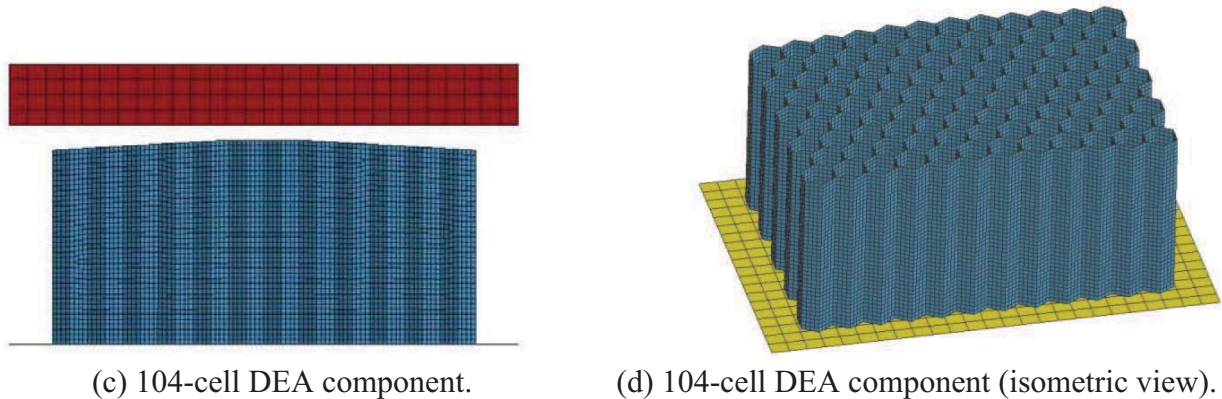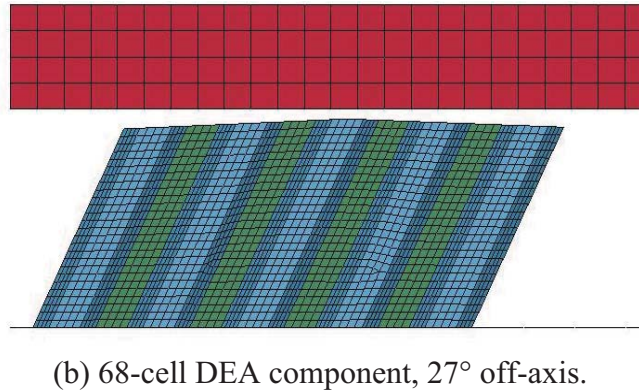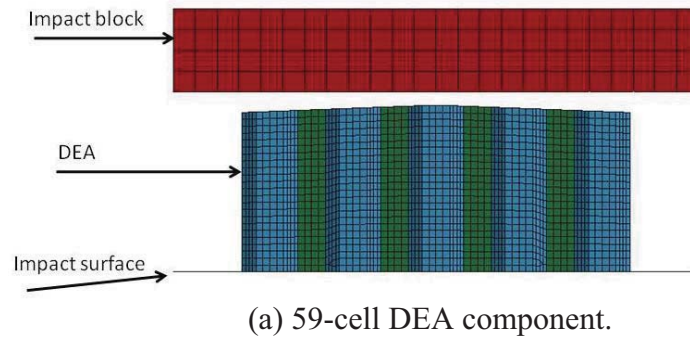
Figure 48. Pictures of the shell element DEA component models.

Table 4. Multi-Cell DEA component model information

Property	59-Cell	104-Cell	68-Cell
Number of nodes	22,161	53,329	27,435
Number of solid elements	1,920	2,240	1,920
Number of shell elements	20,096	56,052	25,515
Number of parts	4	4	4
Number of Linux-based processors	4	4	4
Approximate run time, minutes	19	87	22
Termination time, s	0.06	0.06	0.1

Prior to presenting the test-analysis results, it is important to specify the calibration metrics used to assess the level of agreement. For the dynamic crush tests of the DEA components, test-analysis comparisons are presented for four parameters: initial peak acceleration, average acceleration over a specified time duration, average crush stress calculated from the average acceleration, and peak compaction acceleration. In addition, plots showing unfiltered test and unfiltered predicted acceleration time history responses are provided. These metrics were selected based on the stated design goal for the DEA. The level of agreement between test and analysis is evaluated based on a simple percentage difference approach, where agreement within ±15% is considered good.

4.1.3.1 Results for the 59-Cell DEA Component Test

Both Mat 58 and Mat 24 material models were used to represent the Kevlar$^®$-129 fabric/epoxy cell walls in the shell-based model of the 59-cell DEA crush test. The material properties listed in Table 2 were used for Mat 58, while the material properties listed in Table 3 were assigned to Mat 24. A plot of experimental and predicted acceleration time history responses are shown in Figure 49 and correlation metrics are listed in Table 5. The acceleration response of the model with Mat 58 properties closely follows the test data up to 0.0175-seconds. The predicted acceleration response then exceeds the test data by about 2-3 g's for 0.015-seconds, which slowed the impact block enough to make the predicted compaction peak only 30-g as compared to 64.4-g for the test.

In comparison, the model that was executed with Mat 24 accurately predicted the initial peak acceleration and the uniform crush response up to 0.015-seconds. This model demonstrated a slight compaction response; however, the magnitude of the predicted acceleration peak during compaction was under predicted (27.4-g for the model compared with 64.4-g for the test). As listed in Table 5, the Mat 58 model generally showed better agreement with the test than did Mat 24, though neither model did a good job of predicting the peak compaction acceleration. Note that average stress values for the tests, shown in Table 5, may differ from those shown in Figure 21, due to the fact that the calculations in Figure 21 were strain based (0- to 0.6-in/in), whereas the values shown in Table 5 are based on time (0- to 0.03-s). Predicted DEA crush patterns are shown in Figure 50 at a time of 0.012-seconds. At that time in the simulation, the DEA is being crushed in a stable and uniform manner and compaction has not been reached. The two deformation patterns are similar and indicate folding of the cell walls, as well as a tendency for the outer cells to deform inwardly, towards the center of the component.

Figure 49. Comparisons of test and analysis for 59-Cell DEA acceleration-time responses.

Table 5. Test-Analysis Correlation Metrics for the 59-Cell DEA Component Models.

Parameter	Test	Mat 24		Mat 58	
		Value	Percentage Difference	Value	Percentage Difference
Initial peak acceleration, g	12.4	12.2	1.6	13.7	-10.5
*Average acceleration, g	7.1	9.7	-36.6	7.8	-9.9
Average crush stress, psi	16.9	22.3	-32.0	18.3	-8.3
Compaction peak, g	64.4	27.4	57.5	30.0	53.4

* Average acceleration computed over time interval of 0.0-0.03 seconds.
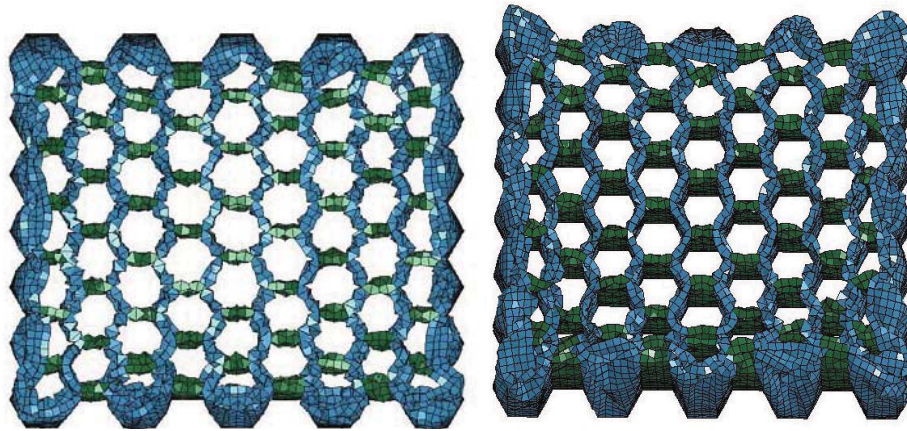
(a) DEA crush patterns using Mat 24   (b) DEA crush patterns using Mat 58

Figure 50. Comparisons of predicted DEA crush at 0.012-s using Mat 24 and Mat 58.

4.1.3.2 Results for the 104-Cell DEA Component Test

As with the 59-cell DEA component, both material models (Mat 58 and Mat 24) were used to represent the Kevlar®-129 fabric/epoxy cell walls in the shell-based model of the 104-cell DEA crush test. Again, the material parameters listed in Table 2 were used for Mat 58, while the

material properties listed in Table 3 were assigned to Mat 24. Experimental and predicted acceleration time history responses are plotted in Figure 51 and correlation metrics are listed in Table 6. Both the Mat 58 and Mat 24 models accurately predict the average acceleration and crush stress within ±12%; however, neither model does a good job of matching the initial peak acceleration. In addition, the Mat 58 predicted response matches the unloading slope of the experimental curve near the end of the pulse. In comparison, the model that was executed with Mat 24 material properties exhibits a slight compaction acceleration starting at 0.035-s that is not present in the test data.
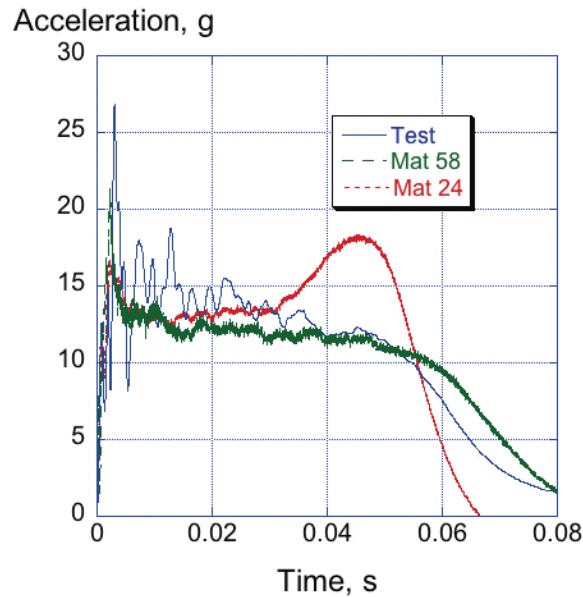
Figure 51. Comparisons of test and analysis 104-Cell DEA acceleration-time responses.

Table 6. Test-analysis correlation metrics for the 104-cell DEA component models.

Parameter	Test	Mat 24		Mat 58	
		Value	Percentage Difference	Value	Percentage Difference
Initial peak acceleration, g	26.8	16.8	37.3	21.3	20.5
*Average acceleration, g	14.3	13.0	9.1	12.7	11.2
Average crush stress, psi	22.1	20.2	8.6	19.8	10.4
Compaction peak, g	-	18.0	-	-	-

*Average acceleration computed over time interval of 0.0-0.03 seconds.

The correlation metrics listed in Table 6 indicate that neither material model predicts the initial peak acceleration of the test response well. However, over the first 0.03 seconds, the average acceleration of the Mat 24 model (13-g) is slightly closer to the test average of 14.3-g and the predicted average crush stress is also closer to the test (20.2-psi for the model compared with 22.1-psi for the test) than for the Mat 58 model. However, both models predict the uniform crushing response of the test within 12%. After 0.03 seconds, the Mat 24 model deviates from the test data and shows a compaction peak, while the Mat 58 remains closer to the test data. Thus, visual inspection of the test-analysis comparison plot is as important, in this case, as the individual correlation metrics in evaluating the performance of the material model.

4.1.3.3 Results for the 68-Cell DEA Component Test

As with the 59- and 104-cell DEA component models, both materials (Mat 58 and Mat 24) were used to represent the Kevlar®-129 fabric/epoxy cell walls in the shell-based model of the 68-cell off-axis DEA crush test. Experimental and predicted acceleration time history responses are plotted in Figure 52 and correlation metrics are listed in Table 7. For this simulation, the model with Mat 58 properties matches the initial peak magnitude and the uniform crush response within ±2% of the test. The acceleration peak at compaction is over predicted by about 6-g (33.9-g versus 27.7-g for the test) and occurs approximately two milliseconds before the test peak occurs.   In comparison, the model that was executed with Mat 24 material properties over predicts the initial peak acceleration by approximately 7-g, but predicts the subsequent reduction in acceleration attributed to outer cell buckling, and the compaction response of the component. The magnitude of the peak acceleration during compaction is over predicted (29.8-g compared with 27.7-g for the test) and the predicted compaction peak occurs earlier in time than the test peak. Early compaction occurs in the simulation with Mat 24 due to global buckling of the cell walls.
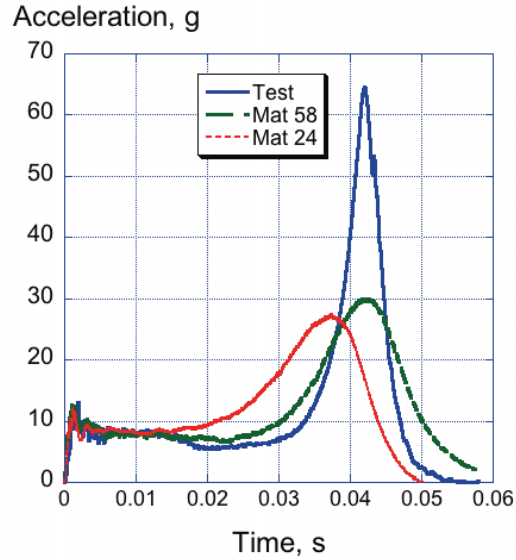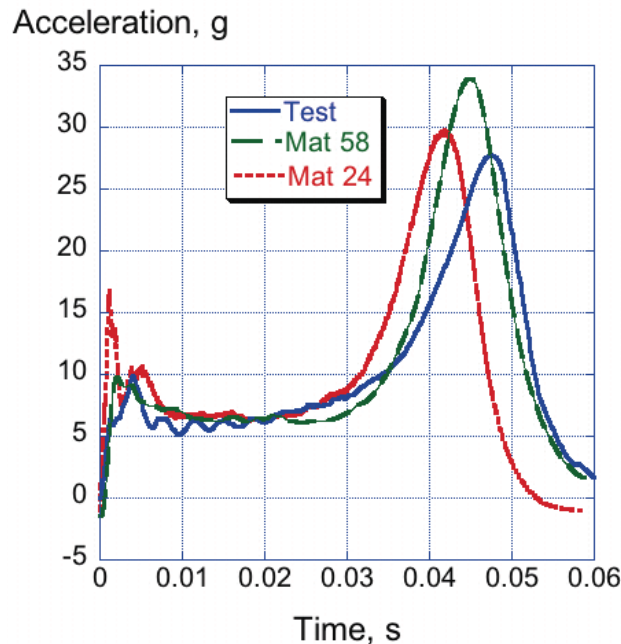

Figure 52. Comparisons of test and analysis 68-cell canted DEA acceleration-time responses.

Table 7. Test-analysis correlation metrics for the 68-cell DEA component material models.

Parameter	Test	Mat 24		Mat 58	
		Value	Percentage Difference	Value	Percentage Difference
Initial peak acceleration, g	9.9	16.8	-69.7	9.7	2.0
*Average acceleration, g	6.5	7.6	-16.9	6.6	-1.5
Average crush stress, psi	16.0	18.3	-14.4	16.2	-1.3
Compaction peak, g	27.7	29.8	-7.6	33.9	-22.4

* Average acceleration computed over time interval of 0.0-0.03 seconds.

44

As indicated in Table 7, the Mat 58 model predicts the initial peak acceleration and the uniform crushing response of the 68-cell DEA component within ±2%. Percentage differences for the model with Mat 24 are considerably higher. However, the Mat 24 model predicts the magnitude of the compaction peak within 10%.

4.1.3.4 Discussion of DEA Component Simulation Results

The complex combined loading mechanisms in tension, compression, and shear within the Kevlar®-129 fabric/epoxy make it extremely difficult to characterize the crushing response of the DEA components. Tension and compression stress-strain responses and strengths are highly dependent on fiber orientation. Consequently, it is difficult to find a single material model that can accurately represent both the linear response to failure of the 0°/90° Kevlar®-129 tensile test and the highly nonlinear response of the ±45° Kevlar®-129 tensile test, which exhibited matrix failure, scissoring, and high strain-to-failure. Thus, approximations must be made, and the material model chosen will not likely represent all loading conditions equally well. For example, plasticity in compression was simulated in Mat 58 by setting the SLIM parameter to 1. However, strain hardening, if present, must be neglected.

The Mat 58 model, which made use of both 0°/90° and ±45° tension test data, as well as an estimated compression strength, was able to predict the loading of the three-point bend test. But, the buckling that was predicted by the Mat 58 model was somewhat exaggerated, which resulted in larger reductions in load than was measured. The load-displacement response of the single hexagonal cell under three-point bending was not captured when Mat 24 material properties were used, since the material stress-strain behavior was generated by inputting the ±45° tensile coupon response directly. While Mat 24 performed well in predicting the crush response of the DEA components, one must use caution when characterizing an orthotropic material as isotropic in a finite element model. In these simulations, the defined stress-strain response of the composite fabric was obtained from ±45° tensile test data, which gave a reasonable approximation of the crushing response. However, if the DEA were subjected to a more complex loading scenario, especially involving transverse or combined loading, this material model may not be appropriate.

Through examination of model data, the compression strength of the Kevlar®-129 fabric/epoxy material needs to be accurately characterized in Mat 24 to better capture the crush response. Unfortunately, no viable data were collected in compression due to the high degree of difficulty in overcoming buckling effects. Even with these considerations, as observed by comparing analysis with test data, both the Mat 24 and Mat 58 models predicted the crushing response of the DEA components reasonably well. If, in addition to crushing, tensile properties along the 0°/90° fabric direction should become important, as could occur in combined loading cases, the Mat 58 model should be more accurate than the isotropic Mat 24 material model.

4.1.4 Simulation of the Multi-Terrain Impact Tests

LS-DYNA models were developed to simulate multi-terrain impacts of the composite fuselage section fitted with the DEA. Three different impact surfaces were evaluated: concrete, water, and soft soil (sand). Identical finite element models of the fuselage section and DEA were used in each simulation and only the impact medium was changed for the multi-terrain impact

simulations. Originally, the finite element model of the fuselage section was developed in the late 1990's using MSC.Dytran, which is an explicit transient dynamic simulation code similar to LS-DYNA. When the model was converted to LS-DYNA in 2003, there were no easy methods to simulate hybrid composite laminates that were composed of two different material systems, in this case graphite/epoxy and E-glass/epoxy fabrics. Consequently, some indirect methods were used to allow dissimilar material inputs. These methods are no longer needed and the model was updated using the *PART_COMPOSITE card in LS-DYNA.

General model information regarding details of the multi-terrain simulations can be found in Table 8. Note that a Kevlar®-129 fabric/epoxy sheet was placed beneath all DEA blocks to effectively transfer the impact loads into the cell walls.   The rigid impact surface was represented using shell elements, whereas the water and sand surfaces were represented using solid hexagonal elements. Shell elements in the fuselage section model represented the inner and outer face sheets of the upper fuselage cabin and the DEA components.   Solid elements represented the upper cabin foam core and the floor foam core. Beam elements in the model represented the seat tracks that were mounted to the floor of the fuselage and concentrated mass elements were used to represent the ten 100-lb lead masses attached to the seat tracks.

Table 8. Fuselage section with DEA model information.

Property	Rigid impact	Sand impact	Water impact
Number of nodes	126,500	220,305	202,472
Number of solid elements	14,946	99,618	87,846
Number of shell elements (total)	129,573	128,180	128,180
Number of shell elements (DEA)	116,160	117,792	117,792
Number of beam elements	188	188	188
Number of concentrated mass elements	40	40	40
Number of parts	12	13	14
Number of Linux-based processors	4	4	4
*MAT_24 run time, minutes	271	2366	2797
*MAT_58 run time, minutes	250	2153	2675

The model contained 7 different material models. The material properties of E-glass/epoxy and graphite/epoxy fabric materials that were used in the face sheets in the upper fuselage cabin were determined from coupon tests and are represented using a bilinear elastic-plastic material model with strain hardening. The 3- and 8-lb/ft^3 polyurethane foam cores were modeled as linear elastic materials. The laminate stacking sequences of the multi-layered face sheets were defined using *PART_COMPOSITE to specify the material designations of each ply, ply thicknesses and orientation, and the number of integration points per ply.   Shell elements used to represent the DEA blocks were assigned the same Mat 58 and Mat 24 material properties that were used previously to represent the DEA components. The DEA shell elements had a nominal element edge length of 0.5-in. Additional details regarding the fuselage section model can be found in References 34-38.

For the multi-terrain impacts, the selected calibration metrics were average floor-level accelerations over specified time durations and plots of acceleration time histories. The selection

of these metrics was guided by the stated design goal for the DEA, which was to limit average floor-level accelerations to 20-g or less. Finally, predicted acceleration results for the multi-terrain simulations were filtered using an SAE low-pass filter [39]. Test data for the rigid surface and sand impact tests are presented unfiltered, whereas the water impact data are filtered using and SAE low-pass filter [39]. The multi-terrain impact simulations will be described in the following subsections of the paper.

4.1.4.1 Results for the Rigid Surface Impact

The finite element model for simulating impact of the composite fuselage section with DEA onto concrete is shown in Figure 53. Nodes forming the concrete impact surface were fixed in the model. The four DEA blocks were attached to the fuselage model using the *TIED_SHELL_EDGE_TO_SURFACE option in LS-DYNA. A contact algorithm entitled *CONTACT_AUTOMATIC_SINGLE_SURFACE was used to define contact interfaces between the concrete surface and the DEA, in addition to modeling self-contact within element segments of the DEA. An impact velocity of 38.4-ft/s (460.8-in/s) was prescribed to the fuselage section with DEA blocks using the *INITIAL_VELOCITY_GENERATION card in LS-DYNA. A perfectly vertical orientation of the fuselage was assumed. Two models were executed, one in which the DEA blocks were assigned Mat 24 and the second with Mat 58. The simulations were executed with double precision using LS-DYNA version 971 for 0.1-seconds. Execution times are listed in Table 8.
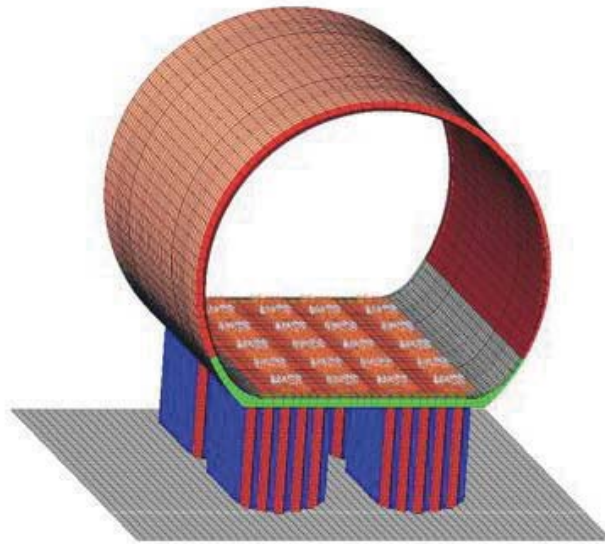
Figure 53. Finite element model of the composite fuselage section with DEA impacting concrete.

Acceleration time history comparisons, shown in Figure 54, are plotted for the left and right center, left front, and right rear lead blocks on the floor of the fuselage. Note that these floor positions are depicted in Figure 24(b). Unfiltered acceleration data is plotted with LS-DYNA results, which were filtered using an SAE Channel Filter Class (CFC) 60 low-pass filter [39]. As a method of judging the level of correlation, average accelerations were obtained for the experimental and analytical responses by calculating the area under the acceleration curves from 0.0- to 0.05-seconds, and then dividing the area by the pulse duration. The values of average acceleration are listed in the plot labels. In general, the model executed with Mat 58 under predicts the average accelerations of the test by approximately 1-g, while the Mat 24 model over

predicts the test by approximately 2-g. The Mat 24 responses show a large increase in acceleration at 0.05-s, as a result of the DEA reaching compaction. A similar increase is not seen in the test data or in the Mat 58 predicted responses. In general, the Mat 24 responses have shorter duration than either the test data or the Mat 58 responses. The Mat 24 material model predicted an average DEA crush of 13.7-in., while the Mat 58 model predicted the crush at 14.8-in. Experimental results indicated that the DEA blocks crushed between 14.2- to 14.9-in. based on double integration of measured floor-level acceleration responses.
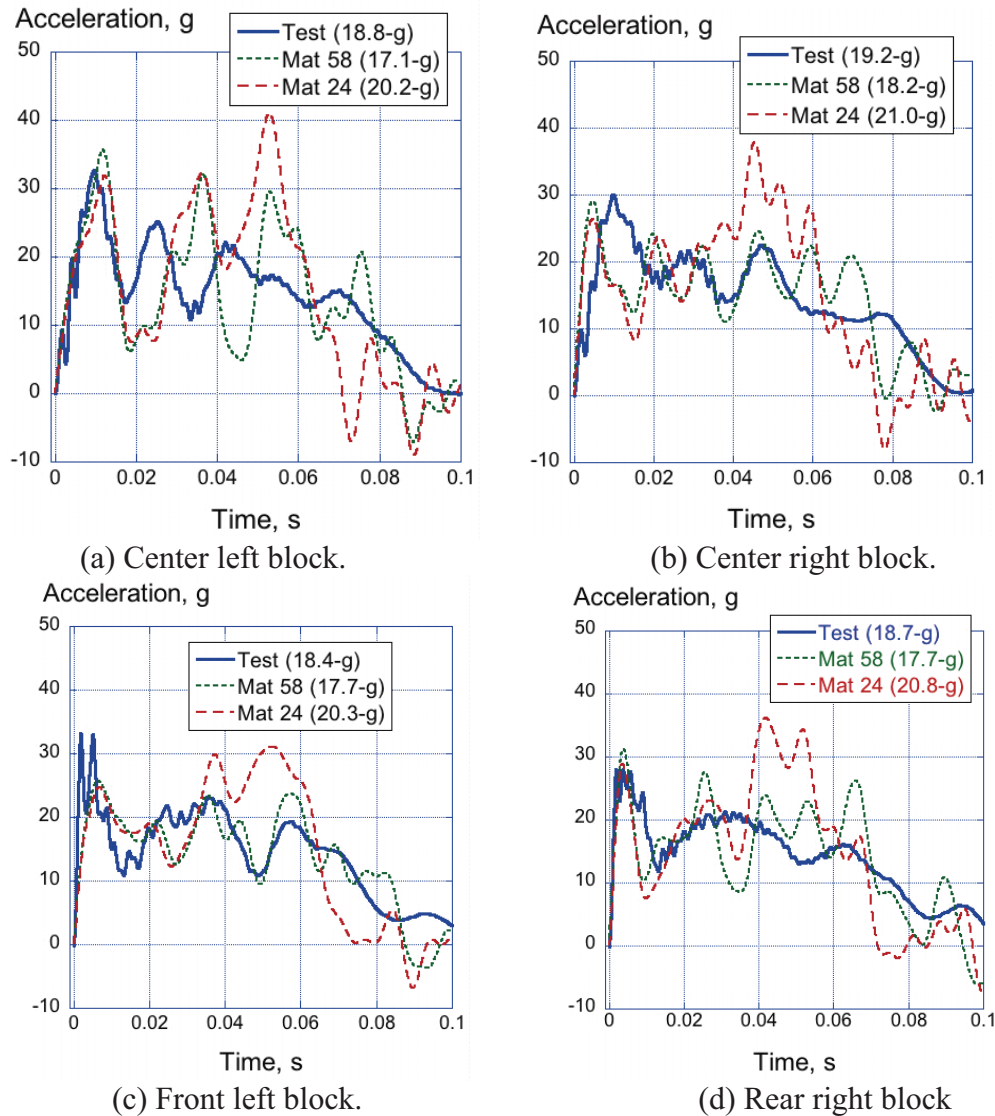
Figure 54. Test-analysis comparisons from different locations for the rigid surface impact.
Average accelerations were calculated based on a time interval of 0.0- to 0.05-seconds.

The average accelerations based on the test data ranged from 18.4- to 19.2-g, indicating a high level of consistency in the test data, with less than 1-g variability based on floor location. In addition, these results show that the design goal for the DEA (to limit floor level accelerations to 20-g) was achieved. The Mat 58 predicted average accelerations ranged from 17.1- to 18.2-g, or

generally 1-g lower than the test data. Conversely, the Mat 24 predicted average accelerations ranged from 20.2- to 21.0-g, or generally 2-g higher than the test data.

4.1.4.2 Results for Water Impact
The same fuselage section and DEA model that was used during the rigid surface impact simulation was also executed for water impact using the Arbitrary Lagrange-Euler (ALE) formulation in LS-DYNA. The physical model is shown in Figure 55. Again, two material models were assigned to the DEA, Mat 24 and Mat 58. The water (red mesh) and air (pink mesh) were modeled using 56,700 and 16,200 solid elements, respectively, to simulate the fluid-structure interaction problem. The air region above the water was added to accommodate the splash that occurs upon contact of the water surface with the DEA blocks located beneath the fuselage floor. The Kevlar® cover sheet was attached to the bottom surface of the DEA blocks using the *TIED_SHELL_EDGE_TO_SURFACE option in LS-DYNA. A perfectly flat attitude of the fuselage was also assumed, and an impact velocity of 27.4-ft/s (328.8-in/s) was prescribed to the fuselage section and DEA blocks. Single-point constraints were applied to the circumference of the water and air meshes in addition to the bottom of the water. The simulations were executed with double precision using LS-DYNA version 971 for 0.15-seconds.
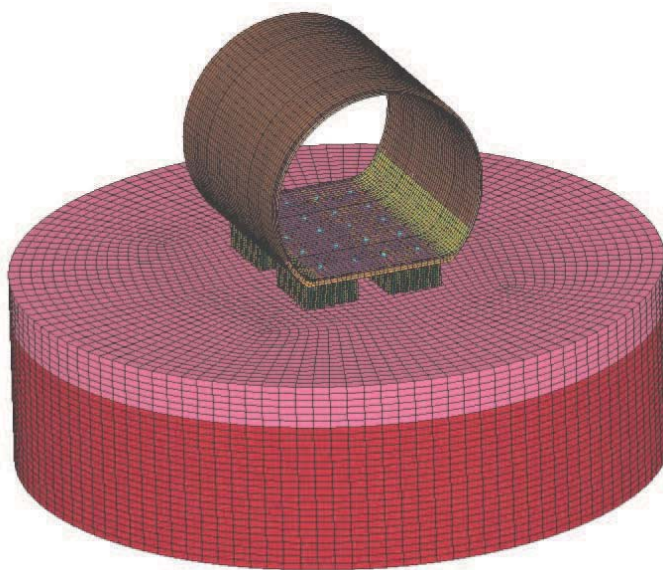
Figure 55. ALE model of the composite fuselage section with DEA impacting fluid (air/water).

As shown in Figure 56, the acceleration responses for both the Mat 24 and Mat 58 material models of the DEA, filtered with a SAE CFC 60 low-pass filter [39], show good qualitative correlation with test data, that was filtered using an SAE CFC 180 low-pass filter. In general, both models over predict the initial peak accelerations of the center lead blocks, but capture the higher initial peaks of the front and rear accelerometers. Neither model predicts the second large spike in acceleration seen in the center accelerometer locations that is attributed to impact of the bottom of the fuselage section with the water.

For water impact, the average accelerations based on the test data ranged from 6.6- to 9.2-g, indicating variability in the test data based on floor location. Even with the variability, these results show that the design goal for the DEA (to limit floor level accelerations to 20-g) was

achieved. The Mat 58 predicted average accelerations ranged from 12.4- to 12.8-g, and the Mat 24 predicted average accelerations ranged from 12.4- to 12.7-g. These ranges indicate a high degree of uniformity in the predicted floor responses that are not seen in the test data.

(a) Center left block.

(b) Center right block.

(c) Front left block.

(d) Rear right block.
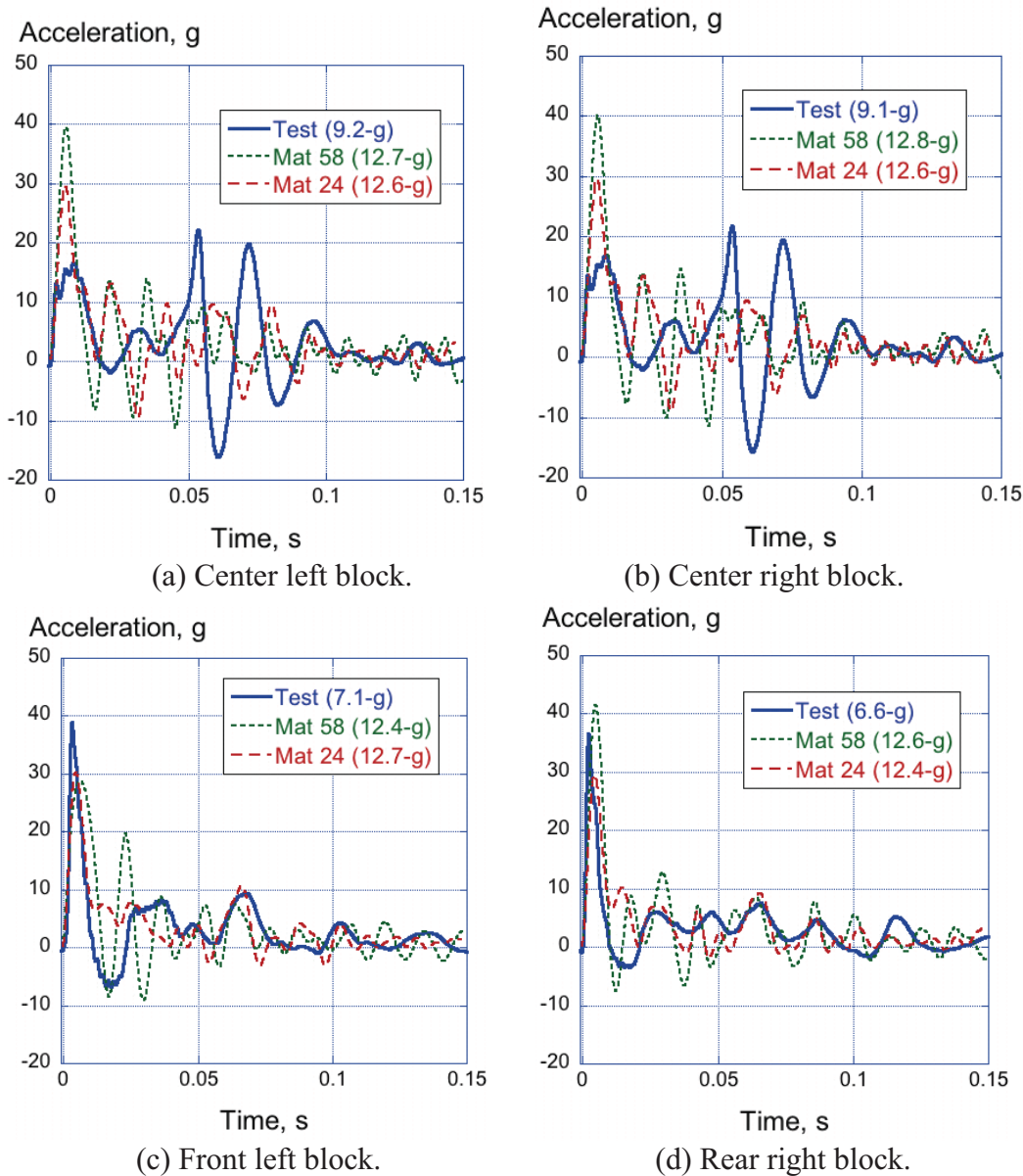
Figure 56. Acceleration time histories for water impact at locations on the fuselage floor. Average accelerations were calculated based on a time interval of 0.0- to 0.02-seconds.

4.1.4.3 Results for Soft Soil (Sand) Impact

The same fuselage section model with a shell-based representation of the DEA blocks that was used during the rigid surface and water impact simulations was also executed for soft-soil impact. The finite element model is shown in Figure 57. The sand was represented by an additional 84,672 solid elements that were assigned Mat 5, *MAT_SOIL_AND_FOAM, material property. Information on the characterization of the sand used in this model can be

50

found in Reference 38. Like the rigid impact model, the fuselage orientation for sand impact was assumed to be perfectly vertical. Tied contacts were prescribed between the Kevlar® sheet and the DEA components, and the bottom of the fuselage and the DEA components through the *TIED_SHELL_EDGE_TO_SURFACE card in LS-DYNA. An automatic contact algorithm was specified to define contact between the sand and the DEA and self-contact within each DEA block. An impact velocity of 37.4-ft/s (448.8-in/s) was prescribed to the fuselage section with the DEA components. The simulation was executed with double precision using LS-DYNA version 971 for 0.2-seconds.
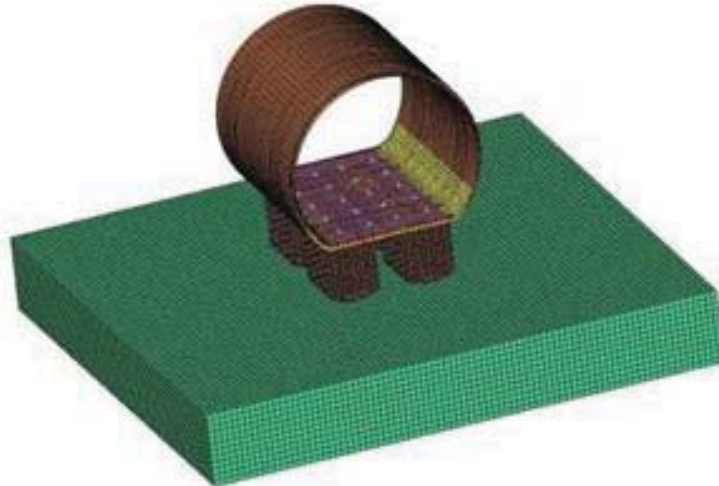
Figure 57. Composite fuselage section model with DEA components and sand.

In the simulation, the crater depths in the sand ranged between 9- and 10.5-in. for Mat 24 and between 9- and 11-in. for Mat 58, and the crush of each DEA component ranged between 5- and 8-in. for Mat 24 and 3.75- and 5-in. for Mat 58. In the test, between 7- and 9-in. of penetration into the sand was measured, and the amount of DEA crush was estimated to be 6- to 8-in. [5, 38]. Acceleration response comparisons of four different lead block locations on the floor of the fuselage are shown in Figure 58. Predicted acceleration results were filtered using an SAE CFC 60 low-pass filter [39], while test data is unfiltered. The plot labels list the average accelerations determined for a time interval of 0.0- to 0.05-seconds. The general analysis trends show good correlation with the test.

For the sand impact, the average accelerations based on the test data ranged from 16.9- to 17.8-g, indicating a high degree of consistency in the test data, with less than 1-g variation based on floor location. In addition, these results show that the design goal for the DEA (to limit floor level accelerations to 20-g) was achieved. The Mat 58 predicted average accelerations ranged from 17.8- to 23-g, and the Mat 24 predicted average accelerations ranged from 17.8- to 21.2-g. Both material models over predict the measured acceleration responses by as much as 5-g. In addition, these acceleration ranges indicate a higher degree of variability in the predicted floor responses than observed in the test data.

Acceleration, g

(a) Center left block.

Test (17.7-g)
Mat 58 (21.9-g)
Mat 24 (19.6-g)

(b) Center right block.

Test (17.4-g)
Mat 58 (20.9-g)
Mat 24 (19.5-g)

(c) Front left block.

Test (17.8-g)
Mat 58 (23.0-g)
Mat 24 (21.2-g)

(d) Rear right block.

Test (16.9-g)
Mat 58 (17.8-g)
Mat 24 (17.8-g)
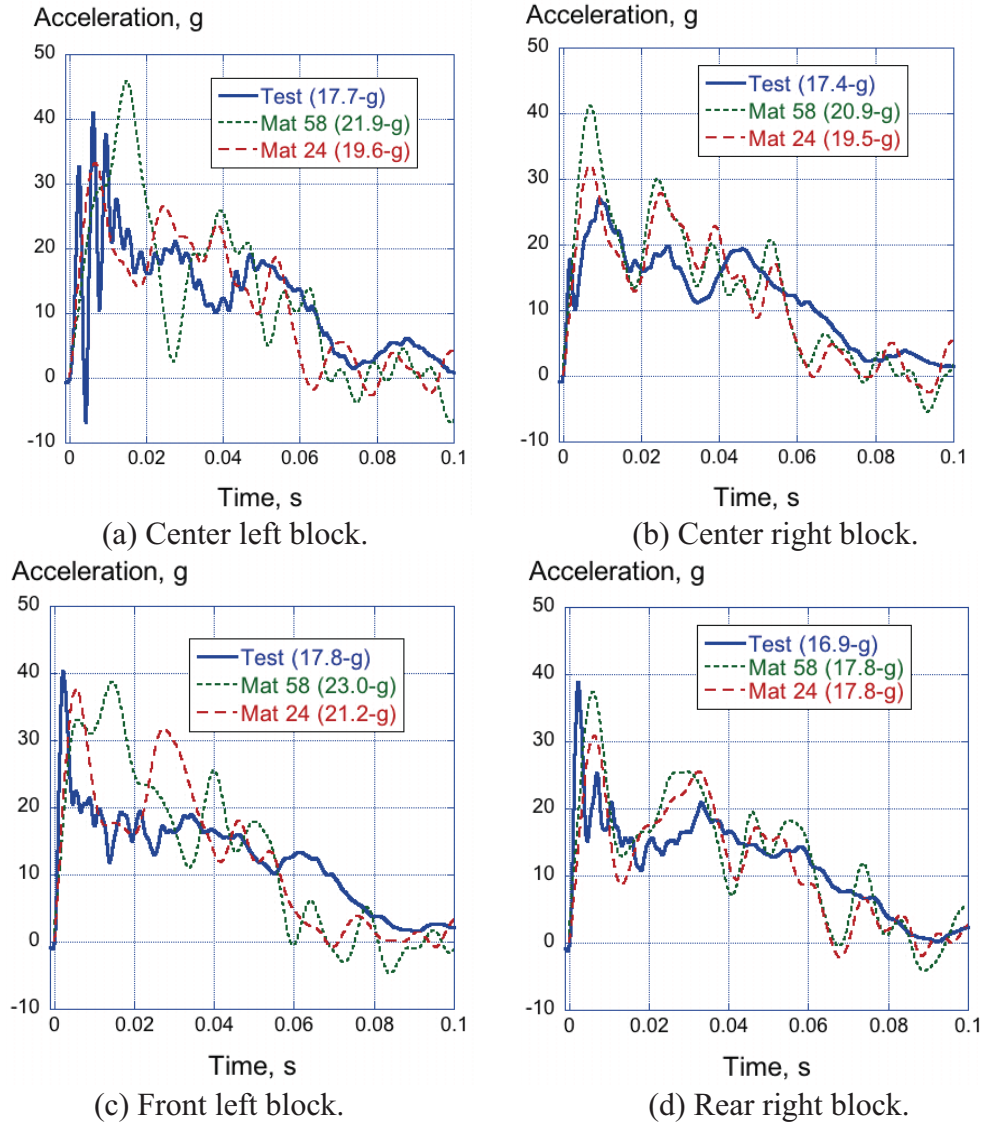
Figure 58. Test-analysis correlation from different locations on the fuselage floor during sand impact. Average accelerations were calculated using a time interval of 0.0- to 0.05-seconds.

4.1.4.4 Discussion of Multi-Terrain Simulation Results

Both the Mat 24 and the Mat 58 material models performed well in predicting floor-level acceleration responses of the vertical drop tests onto multi-terrain. The Mat 58 model showed slightly better comparison with test data for the rigid surface impact, while the Mat 24 model compared better with the sand test. Since the DEA blocks experience very little crushing during water impact, the two material models provided nearly equivalent results for this impact surface. It is anticipated that both models would provide similar results, except for cases involving combined loading where the orthotropic material behavior of the fabric becomes important.

4.2 Solid-Element Modeling of the DEA

Solid-element-based finite element models of the dynamic crush tests of the DEA components were developed for execution in LS-DYNA version 971. Initially, solid elements were selected

for the simulations as a means of lowering execution times, compared with shell-element-based simulations. However, it was understood that the use of solid-element-based models precluded the accurate prediction of deformation modes observed in the actual DEA specimens, which would require detailed shell-element-based models. The major challenges of this simulation study were to define a material model that would enable accurate prediction of the dynamic crushing response of the normal (cells aligned with the loading direction) and off-axis (cells canted with respect to the loading direction) DEA components and to predict both the uniform crush and compaction responses of the DEA components. Two different material property definitions available in LS-DYNA were assigned to the solid elements, including Mat 63 (*MAT_CRUSHABLE_FOAM), and Mat 26 (*MAT_HONEYCOMB). Solid-element-based models of the three DEA components were developed and executed using both material definitions. In addition, the fuselage section model, previously described in Section 4.1.4, was updated with solid element representations of the DEA blocks and the multi-terrain impact simulations were executed in which both material models were assigned to the energy absorbers.

4.2.1 Material Model Development

The material property definitions in LS-DYNA that were selected to represent the DEA were *MAT_CRUSHABLE_FOAM (Mat 63) and *MAT_HONEYCOMB (Mat 26) [21]. A description of each material model is provided in the following subsections.

4.2.1.1 Mat 63 Crushable Foam Material Model
This material model is intended to represent the properties of isotropic crushable foam and includes optional damping and a tensile cutoff stress. Unloading is fully elastic to the tension cutoff stress and reloading follows the loading curve. Tension is represented using an elastic-perfectly-plastic response at the tension cutoff value [21]. Mat 63 allows input of a user-defined curve representing the yield stress versus volumetric strain of the material. It is important to note that volumetric strain is defined as 1 minus the relative volume, which is the ratio of the current volume to the initial volume. Thus, as crushing initiates, the volumetric strain is low and increases as crushing progresses. The input values used in the Mat 63 material model are listed in Table 9.

Table 9. Mat 63 input parameters.

Parameter	Description	Value
RO	Material density	2.182e-6 lb-s^2/in^4
E	Young's modulus	600 psi
PR	Poisson's ratio	0.05
LCID	Identification number of user input stress-strain response	8
TSC	Tensile stress cutoff	-5 psi
DAMP	Damping coefficient	0.05

Input load curves (LCIDs) representing the stress versus volumetric strain responses of the 59- and 104-cell DEA were calculated from the filtered acceleration data obtained from the respective component tests. The stress was determined by adding 1 to the filtered acceleration data in g's (to account for gravitational loading), then multiplying the sum by the weight of the

impact block, and then dividing by the cross-sectional area of the DEA. The strain was calculated by double integration of the raw acceleration response to obtain displacement, which was then divided by the initial height of the DEA component. Note that this strain calculation represents the change in height of the DEA specimen, which is only one component of the volumetric strain. However, given a low value of Poisson's ratio (PR=0.05), this approach provides a reasonable approximation of the volumetric strain.

The raw stress-strain data for the 59- and 104-cell DEA components are plotted in Figures 59(a) and (b), respectively, along with the corresponding Mat 63 input curves. Since the 104-cell DEA did not reach the compaction phase during the test, the Mat 63 curve was approximated to have the same response as the 59-cell DEA after a strain of approximately 0.8-in/in. For this simulation study, the two Mat 63 curves based on the 59- and 104-cell DEA test data were input as user-defined load curves (LCIDs) in the DEA models. Finally, it should be noted that the unloading curve for this material definition is elastic; however, the experimental responses of the 59- and 104-cell DEA components, shown in Figure 59, indicate that the actual unloading curves are hysteretic.

(a) Mat 63 input curve for 59-cell DEA.   (b) Mat 63 input curve for 104-cell DEA.
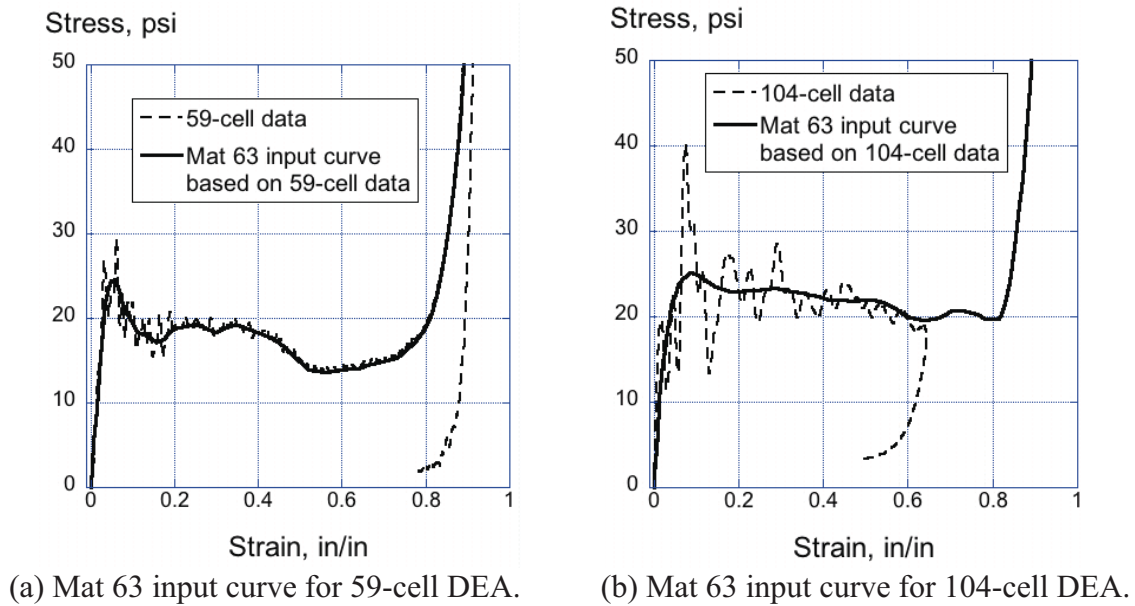
Figure 59. Mat 63 input load curves derived from the 59- and 104-cell DEA test data.

4.2.1.2 Mat 26 Honeycomb Material Model
The Mat 26 material model is used to represent honeycomb and foam materials with anisotropic behavior [21]. Nonlinear elastic-plastic material responses are defined separately for normal and shear stresses and these input curves are considered to be fully uncoupled. The behavior of the material before compaction is orthotropic, where the components in the stress tensor are uncoupled. Unloading is based on the interpolated Young's modulus, which must provide an unloading tangent that exceeds the loading tangent. The input values used in the Mat 26 material model for both the normal and off-axis DEA components are listed in Table 10. One difference between Mat 63 and Mat 26 is that Young's modulus (E) has been increased from 600-psi for Mat 63 to 6,000-psi for Mat 26. The actual Young's modulus as measured from test data is 600-psi. However, when this value is used in Mat 26, negative volume errors occurred in the

simulation, indicating that some elements have inverted due to the low value of stiffness. Consequently, the value of Young's modulus used in Mat 26 was artificially increased to avoid this problem.

Table 10. Mat 26 input parameters.

| Symbol	Description	Value	
		Normal DEA	**Off-axis DEA**
RO	Material density, lb-s^2/in^4	2.182e-6	2.182e-6
E	Young's modulus of fully compacted honeycomb, psi	6000	6000
PR	Poisson's ratio	0.05	0.05
SIGY	Yield stress of fully compacted honeycomb, psi	22.0	22.0
VF	Relative volume at which honeycomb is fully compacted	0.135	0.135
MU	Damping coefficient	0.065	0.065
BULK	Bulk viscosity flag, if equal 0.0, bulk viscosity is not used	0.0	0.0
LCA	Load curve id for stress sigma-aa versus volumetric strain	SF*=0.1	SF*=0.1
LCB	Load curve id for stress sigma-bb versus volumetric strain	SF=0.1	SF=0.1
LCC	Load curve id for stress sigma-cc versus volumetric strain	SF=1.0	SF=1.0
LCS	Load curve id for shear stress versus volumetric strain	No input	No input
LCAB	Load curve id for stress sigma-ab versus volumetric strain	SF=0.45	SF=0.45
LCBC	Load curve id for stress sigma-bc versus volumetric strain	SF=0.45	SF=0.45
LCCA	Load curve id for stress sigma-ca versus volumetric strain	SF=0.45	SF=0.45
LCSR	Load curve id for strain rate effects (optional)	No input	No input
EAAU	Elastic modulus Eaau in uncompressed configuration, psi	60.0	60.0
EBBU	Elastic modulus Ebbu in uncompressed configuration, psi	60.0	60.0
ECCU	Elastic modulus Eccu in uncompressed configuration, psi	566.7	566.7
GABU	Shear modulus Gabu in uncompressed configuration, psi	135.0	135
GBCU	Shear modulus Gbcu in uncompressed configuration, psi	270.0	270.0
GCAU	Shear modulus Gcau in uncompressed configuration, psi	270.0	270.0
AOPT	Material axes option (equal 2.0 – globally orthotropic material axes determined by vectors **a** and **d**)	2.0	2.0
MACF	Material axis change flag (default=1, no change)	1.0	1.0
XP YP ZP	Coordinates of point p for AOPT = 1	No input	No input
A1 A2 A3	Coordinates of vector **a** for AOPT = 2	1, 0, 0	0, -.454, .891
D1 D2 D3	Coordinates of vector **d** for AOPT = 2	0, 1, 0	1, 0, 0
TSEF	Tensile strain at element failure (element will erode)	No input	No input
SSEF	Shear strain at element failure (element will erode)	No input	No input

*SF is a Scale Factor applied to the primary input load curve (LCC)

In this study, the input stress-strain curves are based on volumetric strain. The user of this material model is cautioned in Reference 21 to ensure that each input curve contains the exact same number of points and this recommendation was followed. The input load curves for Mat 26 were, once again, based on the stress-strain responses of the 59- and 104-cell DEA components, as shown in Figures 60(a) and (b), respectively. Unlike the input curves for Mat 63 which begin at zero stress and zero strain, each of the two Mat 26 input curves begins with a point having negative strain and positive stress and the second point has a corresponding value of positive strain and the same value of positive stress. This approach for inputting the load curves for Mat 26 is recommended in Reference 21.
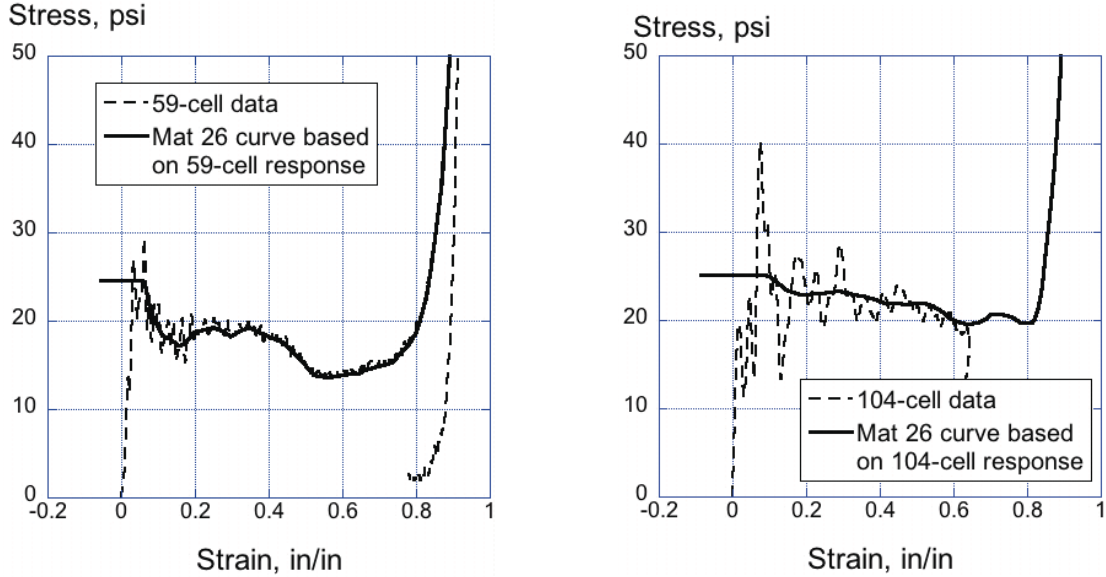
(a) Mat 26 input curve for 59-cell DEA. (b) Mat 26 input curve for 104-cell DEA.

Figure 60. Mat 26 input curves for the 59- and 104-cell DEA components.

The Mat 26 input curves, shown in Figure 60, correspond to the load curve for sigma-cc (LCC listed in Table 10) versus volumetric strain, where cc represents the local vertical direction. Since no experimental data were available, load curve inputs for the two primary transverse directions (aa and bb) and for the shear directions (s, ab, bc, ca) were based on engineering judgment. The load curves in these directions were assumed to be scaled versions of sigma-cc (LCC), with the scale factors listed in Table 10. Finally, Mat 26 allows the user to define directions for the local material axis system using the AOPT parameter [21]. For these simulations, AOPT was set to 2.0 indicating globally orthotropic behavior with material axes determined by vectors **a** and **d**, such that **a** x **d** defines the primary material direction. For the 59- and 104-cell DEA components, the vectors were chosen such that the primary material direction (cc) is oriented vertically, as illustrated in Figure 61(a). For the 68-cell DEA, the vectors were defined such that the primary material axis for LCC was canted 27° with respect to the vertical direction, as illustrated in Figure 61(b).
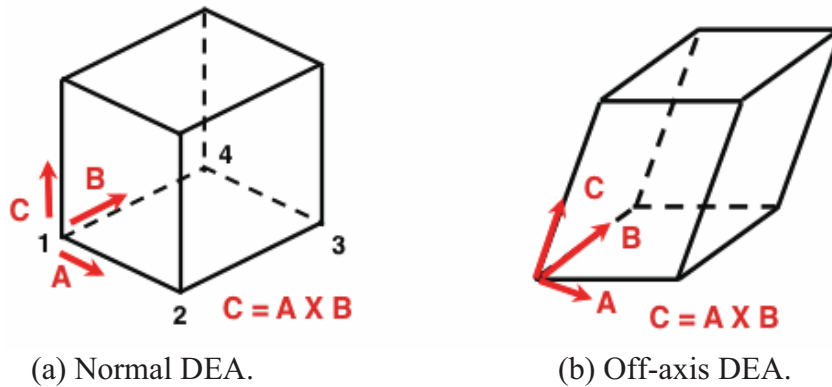
(a) Normal DEA.   (b) Off-axis DEA.

Figure 61. Schematic drawings illustrating local material axis definitions for normal and off-axis DEA components.

4.2.2 Simulation of the DEA Multi-Cell Component Tests

The 59-, 104-, and 68-cell DEA component models are shown in Figure 62. Each model consists of three main parts: the DEA, which is represented using hexagonal solid elements with element formation 1 (default constant stress solid element); an impact surface, located just beneath the bottom surface of the DEA, that is constructed of quadrilateral shell elements; and, a rigid block that is constructed of solid hexagonal elements that are assigned a *MAT_RIGID material property. Each DEA model had a nominal element edge length of 0.5-in., which was determined based on a prior mesh discretization study. The impact surface was included to prevent element deformation below the bottom surface of the DEA, which was especially needed for the 68-cell DEA. All edge nodes on the impact surface were fully constrained. The same *MAT_RIGID material property used for the impact block was assigned to the impact surface. The density of the rigid material was chosen such that the weight of each rigid block matched the test conditions, which are listed in Table 1. Likewise, nodal velocities were assigned to the block to match the test conditions. For all models, a segment-based contact definition of *CONTACT_AUTOMATIC_SINGLE_SURFACE was used with a coefficient of friction of 0.35. This contact definition essentially prohibits any node from penetrating any surface and is used to represent contact between the impact block and the DEA, the DEA and the impact surface, and self-contact between elements within the DEA. Finally, the DEA component simulations were executed to include gravity as a body load.

| (a) 59-cell model. | (b) 104-cell model. | (c) 68-cell model. |
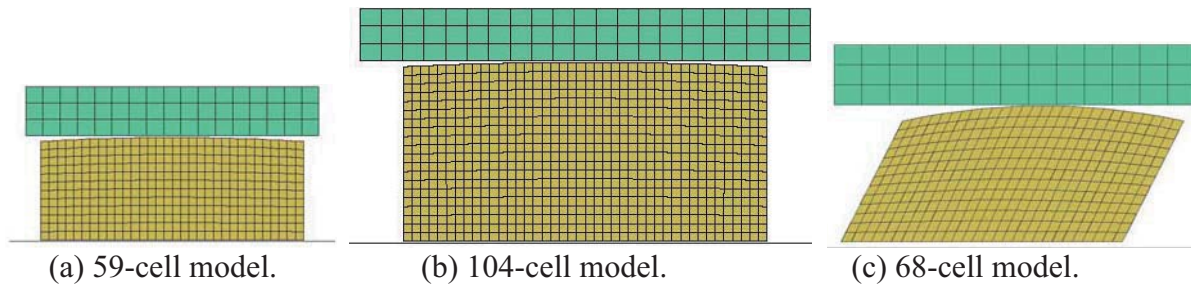
Figure 62. Solid element models of three DEA components.

Single Point Constraints (SPCs) were assigned to the bottom nodes of each solid element DEA model to represent fixed boundary conditions used in the test. For the 59- and 104-cell DEA components, the fully deployed DEA was held in place using double sticky back tape on the impact surface of the drop tower. For the 68-cell DEA component, the bottom of the fully deployed DEA was attached to a plate using potting material. To represent these conditions, variations in the SPCs were studied and the best results were found using fixed constraints in translation and rotation. Consequently, the results shown in this paper are for these conditions. Nodal constraints were input using the *BOUNDARY_SPC_SET card in LS-DYNA.

Two different material models, Mat 63 and Mat 26 were evaluated. For the 59-cell DEA, input curves to Mat 63 and Mat 26 were based on the 59-cell DEA stress-strain responses, plotted in Figures 59(a) and 60(a), respectively. Likewise, for the 104-cell DEA, input curves were based on the 104-cell DEA stress-strain responses, plotted in Figures 59(b) and 60(b). Both material models, along with both sets of input curves, were evaluated for the 68-cell DEA to determine which material model best predicted the actual response.

Specific details of the three DEA component models are listed in Table 11. Comparisons of the simulation predictions with the test data are made for each DEA component to evaluate the effectiveness of the two material models in predicting the DEA response. In each case, raw experimental data are plotted with predicted responses that were filtered using an SAE CFC 180-Hz low-pass filter [39]. In addition, four correlation metrics were selected to assess the level of agreement between test and analysis for the DEA components. These metrics are initial peak acceleration, average acceleration for a time interval of 0.0-0.03 seconds, average crush stress based on average acceleration, and peak acceleration during compaction.

Table 11. Details of the solid-element models of the DEA components.

Property	59-Cell	104-Cell	68-Cell
Number of nodes	13,354	31,330	15,370
Number of solid elements	10,892	27,776	12,928
Number of shell elements	361	225	160
Number of parts	3	3	3

4.2.2.1 Results for the 59-cell DEA Component Test

Test-analysis comparisons for the 59-cell DEA component are shown in Figures 63(a) and (b) for two different material models, Mat 63 and Mat 26, respectively. For both material models, the input stress-strain curves were based on the 59-cell DEA response. The correlation metrics for each simulation are listed in Table 12. The results indicate that both material models are able to predict the average acceleration and crushing stress within ±3%. However, results for initial and peak compaction accelerations are not as good. The Mat 63 predicted response indicates an increase of acceleration near the end of the pulse, representing compaction of the DEA. However, the magnitude of the compaction response is under predicted (49.3-g for the simulation versus 64.4-g for the test). The timing of the Mat 63 compaction peak occurs approximately 0.002-s later in time than the test peak. As shown in Figure 63(b), the model executed using Mat 26 over predicted the peak acceleration seen during compaction of the DEA (73.8-g for the simulation versus 64.4-g for the test). However, the timing of the compaction peak closely matched the test.
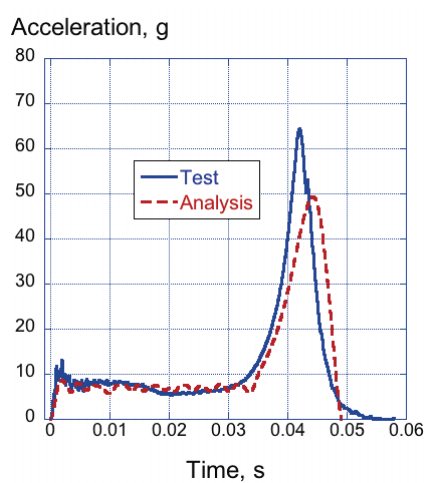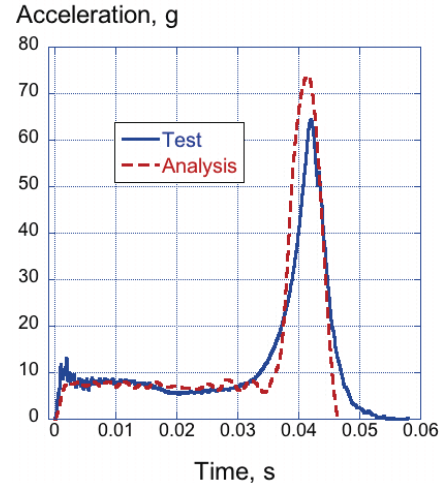
(a) Model executed using Mat 63. (b) Model executed using Mat 26.

Figure 63. Test-analysis comparisons for the 59-cell DEA component.
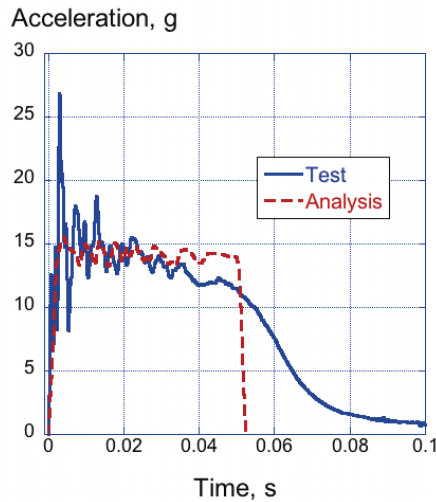
58

Table 12. Test-analysis correlation metrics for the 59-cell DEA component

Parameter	Test	Model (Mat 63)		Model (Mat 26	
		Value	Percentage Difference	Value	Percentage Difference
Initial peak acceleration, g	12.4	8.7	29.8	8.0	35.5
*Average acceleration, g	7.1	6.9	2.8	7.1	0.0
Average crush stress, psi	16.9	16.5	2.4	16.9	0.0
Compaction peak, g	64.4	49.3	23.5	73.8	-14.6

*Average acceleration calculated for a time interval of 0.0-0.03 seconds.

4.2.2.2 Results for the 104-cell DEA Component Test

Test-analysis comparisons for the 104-cell DEA component are shown in Figures 64(a) and (b) for two different material models, Mat 63 and Mat 26, respectively, and correlation metrics are listed in Table 13. Note that no data are shown in Table 13 for peak compaction acceleration, since the experimental and analytical responses did not exhibit this behavior. The results indicate that both material models are able to predict the uniform crushing response of the test within ±4%. No significant trends are observed in the correlation metrics to indicate significant differences based on material model. However, one major difference between the simulation responses and the test data is that both of the analytical curves exhibit a sudden drop in the acceleration response at approximately .05-seconds, whereas the experimental response shows a more gradual reduction in acceleration.

(a) Model executed using Mat 63.   (b) Model executed using Mat 26.

Figure 64. Test-analysis correlation results for the 104-cell DEA component.

Table 13. Test-analysis correlation metrics for the 104-cell DEA component

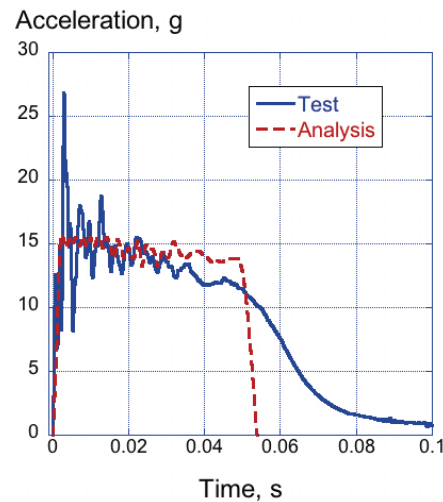| Parameter	Test	Model (Mat 63)		Model (Mat 26	
		Value	%Difference	Value	%Difference
Initial peak accel., g	26.8	15.5	42.2	15.7	41.4
*Average acceleration, g	14.3	13.8	3.5	14.2	0.7
Average crush stress, psi	22.1	21.3	3.6	21.9	0.9

*Average acceleration calculated for a time interval of 0.0-0.03 seconds.

<u>4.2.2.3 Results for the 68-cell Off-Axis DEA Component Test</u>
Test-analysis comparisons for the 68-cell DEA component are shown in Figures 65(a) and (b) for two different material models, Mat 63 and Mat 26, respectively, and correlation metrics are listed in Table 14. Both input curves based on the 59- and 104-cell stress-strain curves were evaluated in Mat 63 and Mat 26, and the predicted responses were compared with test data.

(a) Model executed using Mat 63.   (b) Model executed using Mat 26.

Figure 65. Test-analysis correlation results for the 68-cell DEA component.

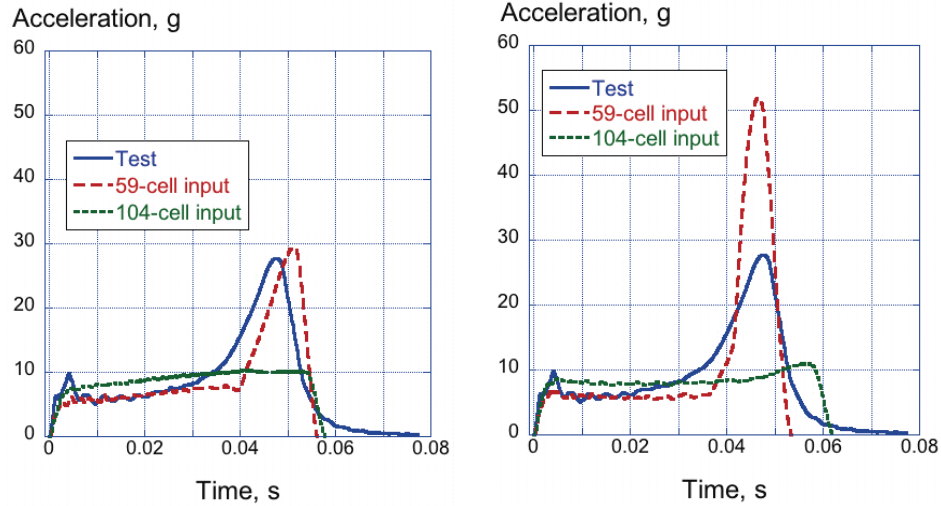Table 14. Test-Analysis Correlation Metrics for the 68-Cell DEA Component
Input Load Curve Based on the 59-cell Test Data

Parameter	Test	Mat 63 59-Cell Input		Mat 63 104-Cell Input		Mat 26 59-cell Input		Mat 26 104-Cell Input	
		Value	%Error	Value	%Error	Value	%Error	Value	%Error
Initial peak acceleration, g	9.9	6.2	37.4	7.4	25.3	7.1	28.2	8.7	12.1
*Average acceleration, g	6.5	6.0	7.7	8.0	-23.1	5.7	12.3	7.7	-18.5
Average crush stress, psi	16.0	14.9	6.9	19.2	-20.0	14.3	10.6	18.5	-15.6
Compaction peak, g	27.7	29.4	-6.1	10.3	62.8	51.8	-87.0	11.0	60.3

*Average acceleration calculated for a pulse duration of 0.0-0.03 seconds.

Test-analysis results, shown in Figure 65, indicate that both material models, Mat 63 and Mat 26, are generally capable of predicting the complex response of the 68-cell DEA when the 59-cell DEA stress-strain response is used as input. Neither model captures the initial 10-g peak or the subsequent 5-g reduction in acceleration, which is attributed to buckling of perimeter cells in the component. Instead, the predicted responses show a gradual increase in acceleration from initial peaks ranging from 6.2- to 7.1-g until compaction. The correlation metrics listed in Table 14 indicate that both material models are capable of predicting the average acceleration and crush stress within ±13%, when the 59-cell stress-strain response in used. Also, both the Mat 63 and

Mat 26 models predict compaction of the DEA when the 59-cell stress-strain responses are input. The Mat 63 model predicts a peak compaction acceleration of 29.4-g, compared with 27.7-g for the test. The Mat 26 model over predicts the peak compaction acceleration (51.8-g for the simulation compared with 27.7-g for the test). However, the Mat 26 model demonstrates better prediction of the timing of the compaction peak than does Mat 63. In general, the material models that were executed using the 104-cell stress-strain input responses over predict the average acceleration and either demonstrate no compaction (Mat 63) or only a minor compaction response (Mat 26).

4.2.2.4 Discussion of Material Model and DEA Component Simulation Results
Two material models, Material Type 63 (*MAT_CRUSHABLE_FOAM) and Material Type 26 (*MAT_HONEYCOMB), were selected for evaluation in the solid-element-based models of the DEA components. As documented in Reference 21, LS-DYNA offers many additional material models that would be appropriate for representing the behavior of the DEA including Mat 83 (*MAT_FU_CHANG_FOAM), Mat 126 (*MAT_MODIFIED_HONEYCOMB), and Mat 142 (*MAT_TRANSVERSELY_ANISOTROPIC_CRUSHABLE_FOAM). Generally, these models were developed to represent the crushing response of isotropic, orthotropic, and anisotropic foams including hysteretic unloading and strain rate effects. Mat 63 was selected for the present study because it is the simplest, most straightforward material model and has demonstrated good performance in past simulations, even under severe element deformations. Mat 26 was selected over Mat 126 based on prior research documented in Reference 41 in which models executed with Mat 126 developed problems with contact penetration, severe element distortion, and high values of hourglass energy in comparison with the total energy of the simulation. Mat 142 is a relatively new material model that was added to LS-DYNA for modeling an extruded foam material that is transversely isotropic, crushable, and of low density with no significant Poisson's effect. This material was used successfully, as an alternative to Mat 26 and Mat 126, to represent the off-axis crushing response of anisotropic foam, as documented in Reference 63. Future work may include evaluation of additional material models in LS-DYNA in predicting the DEA response.

During the development of the Mat 26 material model, two parameters, VF (the relative volume at which the honeycomb is fully compacted) and MU (the damping coefficient), were found to control the compaction response of the simulation. Parameter studies were conducted in which VF and MU were varied independently using the 68-cell DEA model with 59-cell stress-strain input curves, with results shown in Figures 66(a) and (b), respectively. For the plot of Figure 66(a), VF was varied independently with values ranging from 0.1 to 0.15 in increments of 0.01, while MU was held constant at 0.065. Based on this plot, the selection of VF strongly determines the shape and magnitude of the acceleration response during compaction, as well as timing of the peak acceleration. Likewise, a separate parameter study was performed in which MU was varied independently with values of 0.05, 0.1, and 0.15, while VF was held constant at 0.135. The results indicate that changes in MU also influence the magnitude of the peak acceleration during compaction, with MU=0.05 providing the highest magnitude response. Based on the parametric studies, the values of VF (0.135) and MU (0.065) were selected to provide correlation with the 59-cell DEA response using Mat 26, as listed in Table 10.

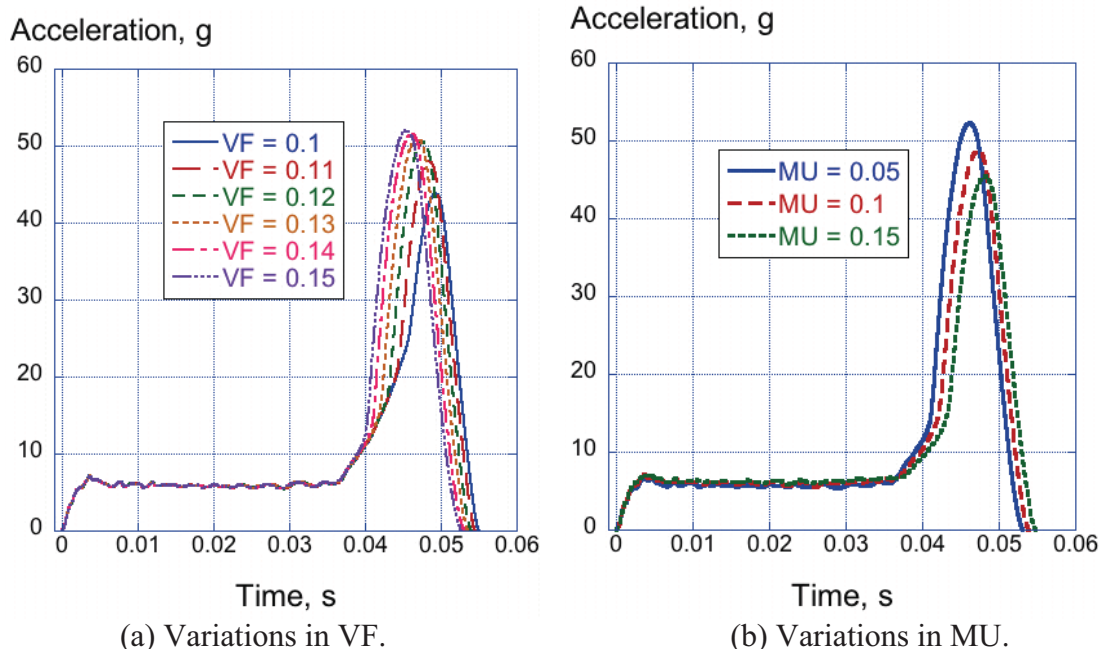| (a) Variations in VF. | (b) Variations in MU. |

Figure 66. Influence of variations in VF and MU on the 68-cell DEA predicted response.

One reason for evaluating solid-element-based models of the DEA was to demonstrate improved run times as compared with the shell-element-based models. All solid element DEA simulations were executed in double precision using LS-DYNA version 971 Shared Memory Processor (SMP) on a single Linux processor with a prescribed termination time of 0.1-seconds. Table 15 lists the run times for each simulation, which are comparable to the run times for the shell element simulations of the DEA components, listed in Table 4. However, a true comparison of run times is not feasible given that each solid element model contained considerably fewer elements than did their shell element counterparts. Also, solid elements were larger in size with a nominal element edge length of 0.5-in. compared with 0.25-in. for the shell elements. Finally, shell-element simulations were executed for 0.06-s, compared with 0.1-s for the solid element models.

Table 15. Run times for solid-element DEA simulations.

Parameter	59-cell DEA		104-cell DEA		68-cell DEA w/59-cell input		68-cell DEA w/104-cell input	
	Mat 63	Mat 26	Mat 63	Mat 26	Mat 63	Mat 26	Mat 63	Mat 26
Run time required, minutes	25	31	72	63	33	39	30	36

In general, the results of the solid element simulations of the DEA components indicate that both material models, Mat 63 and Mat 26, are capable of predicting the uniform crushing response of the DEA. In addition, both models were able to predict compaction of the DEA when input load curves were based on the 59-cell DEA response. In comparison, poor correlation was seen when the 104-cell stress-strain responses were input to Mat 63 and Mat 26 to predict the behavior of the 68-cell off-axis DEA, as shown in Figure 65. The 104-cell DEA component has a 20% higher average crush stress than the 59-cell DEA component (22.0-psi for the 104-cell DEA

62

versus 17.6-psi for the 59-cell DEA, based on the data shown in Figure 21). Consequently, for two identical impact simulations in which the compressive response of one energy absorber is based on the 104-cell DEA response and the second is based on the 59-cell DEA response, a greater amount of the incident kinetic energy is converted to internal (strain) energy for an equivalent amount of crush stroke for the energy absorber whose response is defined by the 104-cell DEA, leaving less energy for additional stroke or compaction.   Both material models (Mat 63 and Mat 26) and input curves (59- and 104-cell DEA responses) will continue to be evaluated in subsequent solid-element simulations of the DEA for multi-terrain impact.

Finally, it is important to note that the use of stress-strain responses, which were determined from acceleration time histories of the 59- and 104-cell DEA components, to define the material behavior of the DEA in Mat 63 and Mat 26 is not the ideal approach. The fact that the two DEA components exhibited significantly different responses indicates that the derived stress-strain curves do not represent a "material" behavior. Likely, these curves, shown in Figures 59 and 60, also contain geometric effects based on upper surface curvature and collapse of circumferential cells. Unfortunately, no quasi-static crush test data were available to establish an effective material response of the DEA in compression. It is also important to note that repeated tests of multiple DEA components of similar configuration were not conducted. An average crush stress of 19.8-psi was estimated by averaging the individual crush stress values obtained for the two normal DEA components (22.0-psi for the 104-cell component and 17.6-psi for the 59-cell component, based on the data shown in Figure 21).

4.2.3 Simulation of the Multi-Terrain Impact Tests

Modifications were made to the fuselage section model, shown in Figure 53, by removing the shell-element-based representation of the DEA blocks and adding solid hexagonal elements in their place. This change significantly reduced the number of shell elements in the model and increased the number of solid elements. The same fuselage section model was used for each multi-terrain impact simulation, and this model contained: 51,860 nodes; 13,413 Belytschko-Tsay shell elements; 40,000 hexagonal solid elements of which 28,128 elements represent the DEA blocks; 188 beam elements; 40 element masses; 12 parts; and, 7 material property definitions. For each multi-terrain simulation, physical representations of the impact media were added, as described in the following subsections. For the rigid surface and sand impact tests, comparisons of unfiltered acceleration data are made with predicted responses that were filtered using an SAE low-pass filter [39]. For the water impact case, both test data and predicted responses were filtered. Average acceleration was selected as the correlation metric for these simulations.

4.2.3.1 Results for the Rigid Surface Impact
A picture of the rigid surface impact simulation model is shown in Figure 67.   With the exception that solid elements were used to represent the DEA blocks, the fuselage section model is otherwise the same as the previous model described in Section 4.1.4.   An impact surface consisting of an additional 3,025 quadrilateral shell elements was added to the model and it was assigned a *MAT_RIGID material property. All nodes used in forming the impact surface were fixed using SPCs. Finally, a *CONTACT_AUTOMATIC_SINGLE_SURFACE was designated for the simulation with a coefficient of friction of 0.1.

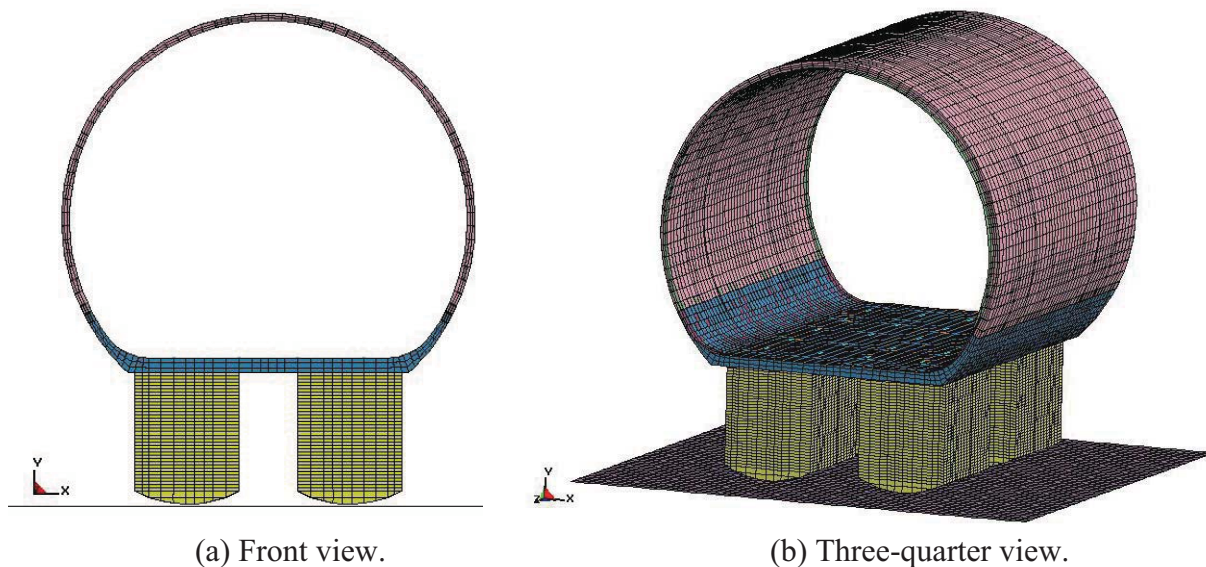(a) Front view.   (b) Three-quarter view.

Figure 67. Composite fuselage section model with curved bottom surface of the DEA.

As seen in Figure 67, the DEA blocks were configured to incorporate the 18-in. radius of curvature of the bottom surface. Both Mat 63 and Mat 26 material models were assigned to the DEA bocks with input stress-strain curves based on the dynamic crush responses of the 59- and 104-cell DEA components, as shown in Figures 59 and 60, respectively. The models were executed using LS-DYNA version 971, SMP, on a single Linux-based processor. Given a termination time of 0.15-seconds, the model with Mat 63 required 480 minutes and the model with Mat 26 required 540 minutes of clock time to achieve normal completion. These simulation times are considerably lower than those of the comparable shell-element based models, which are listed in Table 8.

Test-analysis results are shown in Figures 68-71 for the left and right center accelerometers, the front left accelerometer, and the right rear accelerometer, respectively. These floor-level accelerometer locations are shown in Figure 24(b). As a method of judging the level of correlation, average accelerations were obtained for the experimental and analytical responses by calculating the area under the acceleration curves from 0.0- to 0.05-seconds, and then dividing the area by the time interval (0.05-seconds). The 0.05-second pulse duration was selected as the minimum value based on all of the simulation results. The average accelerations determined for each curve are listed in the plot legends in Figures 68 through 71. Based on this assessment, the test responses are fairly consistent with average accelerations ranging from 18.4- to 19.2-g.
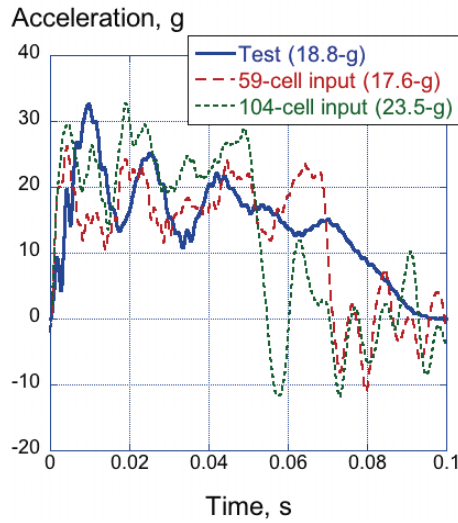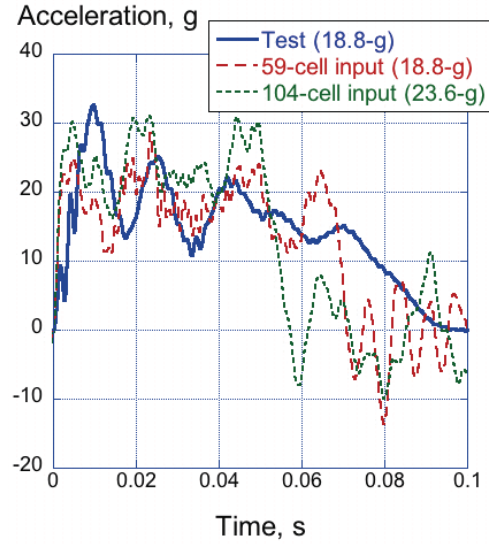
(a) Model executed using Mat 63.   (b) Model executed using Mat 26.

Figure 68. Test-analysis comparisons of the rigid surface impact test (left center accelerometer).

(a) Model executed using Mat 63.   (b) Model executed using Mat 26.

Figure 69. Test-analysis comparisons of the rigid surface impact test (right center accelerometer).

In general, average accelerations obtained from the models in which input stress-strain curves were based on the 59-cell response were consistently lower than the test data by approximately 1-g, with predicted values ranging from 17.4- to 18.8-g. Regardless of material model (Mat 63 or Mat 26), when the input stress-strain response curves are based on the 104-cell test data, the average accelerations are too high, ranging from 23.3- to 23.7-g, and the predicted pulse durations are too short as compared with the test data. Longer pulse durations are seen when the 59-cell stress-strain response curves are input; however, even these responses have a shorter duration than the experimental curves.

(a) Model executed using Mat 63.　　　　(b) Model executed using Mat 26.

Figure 70. Test-analysis comparisons of the rigid surface impact test (front left accelerometer).

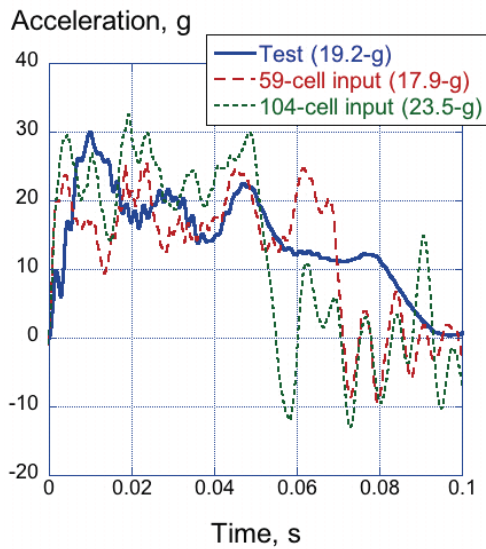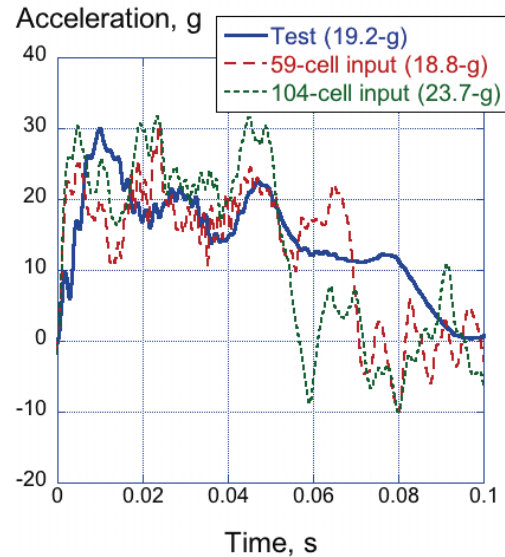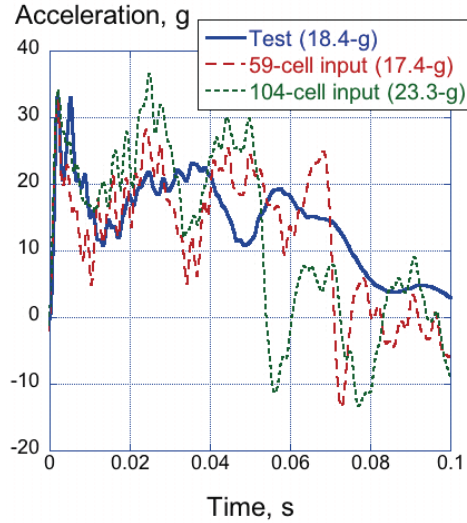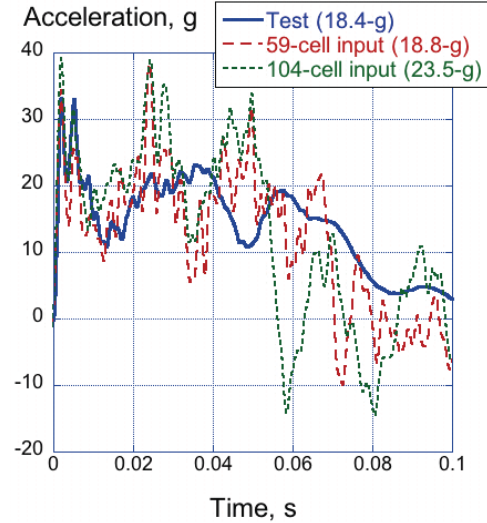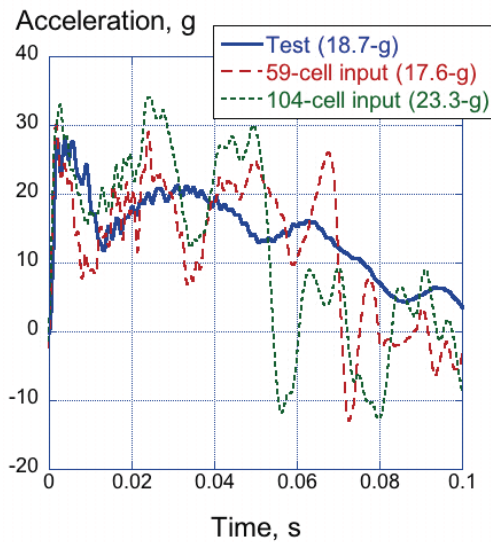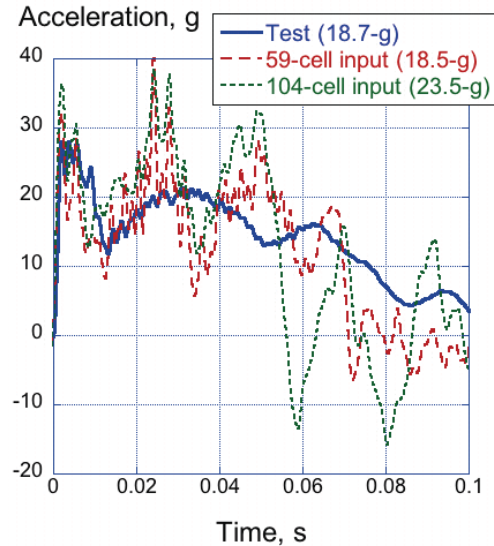(a) Model executed using Mat 63.　　　　(b) Model executed using Mat 26.

Figure 71. Test-analysis comparisons of the rigid surface impact test (right rear accelerometer).

4.2.3.2 Results for Water Impact

The Arbitrary Lagrange-Euler (ALE) method, available in LS-DYNA, was used to simulate the fuselage section impact test into water. The fuselage section with DEA blocks represented the Lagrangian portion of the model, while a cylindrical-shaped mesh represented the Eulerian portion, as shown in Figure 72. Note that the fuselage section model shown in Figure 72 is the same model used for the rigid surface impact. In this case, the rigid surface was removed, and two Euler meshes were added representing the water and the air above the water. A total of 72,900 additional solid elements are included in this model to represent the air and water.

(a) Complete model.   (b) Front view without air.
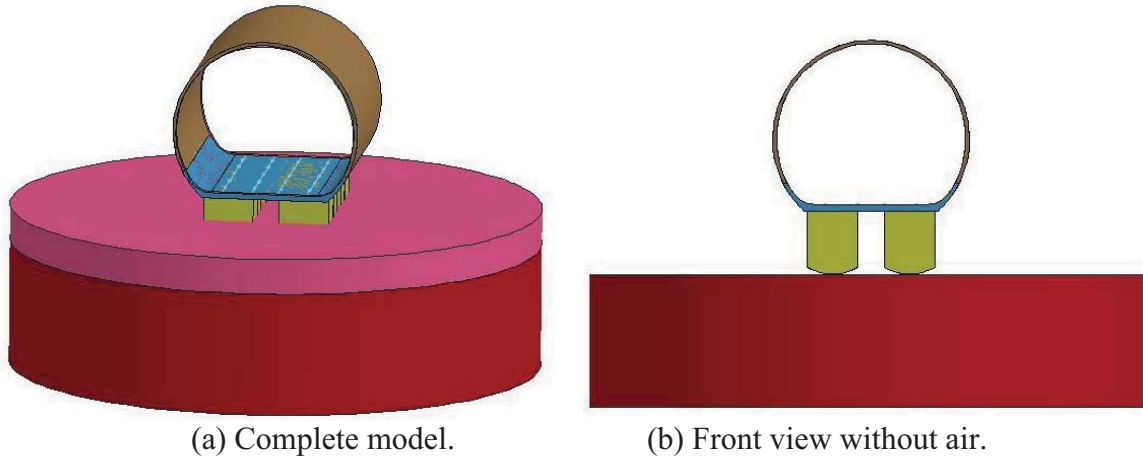
Figure 72. ALE models of fuselage section with DEA impact into water.

Predicted responses are compared with test data for four different floor locations in Figures 73-76 for simulations in which the DEA blocks were assigned Mat 63 and Mat 26 with two different input curves, one based on the 59-cell DEA component crush data and the other based on the 104-cell test data. Comparisons are made with the inboard (IB) accelerometers located on the left and right center lead blocks, and from the left front and right rear blocks. These accelerometer locations are shown in Figure 30(b). As was done for the rigid surface impact, average accelerations were determined for the test and the analytical responses, based on a time interval of 0.02-s. This duration was selected as being representative of the amount of time needed for the DEA blocks to completely break through the surface of the water. The values of average acceleration are shown in the legends of each plot.

(a) Mat 63 model of DEA.   (b) Mat 26 model of the DEA.
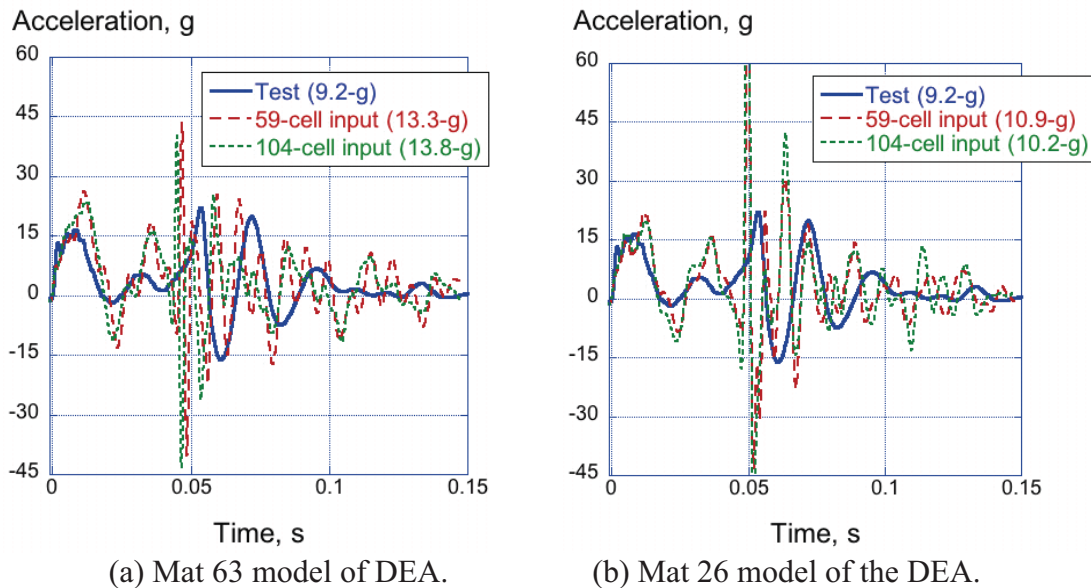
Figure 73. Test-analysis results for water impact at the left center IB location.
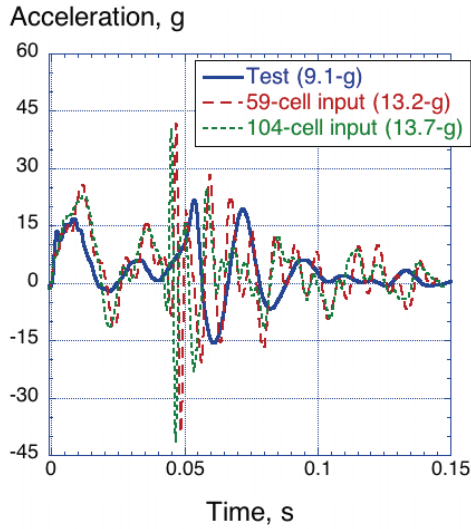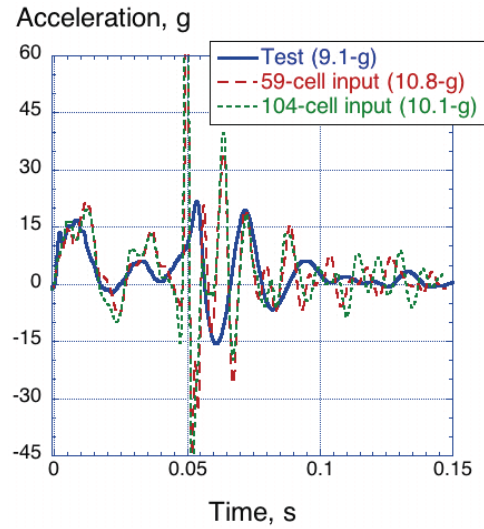
(a) Mat 63 model of DEA.   (b) Mat 26 model of the DEA.

Figure 74. Test-analysis results for water impact at the right center IB location.
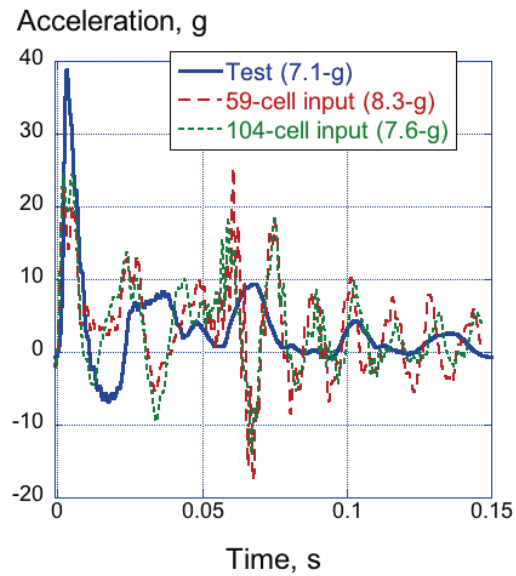
(a) Mat 63 model of DEA.   (b) Mat 26 model of the DEA.

Figure 75. Test-analysis results for water impact at the left front location.

As mentioned previously, the water impact test was different from the rigid surface and sand impact tests in that the floor-level acceleration responses differed based on location. For example, the accelerometers located on the center blocks recorded an initial 15-g pulse of 0.02-s duration. At about 0.05-s, these same accelerometers recorded a second spike in the response, of equal or larger magnitude than the first, which was attributed to impact of the bottom surface of the floor with the water. Conversely, the front left and right rear accelerometers recorded a high magnitude (36-g) pulse of 0.01- to 0.015-s duration. No strong secondary impact was observed. All of the solid-element models performed well in simulating these different test responses. Also of note, prior trends in the rigid surface simulations indicated differences in average acceleration based on which stress-strain input curves were used. These differences are no longer seen in the

68

water impact simulation. As mentioned previously, very little crushing of the DEA was measured during the water impact test and the curved shape of the DEA blocks played an important role in lowering the floor-level accelerations. Based on these factors, the importance of the material response of the DEA is downplayed for this terrain.
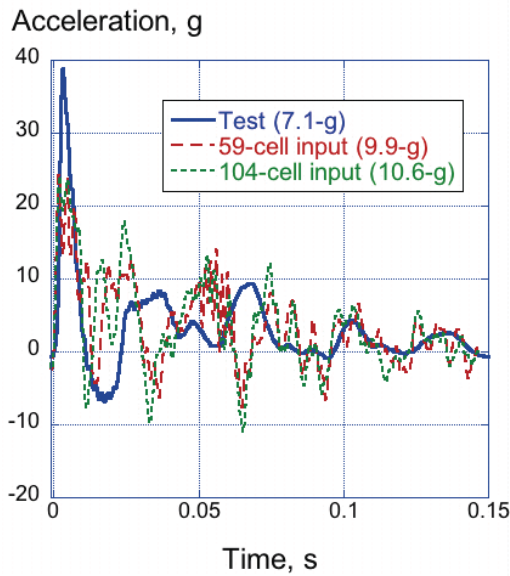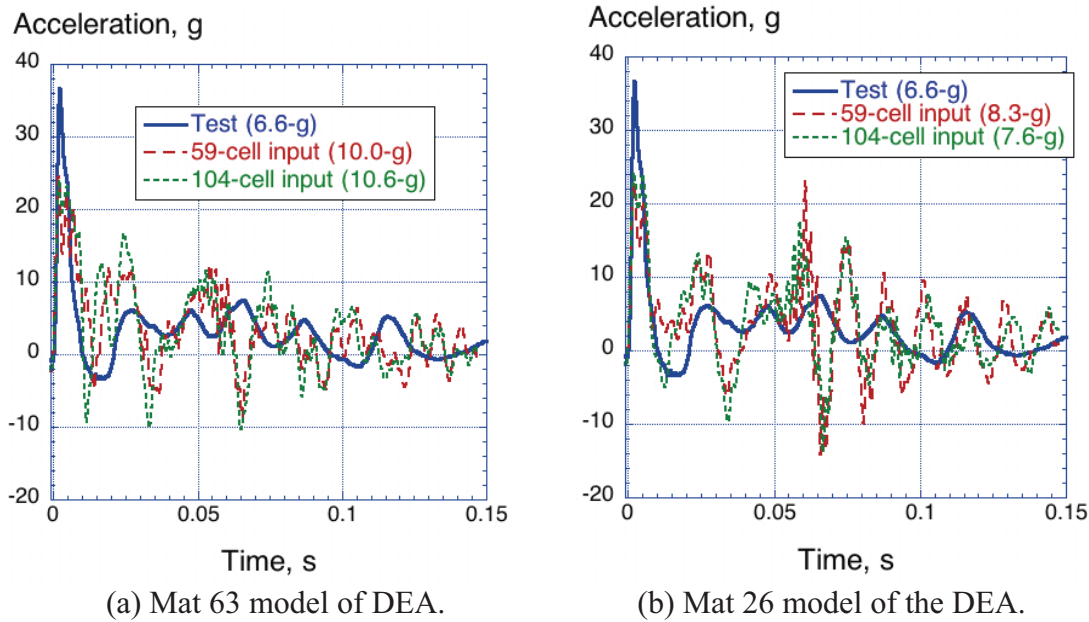

(a) Mat 63 model of DEA. (b) Mat 26 model of the DEA.

Figure 76. Test-analysis results for water impact at the right rear location.

4.2.3.3 Results for the Soft Soil (Sand) Impact

The soft soil (sand) impact test of the fuselage section was simulated using LS-DYNA in which the DEA blocks were represented using solid elements. A picture of the fuselage, DEA, and sand model is shown in Figure 77. The same fuselage section model that was used in the rigid and water surface simulations was used for this simulation. As with the rigid surface and water impact simulations, the DEA blocks were assigned two different material properties, Mat 63 and Mat 26, with two different input curves based on the 59- and 104-cell DEA crush test responses.

The sand was modeled using 84,672 hexagonal solid elements with material properties obtained from a model that was developed in 2001 for correlation with test data obtained in a drop test onto a similar type of sand [27]. Initially, pre-test predictions of the soft soil (sand) impact test were generated in LS-DYNA using a Mat 63 material model to represent the soil, as documented in Reference 38. However, test-analysis correlation results indicated that the Mat 63 model retains too much elastic energy, which is released to produce excessive rebound. Another shortcoming of the Mat 63 model is that the unloading curve cannot be specified independently, and Poisson's ratio is effectively zero. A soft soil may initially load with a relatively small modulus, while unloading may require a very large modulus. The tensile cutoff stress must be nonzero to prevent element failure under small element strains. Consequently, other soil models were investigated and the Mat 5 (*MAT_SOIL_AND_FOAM) model was chosen for additional analysis due to its simplicity and added flexibility [21]. The Mat 5 model has a shear failure surface that is pressure dependent, which is a basic property of geo-materials, and unlike Mat 63 allows for a separate unloading bulk modulus. In addition, the Mat 5 model is more fluid-like

69

under many conditions, which is ideal for a soft soil. In the Mat 5 material model, the yield surface, i.e., the strength of the soil, increases with larger confining pressures. As documented in Reference 38, the specific material input parameters to Mat 5 were partially determined from the post-test penetrometer drops, which were simulated using LS-DYNA as a means of calibrating the material model. The input values for the model are shown in Table 16.
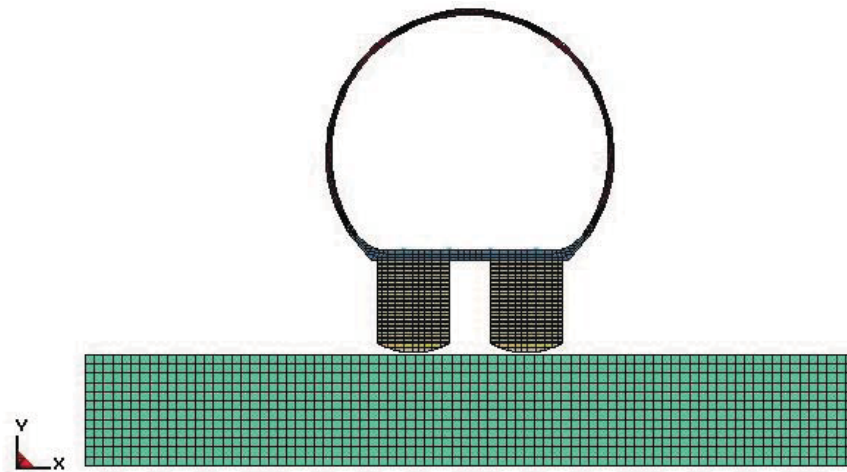
Figure 77. LS-DYNA model of fuselage with DEA above sand.

Table 16. Mat 5 input properties for soft soil

Variable Name	LS-DYNA Symbol	Value	Units
Density	RO	1.36e-04	$lb\text{-}s^2/in^4$
Shear Modulus	G	267	psi
Bulk Unloading Mod	K	10000.	psi
Yield Surface Coeff	A0	0	psi^2
Yield Surface Coeff	A1	0	psi
Yield Surface Coeff	A2	0.3	-
Pressure Cutoff	PC	0	psi
Crushing option	VCR	0 (default)	-
Reference Geometry	REF	0 (default)	-

Comparisons of predicted and experimental acceleration responses are shown in Figures 78-81 for four different floor locations including the left and right center blocks, the left front, and right rear blocks. These accelerometer locations are depicted in Figure 24(b). As before, average accelerations were determined for the experimental and analytical time history responses for a time interval of 0.0- to 0.05-seconds. Based on this simple comparison, uniformity in the test results is seen with average accelerations ranging from 16.9- to 17.7-g. The experimental acceleration pulses exhibit an initial peak ranging from 27- to 40-g, which gradually decreases over time.

Generally, all of the simulations exhibit the same trends as the test data. As with the rigid surface impact, differences in average acceleration are observed based on which input stress-

strain curves are used. For simulations executed using the 59-cell stress-strain input, the average accelerations are always lower than the test by approximately 1-g, regardless of which material model is used. These values range from 16.1- to 17.4-g. For simulations executed using the 104-cell-based input, the average accelerations are always higher than the experiment by approximately 3-g, ranging from 19.9- to 21.3-g. Also, the DEA models with input curves based on the 104-cell dynamic crush test data have a shorter pulse duration than the test data.

(a) Mat 63 material model. (b) Mat 26 material model.
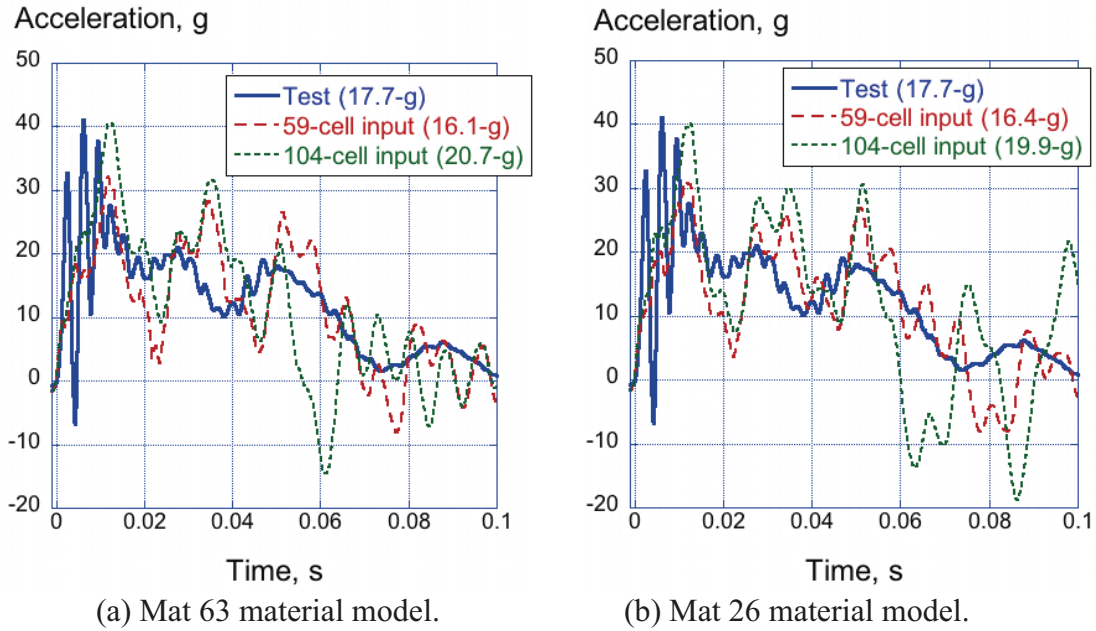
Figure 78. Test-analysis results for sand impact (left center block).

(a) Mat 63 material model. (b) Mat 26 material model.
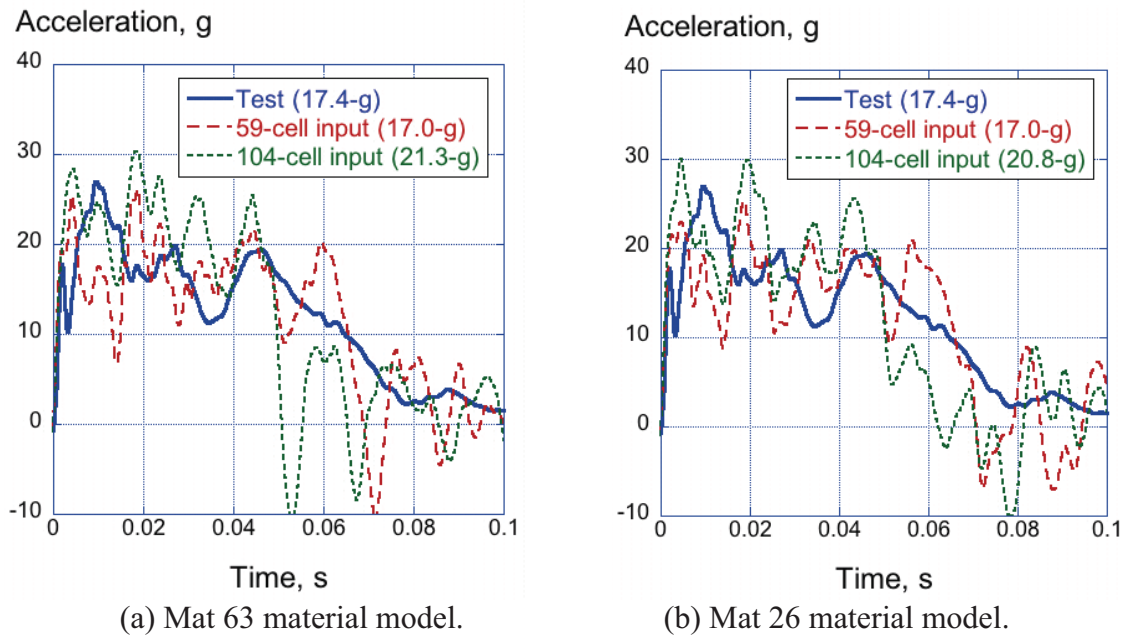
Figure 79. Test-analysis results for sand impact (right center block).
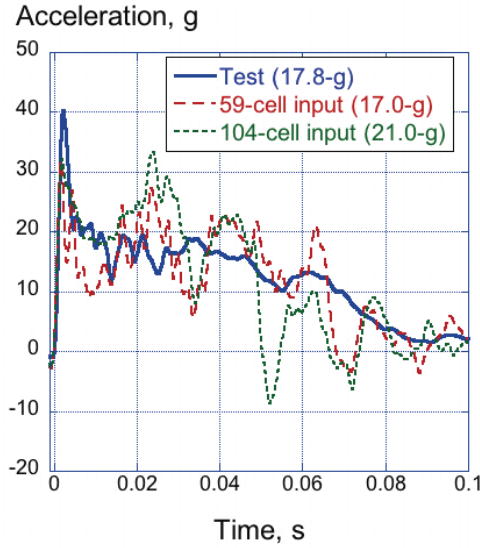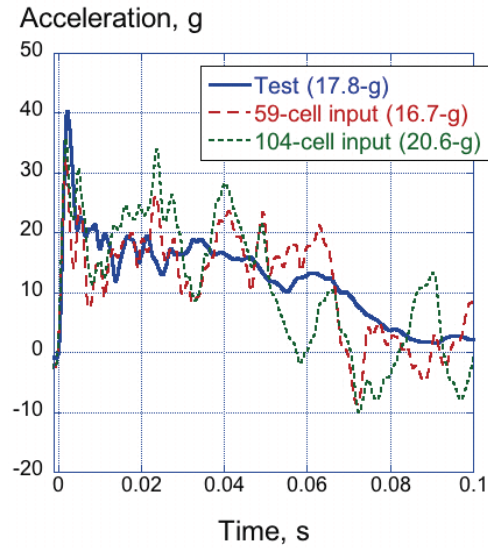
(a) Mat 63 material model.   (b) Mat 26 material model.

Figure 80. Test-analysis results for sand impact (left front block).
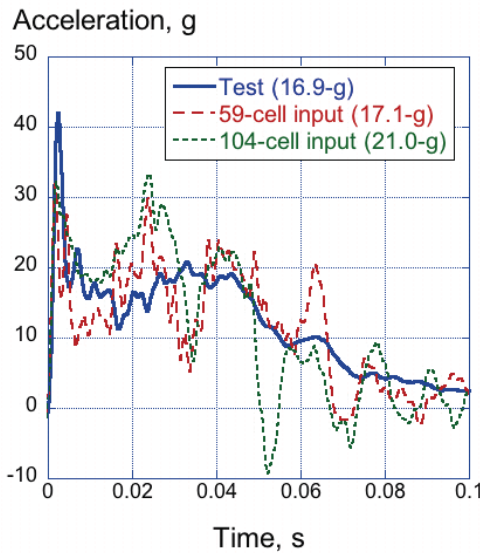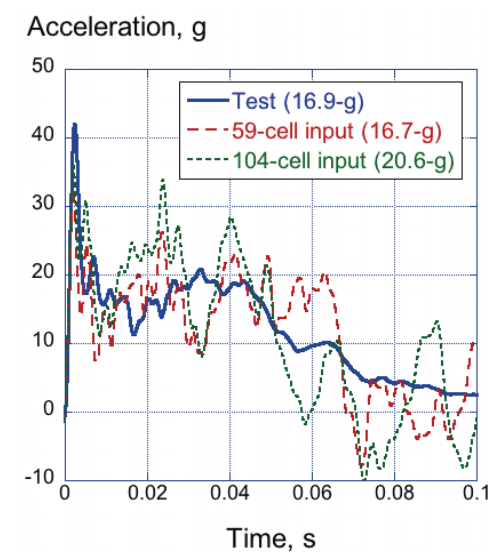
(a) Mat 63 material model.   (b) Mat 26 material model.

Figure 81. Test-analysis results for sand impact (right rear block).

5.0 DISCUSSION OF RESULTS

An externally deployable composite honeycomb structure was evaluated through experimental testing and found to be an effective energy absorber that could be used to mitigate the crash energy of light aircraft and rotorcraft. The energy absorption capabilities of the DEA were demonstrated through dynamic crush tests of multi-cell components. The specific energy absorption properties of the DEA are compared with those of aluminum and paper honeycomb in Table 17. These data show that the current configuration of the DEA is comparable to aluminum honeycomb. Unlike the DEA, however, aluminum honeycomb is not deployable. Also, it should be noted that the DEA used in this study was not optimized, either through experimental

testing or analytical studies. It may be possible through selection of a different material system, or different combinations of cell width, thickness, or cross-sectional shape to tailor the energy absorption properties of the DEA while minimizing its weight.

Table 17. Comparison of specific energy absorption properties

Type of honeycomb	Material specification	Cell width, in.	Cell wall thickness, in.	Honeycomb density, lb/ft^3	Crush stress, psi
DEA	Kevlar$^®$-129 fabric/epoxy oriented at ±45° longitudinally	1.0	0.01	1.15-1.59	16.4-20.7
Hexcell HexWeb$^®$ CR III	Aluminum 5052	0.375	0.0007	1.0	25.0
IPS paper honeycomb	Kraft paper w/o face sheets	0.375	0.007	3.2	41.5

As documented in this paper, the DEA components were subjected primarily to loading in the normal direction, or in the same direction as the longitudinal axes of the cells. However, actual aircraft crashes rarely occur under conditions in which only vertical velocity is present. Consequently, as a final step in the building block approach to demonstrate the energy absorbing capabilities of the DEA, a full-scale crash test of a light helicopter that was retrofitted with the DEA was conducted at the NASA Landing and Impact Research Facility in December 2009. This test was conducted under combined velocity conditions of 40-ft/s forward and 26-ft/s vertical velocities. Crushing of the DEA blocks beneath the helicopter successfully limited the floor-level accelerations to approximately 10-g during this severe crash test. A thorough description of this experiment is beyond the scope of the present paper; however, additional information is available in References 64-70.

Finally, a new approach for quantifying test/analysis correlation needs to be developed and utilized. In the present paper, test-analysis correlations are presented as plots of acceleration time histories, and data obtained from acceleration responses such as initial peak, average acceleration, average crush stress, and peak compaction acceleration. In comparing experimental and analytical acceleration time histories, the level of agreement is determined by comparing the onset rate, magnitude, timing, and averages of the acceleration responses, and the pulse duration. Rarely will the analyst see "good" correlation between test and analysis in the sense of an absolute match for all of these parameters. In general, the level of correlation is deemed "good or reasonable" if these parameters are "in the ball park." Thus, the need to re-evaluate the current crash data analysis and correlation methodologies for use with detailed finite element model simulations has been identified [42]. Recently, a project was initiated at NASA Langley to better quantify the accuracy of crash simulation results. The motivation for the project, as stated in Reference 37, was "to document modeling improvements, to evaluate design configurations analytically, and to enable certification or qualification by analysis."

Several important findings are repeated from Reference 37, as follows. "It is necessary to quantify and understand experimental variations, channel-to-channel, for symmetric locations, as well as test-analysis variations. Future crash finite element model development could be expedited by correlation with experimental modal analysis results, especially since the modal correlation will depend on the accuracy of the global stiffness and mass distribution of the finite element model. Also, this approach provides a second set of data for correlation, which is important given that most test articles are destroyed during crash testing." Continued work is needed to automate rigorous test-analysis correlation methodologies to improve and redefine the level of accuracy.

6.0 CONCLUDING REMARKS

An experimental and analytical study was conducted to assess the energy absorption capabilities of a novel Deployable Energy Absorber (DEA). The DEA is a composite honeycomb structure that can be deployed, much like an external airbag system, to provide energy attenuation during aircraft or rotorcraft crash events. A building block approach was taken during the experimental program that included: material characterization testing of the DEA constituent, Kevlar®-129 fabric/epoxy; three-point bend testing of single hexagonal cells to highlight shear and compressive buckling failures; dynamic crushing of multi-cell DEA components subjected to both normal and off-axis loading to assess energy absorption capabilities; and vertical drop testing of a composite fuselage section, retrofitted with four DEA blocks, onto multi-terrain surfaces. At each stage of the testing, finite element simulations were performed using the explicit nonlinear transient dynamic code, LS-DYNA. Major findings of the research program are listed, as follows.

- Even though many different material systems could have been used in the construction of the DEA, Kevlar®-129 fabric/epoxy proved to be a good choice based on its inherent toughness and ability to mimic plastic-like behavior when loaded in compression. Only limited material characterization testing was performed that provided some data for input into LS-DYNA material models. However, a complete data set was not generated; consequently, many LS-DYNA input values had to be input based on engineering assessment.

- Flexural testing of four different sizes of single hexagonal cells indicated that the shear stability increased linearly as a function of the ratio of cell wall thickness divided by cell wall width. A laminated composite material model (Mat 58) in LS-DYNA was successfully calibrated through test-analysis comparison using a shell-element-based finite element model. A second isotropic material model (Mat 24), which is based on an input user-defined stress-strain response, was also evaluated; however, the level of agreement for this model was poor based on comparison with the flexural test results. However, Mat 24 was evaluated further in simulations of the dynamic crush response of the DEA components due to the compression-dominated nature of those tests.

- Dynamic crush tests of three multi-cell DEA components were performed for both normal and off-axis loading. The specific DEA configuration used in this study (±45° Kevlar®-129 fabric/epoxy, with a ply thickness of 0.01-in. with hexagonal cross-section

cells having an edge length of 1-in.) was designed to provide a 20-psi average crush stress. A measured average crush stress of 19.8-psi was determined by averaging the individual crush stress values obtained from the two normal DEA components (22.0-psi for the 104-cell component and 17.6-psi for the 59-cell component), indicating that the design goal was achieved.

- A comparison of specific energy absorption properties shows that the DEA blocks provide comparable energy absorption to aluminum honeycomb. However, it should also be noted that the current configuration of the DEA was not optimized to minimize weight.

- Both shell- and solid-element models were developed to represent the DEA components. These models were evaluated to determine if they could accurately predict initial loading, sustained crushing, and compaction responses of the DEA components. For the shell-element models, both Mat 58 and Mat 24 material models were able to capture the uniform crushing response and compaction behavior of the DEA components. However, the reader is cautioned against using an isotropic material model (Mat 24) to simulate a highly orthotropic material when subjected to more complex loading scenarios.

- For the solid-element models, both Mat 63 (crushable foam) and Mat 26 (honeycomb) models were evaluated. These models relied on input of stress versus volumetric strain responses obtained from test data. Both material models demonstrated reasonable correlation with test data; however, unlike the shell-element models, the solid-element models were unable to predict the observed deformation modes.

- Vertical drop tests of a composite fuselage section retrofitted with four DEA blocks were conducted to evaluate the performance of the DEA during multi-terrain impact (rigid surface, water, and soft soil). The DEA blocks were designed to limit floor-level accelerations to 20-g. These tests required that a cover be designed and incorporated into the DEA to permit effective load transfer into the honeycomb cells. Load attenuation through crushing occurred in both rigid surface and soft soil impacts. In these cases, the impact surface provided adequate reaction load to initiate and maintain stable crushing. Given that the impact velocity conditions were nearly identical, 38.4- versus 37.4-ft/s, similar acceleration responses were obtained for these two tests. However, for water impact, kinetic energy was dissipated primarily by accelerating the displaced water volume. Though effective in attenuating the initial peak, the energy absorbers were not able to absorb kinetic energy through crushing. This finding is by no means a drawback of the energy absorber but simply a reality associated with water impact. For all multi-terrain impact tests, measured average floor-level accelerations were below the 20-g limit, thus the design crush load of the energy absorber was achieved.

- A finite element model of the fuselage section was modified with shell- and solid-element representations of the DEA blocks and simulations of the multi-terrain impact tests were performed. Generally good correlation was obtained for both models.

Testing performed during the experimental program demonstrated that the DEA concept exhibits excellent energy absorption capabilities. During each stage of the DEA evaluation process, finite element models of the test articles were developed and simulations were performed using the explicit, nonlinear transient dynamic code, LS-DYNA. The generally high level of test-analysis correlation provides confidence in the use of analytical tools for design of energy absorbing structures.

7.0 REFERENCES

1. Porter L., "NASA's New Aeronautics Research Program," Presentation at the 45th AIAA Aerospace Sciences Meeting and Exhibit, Reno, Nevada, November 11, 2007.

2. Jackson K.E., Fuchs Y. T., and Kellas S., "Overview of the NASA Subsonic Rotary Wing Aeronautics Research Program in Rotorcraft Crashworthiness," *Journal of Aerospace Engineering*, Special Issue on Ballistic Impact and Crashworthiness of Aerospace Structures, Volume 22, No. 3, July 2009, pp. 229-239.

3. Kellas S., "Deployable Rigid System for Crash Energy Management," U.S. Patent Nos. 6,755,453 on June 29, 2004; 6,976,729 on December 20, 2005; and 7,040,658 on May 9, 2006.

4. Kellas S. and Jackson K. E., "Deployable System for Crash-Load Attenuation," *Journal of the American Helicopter Society*, Vol. 55, No. 4, October 2010, pp. 042001-1 through 042001-14.

5. Kellas S. and Jackson K. E., "Multi-Terrain Vertical Drop Tests of a Composite Fuselage Section," *Journal of the American Helicopter Society*, Vol. 55, No. 4, October 2010, pp. 042002-1 through 042002-1 through 042002-7.

6. Vassilakos G. J., et al., "Orion Crew Module Landing System Simulation and Verification," 2011 IEEE Aerospace Conference, Big Sky, Montana, March 5-12, 2011.

7. Shane J. S., "Design and Testing of an Energy-Absorbing Crewseat for the F/FB-111 Aircraft," NASA-CR-3916, August 1985.

8. Yosef V., BenMoshe A., Noyman Y., Gansman B., and Bradney C., "Rotorcraft External Airbag Protection System," Proceedings of the AHS 62nd Annual Forum, Phoenix AZ, May 2006.

9. Bolukbasi A. O., "Active Crash Protection Systems for UAVs," Proceedings of the 63rd AHS Annual Forum, Virginia Beach, VA, May 1-3, 2007.

10. Bolukbasi A. O., *et al*, "Rotorcraft Active Crash Protection Systems," Proceedings of the 67th AHS Annual Forum, Virginia Beach, VA, May 3-5, 2011.

11. Waye D. E., Cole J. K., and Rivellini T. P., "Mars Pathfinder Airbag Impact Attenuation System," AIAA-95-1552-CP, 13th AIAA Aerodynamic Decelerator Systems Technology Conference, Clearwater Beach Florida, May 1995.

12. Stein J., and Charles S., "Recent Developments in Inflatable Airbag Impact Attenuation Systems for Mars Exploration," 44th AIAA/ASME/ASCE/AHS SDM Conference, Norfolk Virginia, April 2003.

13. Cooper M., Sinclair R., Sanders J., and Frigerio J., "Design and Testing of an Airbag Landing Attenuator System for a Generic Crew Return Vehicle," Proceedings 18th AIAA Aerodynamic Decelerator Systems Technology Conference and Seminar, AIAA 2005-1616, 2005.

14. Smith R. H., "The Design and Development of Radio-Frequency Transparent Omni-directional Energy-Absorbing Element Systems," NASA CR-66301, NVR-5114, January 1967.

15. Bixby H. W., "Development of a Paperboard Honeycomb Decelerator for Use With Large Platforms in Aerial Delivery Systems," USAF Report WADC-TR-59-776, 1959.

16. Schafer J. P., "Volumetrically Expandable Energy Absorbing Material," US Patent No. 3,339,673, September 1967.

17. Mehaffie S. R., "Foam Impact Attenuation System," AIAA 79-0416, AIAA 6th Aerodynamic Decelerator and Balloon Technology Conference, Houston, Texas, March 1979.

18. Chambers J. R., "Partners in Freedom: Contributions of the Langley Research Center to U.S. Military Aircraft of the 1990's," NASA SP-2000-4519, Monographs in Aerospace History Number 19, 2000.

19. Jackson K. E., Boitnott R. L., Fasanella E. L., Jones L.E., and Lyle K. H., "A Summary of DOD-Sponsored Research Performed at NASA Langley's Impact Dynamics Research Facility (IDRF)," *Journal of the American Helicopter Society*, Vol. 51, No.1, January 2006, pp 59-69.

20. Hallquist J. Q., "LS-DYNA Keyword User's Manual," Volume I, Version 971, Livermore Software Technology Company, Livermore, CA, August 2006.

21. Hallquist J. Q., "LS-DYNA Keyword User's Manual," Volume II Material Models, Version 971, Livermore Software Technology Company, Livermore, CA, August 2006.

22. Farley G. L., "Energy Absorption of Composite Materials," *Journal of Composite Materials*, Vol. 17, No. 3, 1983, pp. 267-279.

23. Kellas S., and Morton J., "Scaling Effects in Angle-Ply Laminates," NASA Contractor Report CR-4423, February 1992.

24. Fleming D.C., and Vizzini A.J., "Off-Axis Energy Absorption Characterization of Composites for Crashworthy Rotorcraft Design," *Journal of the American Helicopter Society*, Vol. 41, July 1996, pp. 239-246.

25. Fleming D.C., and Vizzini A.J., "The Effect of Side Loads on the Energy Absorption of Composite Structures," *Journal of Composite Materials*, Vol. 26, No. 4, 1992, pp. 486-499.

26. Baldwin M., "Final Report – Recommendations for Injury Prevention in Civilian Rotorcraft Accidents," TR-00016, Simula Technologies, Inc., February 29, 2000.

27. Sareen A. K., Sparks C. E., Mullins B. R., Fasanella E. L., and Jackson K. E., "Comparison of Soft Soil and Hard Surface Impact Performance of a Crashworthy Composite Fuselage Concept," Proceedings of the AHS Forum 58, Montreal, Canada, June 11-13, 2002.

28. Fasanella E. L., Jackson, K. E., Sparks C. E., and Sareen A. K., "Water Impact Test and Simulation of a Composite Energy Absorbing Fuselage Section," *Journal of the American Helicopter Society*, Vol. 50, No. 2, April 2005, pp. 150-164.

29. Witlin G., Smith M., and Richards M., "Airframe Water Impact Analysis Using a Combined MSC/DYTRAN-DRI/KRASH Approach," Proceedings of the 53rd Annual Forum of the American Helicopter Society, Virginia Beach, VA, April 29 – May 1, 1997.

30. Tho C. H., Sparks C. E., and Sareen A. K., "Hard Surface and Water Impact Simulations of Two Helicopter Sub-Floor Concepts," Proceedings of the 60th Annual Forum of the American Helicopter Society, Baltimore, MD, June 7-10, 2004.

31. Kohlgruber D., Vigliotti A., Weissberg V., and Bartosch H., "Numerical Simulation of a Composite Helicopter Sub-Floor Structure Subjected to Water Impact," Proceedings of the 60th Annual Forum of the American Helicopter Society, Baltimore, MD, June 7-10, 2004.

32. Pentecote N. and Kindervater C. M., "Airframe Water Impact Analysis Using a Local/Global Methodology," Proceedings of the AHS Forum 58, Montreal, Canada, June 11-13, 2002.

33. Michielsen A. L. P. J., Wiggenraad J. F. M., Ubels L. C, Frijns R. H. W. M., Kohlgueber D., Labeas G., and McCarthy M. A., "Design, Test and Analysis of Tensor Skin Panels for Improved Crashworthiness in Case of Water Impact," AHS/SAFE Crashworthiness Specialists' Meeting on Crash Safety Challenges and Innovative Solutions, Phoenix, AZ, September 14-16, 1998.

34. Jackson K.E., Kellas S., and Fasanella E.L., "Impact Testing and Simulation of a Crashworthy Composite Fuselage," Proceedings of the American Helicopter Society Forum 56, Virginia Beach, VA, May 2-4, 2000.

35. Jackson K.E., "Impact Testing and Simulation of a Crashworthy Composite Fuselage Concept," *International Journal of Crashworthiness,* 2001, Vol. 6, No 1, pp. 107-121.

36. Fasanella E.L., and Jackson K.E., "Impact Testing and Simulation of a Crashworthy Composite Fuselage Section with Energy Absorbing Seats and Dummies," *Journal of the American Helicopter Society*, Vol. 49, No. 2, April 2004, pp. 140-148.

37. Lyle K.H., Bark L.W., and Jackson K.E., "Evaluation of Test/Analysis Correlation Methods for Crash Applications," *Journal of the American Helicopter Society*, Vol. 47, No. 4, October 2002, pp. 219-232.

38. Fasanella E.L., Jackson K.E., Lyle K.H., Sparks C.E., and Sareen A. K., "Multi-Terrain Impact Testing and Simulation of a Composite Energy Absorbing Fuselage Section," *Journal of the American Helicopter Society*, Vol. 52, No. 2, April 2007, pp. 159-168.

39. Society of Automotive Engineers, "Recommended Practice: Instrumentation for Impact Test - Part 1, Electronic Instrumentation," SAE J211/1, March 1995.

40. Horta L. G., Jackson K. E., and Kellas S., "A Computational Approach for Model Update of an LS-DYNA Energy Absorbing Cell," *Journal of the American Helicopter Society*, Vol. 55, No. 3, July 2010, pp. 032011-1 – 032011-8.

41. Jackson K. E., "Predicting the Dynamic Crushing Response of a Composite Honeycomb Energy Absorber using a Solid-Element-Based Finite Element Model," Proceedings of the 11th International LS-DYNA Users Conference, Dearborn, MI, June 6-8, 2010.

42. Jackson K. E., Fasanella E. L., and Lyle K. H., "Crash Qualification by Analysis – Are We There Yet," Proceedings of the American Helicopter Society Forum 62, Phoenix, AZ, May 9-11, 2006.

43. Roach P.P., <u>Verification and Validation in Computational Science and Engineering</u>, Hermosa Publishers, Albuquerque, NM, 1998.

44. Oberkampf W.L., Trucano T.G., and Hirsch C., "Verification, Validation, and Predictive Capability in Computational Engineering and Physics," SAND 2003-3769, February 2003.

45. Thacker B.H., "The Role of Non-determinism in Computational Model Verification and Validation," Proceedings of the 46th AIAA/ASME/ASCE/AHS/ASC Structures, Structural Dynamics, & Materials Conference, April 2005, Austin TX, AIAA 2005-1902.

46. Atamturktur S., Hemez F., and Unal C., "Calibration under Uncertainty for finite element Models of masonry monuments," Los Alamos National Laboratory (LANL) Technical Report, LA-14414, February 2010.

47. Horta L.G., Reaves M.C., Annett M.S., and Jackson, K.E., "Multi-Dimensional Correlation of Impact Dynamic Models," Proceedings of the IMAC-XXIX Conference & Exposition on Structural Dynamics, Jacksonville, Florida, January 31 - February 3, 2011.

48. Oberkampf, W.L. and Barone, M.F.: "Measures of Agreement Between Computation and Experiment: Validation Metrics." Journal of Computational Physics, 217 (2001) 5-56, www.elvevier.com/locate/jcp.

49. Schwer L.E., "Validation Metrics for response Histories: Perspectives and Case Studies." Engineering with Computers," Engineering with Computers (2007), 23:295-309.

50. Anderson M.C., Gan W., and Haselman T.K., "Statistical Analysis of Modeling Uncertainty and Predictive Accuracy for Nonlinear Finite Element Models," Proceedings of the 69th Shock and Vibration Symposium, Minneapolis/St. Paul, MN, 1998.

51. Horta L.G., Lyle K.H., Lessard W.B, "Evaluation of Singular Value Decomposition Approach for Impact Dynamic Data Correlation." NASA TM 2003-212657, Oct. 2003.

52. Jackson K. E., and Fuchs Y. T., "Comparison of ALE and SPH Simulations of Vertical Drop Tests of a Composite Fuselage Section into Water," Proceedings of the 10th International LS-DYNA Users Conference, Dearborn, MI, June 8-10, 2008.

53. Fasanella E. L., Lyle K. H., and Jackson K. E., "Developing Soil Models for Dynamic Impact Simulations," Proceedings of the 65th AHS Forum, Grapevine, TX, May 27-29, 2009.

54. Fasanella E. L., Jackson K. E., and Kellas S., "Soft Soil Impact Testing and Simulation of Aerospace Structures," Proceedings of the 10th LS-DYNA Users Conference, Dearborn, MI, June 8-10, 2008.

55. Polanco M. A., Kellas S., and Jackson K. E., "Evaluation of Material Models within LS-DYNA for a Kevlar[®]/Epoxy Composite Honeycomb," Proceedings of the 65th AHS Forum, Grapevine, TX, May 27-29, 2009.

56. Polanco M. A., "Use of LS-DYNA to Assess Impact Response of a Shell-Based Kevlar[®]/Epoxy Composite Honeycomb," Proceedings of the 11th LS-DYNA Users Conference, Dearborn, MI, June 6-8, 2010.

57. Jackson K.E., Kellas S., Annett M.S., Littell J., and Polanco M.A., "Evaluation of an Externally Deployable Energy Absorber for Crash Applications," Proceedings of the International Crashworthiness Conference, Leesburg, VA, September 22-24, 2010.

58. Fleming D. C., "Modeling Composite Laminate Crushing for Crash Analysis," NAG-1-2260, 2001.

59. Carney K., Melis M., Fasanella E., Lyle K. H., Gabrys J., "Material Modeling of Space Shuttle Leading Edge and External Tank Materials for Use in the Columbia Accident Investigation," 8th International LS-DYNA Users Conference, Dearborn, MI, May 2-4, 2004, pp. 3-35 through 3-44.

60. Fasanella E. L. and Kellas S., "Quasi-Static 3-Point Reinforced Carbon-Carbon Bend Test and Analysis for Shuttle Orbiter Wing Leading Edge Impact Damage Thresholds," NASA Technical Memorandum TM-214505, 2006.

61. Matzenmiller A., Lubliner J., and Taylor R. L., "A Constitutive Model for Anisotropic Damage in Fiber Composites, *Mechanica of Materials,* Vol. 20, 1995, pp. 125-152.

62. Aird F., *Fiberglass & Other Composite Materials: A Guide to Non-Metallic Materials for Race Cars, Street Rods, Body Shops, Boats, and Aircraft*, published by HPBooks, The Penquin Group, New York, NY, 2006.

63. Hirth A., Du Bois P., and Weimar K., "A Material Model for Transversely Anisotropic Crushable Foams in LS-DYNA," Proceedings of the 7th International LS-DYNA Users Conference, Detroit, MI, 2002.

64. Kellas S., Jackson K.E., and Littell J.D., "Full Scale Crash Test of a MD-500 Helicopter with Deployable Energy Absorbers," Proceedings of the 66th AHS Forum, Phoenix, AZ, May 11-13, 2010.

65. Littell J. D., Jackson K. E., and Kellas S., "Crash Test of an MD-500 Helicopter with a Deployable Energy Absorber Concept," Proceedings of the International Crashworthiness Conference, Leesburg, VA, September 22-24, 2010.

66. Annett M. S., and Polanco M. A., "System-Integrated Finite Element Analysis of a Full-Scale Helicopter Crash Test with Deployable Energy Absorbers," Proceedings of the American Helicopter Society 66th Annual Forum, Phoenix, AZ, May 11-13, 2010.

67. Annett M. S., "LS-DYNA Analysis of a Full-Scale Helicopter Crash Test," Proceedings of the 11th International LS-DYNA Users Conference, Dearborn, MI, June 6-8, 2010.

68. Littell J. D., "Large Field Photogrammetry Techniques for Aircraft and Spacecraft Impact Testing," Proceedings of the SEM 2010 Annual Conference, Indianapolis, IN, June 6-8, 2010.

69. Littell J. D., Jackson K. E., and Kellas S., "Crash Test of an MD-500 Helicopter with a Deployable Energy Absorber Concept," Proceedings of the International Crashworthiness Conference, Leesburg, VA, September 22-24, 2010.

70. Littell J.D., "Full Scale Crash Test of an MD-500 Helicopter," Proceedings of the 67th American Helicopter Society Annual Forum, Virginia Beach, VA, May 3-5, 2011.

REPORT DOCUMENTATION PAGE

1. REPORT DATE (DD-MM-YYYY)	2. REPORT TYPE	3. DATES COVERED (From - To)
01-11-2011	Technical Memorandum	

4. TITLE AND SUBTITLE

Experimental and Analytical Evaluation of a Composite Honeycomb Deployable Energy Absorber

5a. CONTRACT NUMBER

5b. GRANT NUMBER

5c. PROGRAM ELEMENT NUMBER

6. AUTHOR(S)

Jackson, Karen E.; Kellas, Sotiris; Horta, Lucas G.; Annett, Martin S.; Polanco, Michael A.; Littell, Justin D.; Fasanella, Edwin L.

5d. PROJECT NUMBER

5e. TASK NUMBER

5f. WORK UNIT NUMBER

877868.02.07.07.05.02.01

7. PERFORMING ORGANIZATION NAME(S) AND ADDRESS(ES)

NASA Langley Research Center
Hampton, VA 23681-2199

8. PERFORMING ORGANIZATION REPORT NUMBER

L-20093

9. SPONSORING/MONITORING AGENCY NAME(S) AND ADDRESS(ES)

National Aeronautics and Space Administration
Washington, DC 20546-0001

10. SPONSOR/MONITOR'S ACRONYM(S)

NASA

11. SPONSOR/MONITOR'S REPORT NUMBER(S)

NASA/TM-2011-217301

12. DISTRIBUTION/AVAILABILITY STATEMENT

Unclassified Unlimited
Subject Category 39
Availability: NASA CASI (443) 757-5802

13. SUPPLEMENTARY NOTES

14. ABSTRACT

In 2006, the NASA Subsonic Rotary Wing Aeronautics Program sponsored the experimental and analytical evaluation of an externally deployable composite honeycomb structure that is designed to attenuate impact energy during helicopter crashes. The concept, which is designated the Deployable Energy Absorber (DEA), utilizes an expandable Kevlar® honeycomb structure to dissipate kinetic energy through crushing. The DEA incorporates a unique flexible hinge design that allows the honeycomb to be packaged and stowed flat until needed for deployment. A variety of deployment options such as linear, radial, and/or hybrid methods can be used. Experimental evaluation of the DEA utilized a building block approach that included material characterization testing of its constituent, Kevlar®-129 fabric/epoxy, and flexural testing of single hexagonal cells. In addition, the energy attenuation capabilities of the DEA were demonstrated through multi-cell component dynamic crush tests, and vertical drop tests of a composite fuselage section, retrofitted with DEA blocks, onto concrete, water, and soft soil. During each stage of the DEA evaluation process, finite element models of the test articles were developed and simulations were performed using the explicit, nonlinear transient dynamic finite element code, LS-DYNA. This report documents the results of the experimental evaluation that was conducted to assess the energy absorption capabilities of the DEA.

15. SUBJECT TERMS

Composites; Crashworthiness; Energy absorption; Honeycomb structures

16. SECURITY CLASSIFICATION OF:			17. LIMITATION OF ABSTRACT	18. NUMBER OF PAGES	19a. NAME OF RESPONSIBLE PERSON
a. REPORT	b. ABSTRACT	c. THIS PAGE			STI Help Desk (email: help@sti.nasa.gov)
U	U	U	UU	94	19b. TELEPHONE NUMBER (Include area code) (443) 757-5802